THE UNIVERSITY OF CHICAGO

COARSE-GRAINED MODELING OF HYBRID BLOCK COPOLYMER SYSTEM

A DISSERTATION SUBMITTED TO

THE FACULTY OF THE INSTITUTE FOR MOLECULAR ENGINEERING

IN CANDIDACY FOR THE DEGREE OF

DOCTOR OF PHILOSOPHY

BY

YONGRUI SU

CHICAGO, ILLINOIS

DECEMBER 2016

To my mother and father

Nothing is new in the face of Divide and Conquer Strategy. Smart people find ways to implement it.

TABLE OF CONTENTS

LIST OF FIGURES

LIST OF TABLES

LIST OF ABBREVIATIONS

BD Brownian Dynamics

CH Cahn-Hilliard

CMA-ES Covariance Matrix Adaptation Evolutionary Strategy

DPD Dissipative Particle Dynamics

DSA Directed Self-Assembly

GL Ginzburg-Landau

LJ Lennard Jones

MC Monte Carlo

MD Molecule Dynamics

NP Nanoparticle

ODT Order-Disorder Transition Temperature

OK Ohta-Kawasaki

PM Particle-to-Mesh

TICG Theoretically Informed Coarse Grained

VMD Visual Molecular Dynamics

ACKNOWLEDGMENTS

First and foremost I want to thank Professor Juan J. de Pablo, whose guidance and patience can be seen in nearly every page of this document. He has been a valued advisor who generously supports me in funding and guides me in research. He gave me as much freedom as possible so that I can discover my real interest and in the mean time he also gives me tremendous valuable advice. Without him, this work is impossible. My experience in his group is one of the most enjoyable memories in my life and impacted my future career significantly.

Besides my advisor, I also want to appreciate the rest of my thesis committee: Professor Paul Nealey and Professor Stuart Rowan for reviewing my dissertation.

I am also grateful to all the current and previous member of the de Pablo group, with who I got lots of inspiration and encouragement. Especially, I would like to thank Professor Jean-Louis, Professor Jian Qin, Dr. Abelardo Ramirez-Hernandez and Dr. Marat Andreev for their valuable advice on my nanocomposites model. I also want to thank Dr. Brandon Peters, Lucas Antony, Grant Garner and Joshua Lequieu for their friendship and advice during my graduate study.

Last but not the least, I also want to thank my mother and father whose spirit support far away empowers me every time I was faced up with difficulties.

ABSTRACT

This thesis is comprised of three major projects of my research. In the first project, I proposed a nanoparticle model and combined it with the Theoretically Informed Coarse Grained (TICG) model [2] for pure polymer systems and the grand canonical slip springs model developed in our group to build a new model for entangled nanocomposites. With Molecule Dynamics(MD) simulation, I studied the mechanic properties of the nanocomposites, for example the influence of nanoparticles size and volume fraction on entanglements, the diffusion of polymers and nanoparticles, and the influence of nanoparticles size and volume fraction on viscosity *et al.*. We found that the addition of small-size nanoparticles reduces the viscosity of the nanocomposites, which is in contrary to what Einstein predicted a century ago. However, when particle increases its size to micrometers the Einstein predictions is recovered. From our simulation, we believe that small-size nanoparticles can more effectively decrease the entanglements of nanocomposites than larger particles. The free volume effect introduced by small-size nanoparticles also helps decrease the viscosity of the whole system. In the second project, I combined the Ohta-Kawasaki (OK) model [3] and the Covariance Matrix Adaptation Evolutionary Strategy(CMA-ES) to optimize the block copolymer blends self-assembly in the hole-shrink process. The aim is to predict the optimal composition and the optimal surface energy to direct the block copolymer blends self-assembly process in the confined hole. After optimization in the OK model, we calibrated the optimal results by the more reliable TICG model and got the same morphology. By comparing different optimization process, we found that the homopolymers which are comprised of the same monomers as either block of the block copolymer can form perfect perforated hole and might have better performance than the pure block copolymer. While homopolymers which are comprised of a third-party monomers have negative effects on forming the perforated hole regardless of the composition and the surface energy. In the third project, We applied the OK model and the CMA-ES algorithm to optimize the combined outcome of particular substrate-copolymer combinations, and we arrived at an efficient method for design of substrates leading to nontrivial desirable outcomes.

CHAPTER 1

INTRODUCTION

1.1 Homopolymer and Block Copolymer

Monomers are structure repeating units of a polymer that are connected to each other by covalent bond. [4] Homopolymer is produced by polymerizing the same type of monomers into a macromolecule. Though homopolymers are made from the same monomers, they might differ by their micro-structures, degree of polymerization or architecture. As monomers are linked together in different degrees of polymerization and different architectures, the physical properties of molecules are different. For example, the boiling point and the melting point increase rapidly with the number of backbone bones. Another example is that the high degree of polymerization usually leads to a high degree of crosslinking, which can form a macroscopic molecule, called a polymer network. The properties of networks make them useful as soft solids (erasers,tires) in rubber industry. In this work, the homopolymers we focus on are linear polymer and have the same degree of polymerizations for simplicity.

Polymers containing different monomers are called heteropolymers. If the number of monomer types is two, we can also call it copolymers. If copolymers are formed by linking two or three blocks of monomers and two neighboring block doesn't contain the same type of monomers, we call them diblock copolymers or triblock copolymers respectively. Figure 1.1a) and Figure 1.1b) gives the schematic plot of the diblock copolymer and the triblock copolymer, respectively. The enthalpy of demixing of the constituent parts of the block copolymers leads to microphase separation, while macrophase separation is prevented by the covalent bond between monomers. This enthalpy is proportional to the Flory-Huggins segmental interaction parameter χ, which is found to be inversely proportional to temperature, and is often modeled as $\chi = \frac{A}{T} + B$ [5], where A and B are parameters determined from experiments. Also, the enthalpic penalty is proportional to the degree of polymerization. Thus χN is often used as a parameter to model block copolymer. The Ohta-Kawasaki(OK) model use the a similar parameter A to represent

the function of χN in the free energy.

Self-Assembly is the process by which disorganized materials spontaneously form certain organized morphologies due to a thermodynamic driving force. As illustrated above, block copolymers can spontaneously self-assemble into ordered morphologies, including spheres, cylinders, lamellar, gyroid microphases. The compositions and the chemical incompatibility together determines which kinds of morphologies it will form [6]. If block copolymers are spin coated and annealed on a carefully prepared substrate, they will follow the chemical pattern on the substrate and self-assemble into ordered morphologies following the underlying substrate. This is called direct self-assembly(DSA).

Directed self-assembly (DSA) technology has received much attention for applications. One of the typical examples is to fabricate bit patterned media and integrated circuits. [7, 8, 9, 10] Traditionally, photolithography, a technique where a beam of light is used to carve a designed pattern onto a photosensitive material, is used in the micro- and nano-electronics fabrication industry. However, the resolution of this technique is limited by the wavelength of the light used. In recent years, as the demand for smaller resolution in these industries, it has become harder to keep up with the trend of electronic device miniaturization with this technique. [11, 12, 13] Block copolymer DSA is easily integrated with current lithographic techniques. It also enables frequency multiplication of the underlying pattern, and can be used to repair defects on the original substrate pattern [6]. Therefore, DSA technology is being considered as one of the most promising options for the next generation of lithography tools. [14, 15]

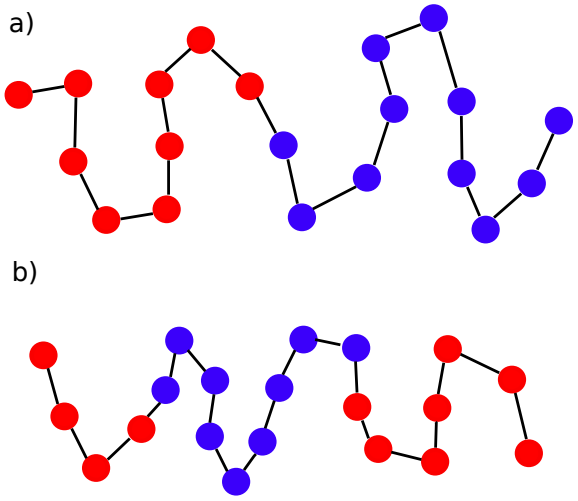

Figure 1.1: a)The schematic plot of the diblock copolymer. b)The schematic plot of the triblock copolymer.

1.2 Entangled Polymer

When the polymer chains are heavily overlapping and melts with long chains behave as elastic networks at short times, those polymer chains form temporary cross-links or are entangled. One feature of entanglement in long chains is the appearance of a wide region in time where the modulus is almost constant in a stress relaxation (or oscillation shear) experiment. [4] Similar to crosslinked rubbers, this region is referred to as the rubbery plateau and the nearly constant value of the modulus in this plateau regime is called the plateau modulus G_e. The average molecular weight of an entanglement strand is called the entanglement molecular weight M_e.

The reason behind the plateau in the stress relaxation is the topological constraints that two chains cannot pass through one another. These topological constraints are called entanglements. Edwards [16] showed that the essence of entanglements can be treated using a tube model which mimics the collective constraints of many chains. By utilizing the Edwards tube concept, de Gennes reduced this many-body problem to the motion of a single chain confined to a tube of surrounding chains. The simplest tube model proposed by de Gennes in 1971 for the motion of linear entangled polymers is called the reptation model. [17] . In reptation model, an entangled chain diffuses along the path which has

the lowest constraints, which is called the primitive path. This curvilinear motion of a polymer along its tube satisfies the topological constraints imposed by surrounding chains.

1.3 Nanoparticle

By convention, particles that have diameter between 1 and 100 nanometers are called nanoparticles. Nanoparticles are of great scientific interest as they often possess unexpected properties. For example, gold nanoparticles melt at much lower temperature($\sim$300 °C for 2.5 nm size) than the gold slabs(1064 °C). [18] Absorption of solar radiation is much higher in materials composed of nanoparticles than it is in thin films without nanoparticles. Therefore, it has the potential to control solar absorption by tuning the size, shape and materials of nanoparticles in solar thermal industries. [19, 20, 21] Because of those unique properties, nanoparticles are being used for diverse purposes, from medical treatments, industry production such as solar and oxide fuel batteries for energy storage, to wide incorporation into diverse materials of everyday use such as cosmetics or cloth, optical devices, catalytic, bactericidal, electronic, sensor technology, biological labeling and treatment of some cancers. [22]

CHAPTER 2

PARTICLE DYNAMICS IN ENTANGLED POLYMER NANOCOMPOSITES: A COARSE-GRAINED DESCRIPTION

2.1 Abstract

The addition of nanoparticles to polymeric liquids has been shown to influence the mechanical properties of the system unexpectedly. For example, it is observed that nanoscale particles lead to a non-Einstein-like decrease in viscosity. The mechanism behinds such an unexpected decrease in viscosity with the addition of nanoscale particles is not entirely explored. A new particle-based Theoretically Informed Coarse-Grained(TICG) model for entangled nanocomposites is proposed to predict and analyze such decrease in viscosity. In our study, the unusual change of viscosity partly roots in the increase of the contribution from the stress relaxation function related to the nanoparticles' core, which relaxes faster compared with the bond-related stress relaxation in the entangled polymers when the size of nanoparticles is small. Another reason for the decrease of viscosity is that the number of entanglements per chain decreases with the introduction of nanoparticles in our model. However, when the size of nanoparticles becomes bigger, the core-related stress correlation would have longer relaxation time, and it can decay even more slowly than the bond-related stress correlation function in loaded nanocomposites. Together with less decrease of entanglements density in composites with large particles, the non-Einstein-like decrease in viscosity could be reversed. Besides the study of the unusual rheology, the diffusion process of the nanocomposites and entanglements are also examined.

2.2 Introduction

The mixing of nanoparticles with polymers to enhance the mechanical properties of the system has been practiced for decades. For example, blending carbon black, zinc oxide and/or magnesium sulfate particles with the vulcanized rubber can be used to prepare

nanoparticle-toughened automobile tires. [23] Reports by researchers also revealed that five-fold increase in the yield and tensile strength of nylon can be achieved by adding mica to it. [24, 25] With the growing availability of nanoparticles, there is surging interest in understanding the mechanisms in which nanoparticles influence the mechanic properties of the materials. One of the mechanic property in the discussion of this work is viscosity.

Micro-sized spherical particles increase the shear viscosity of a pure polymer melt from η_p to a value η following the Einstein law: $\frac{\eta}{\eta_p} = 1 + 2.5\phi_{NP} + 6.25\phi_{NP}^2 + O(\phi_{NP}^3)$, where ϕ_{NP} is the nanoparticles volume fraction. [26, 27, 28]. However, nanosized particles show much richer behaviors [29, 30, 31, 32, 33, 34, 35, 36, 37, 38]. The viscosity of the nanocomposites can be either reduced or increased by tuning the properties and volume fraction of nanoparticles. There are substantial experiments and simulations work of entangled nanocomposites [39, 40, 41, 42, 43, 44]. Kalathi *et al.* [39] found in Molecule Dynamics(MD) simulation with Lennard-Jones(LJ) potential that small energetically neutral nanoparticles can significantly reduce the shear viscosity of a polymer melt because the entanglement weight decrease significantly when particle size decreases and the entanglements weight recovers to its bulk value for large particles. Schneider *et al.* found in experiment that the number of topological chain-chain entanglements decreases with increased nanoparticles loading. Mackay *et al.* [32] and Tuteja *et al.* [29, 30, 31] found in experiments that the addition of small-size neutral nanoparticles reduces the viscosity while the entanglements in the polymer melts is unchanged. And after micro-size particles are added into the system, the composites instead show increase of viscosity.

The present work uses a particle based TICG nanocomposites model with slip springs to address the influence of nanoparticles on entangled homopolymers. Similar to the nanoparticle model introduced in Biondo *et al.* [45], the nanoparticle in our model has excluded volume and also possible grafted brush. However, instead of having the position of the nanoparticles fixed onto the lattice, we let the nanoparticle diffuse according to the equation of motion in our simulation. And we also treat the interactions among nanoparticles and between nanoparticles and polymer beads directly instead of assigning the density of nanoparticles to the space lattice. With this model, we studied the entan-

glements distribution around a single nanoparticle and the impact of loaded nanoparticles on the entanglements of the composites system. We also addressed the diffusion of a single spherical nanoparticle and loaded nanoparticles dissolved in an unentangled and entangled polymer melt. The diffusivity of nanoparticles in entangled polymer melts is strongly dependent on their size and affinity to polymer beads. For nanoparticles smaller than the size of the entanglement mesh, the diffusion of nanoparticles can be described by linear diffusion process. However, for nanoparticles with size comparable to or larger than the entanglement mesh size, non-linear mean-square displacement with power law t^x, $x<1$, is observed in the intermediate diffusion region of nanoparticles. The same behavior is supported by the simulation work of other models [46, 47, 48, 49]. We also found that weakly attractive nanoparticles show faster diffusivity than that of completely neutral nanoparticles, which helps nanoparticles escape the 'caging' regions set by entanglement mesh. Then we explored the molecular origin of the Non-Einstein-like reduced viscosity, reported in Mackay *et al.* [29, 30, 32], in the entangled nanocomposites through direct calculation of the stress correlation function G(t). We found that small nanoparticles reduce the viscosity of a polymer melt due to a reduction in the number of entanglements per chain and the introduction of free volume effects. The number of entanglements per chain is always reduced by the introduction of nanoparticles, regardless of the nanoparticles' size. Such a decrease of entanglements density is also observed in the theoretical work by Kalathi *et al.*. [50] However, based on the calculation of the core stress correlation function separately we predict that the free volume effect of the small-size particles can decrease the viscosity of entangled nanocomposites, and the free volume effect will reverse in the large nanoparticles and the core stress correlation function have much slower decaying power rate as the particles become large.

2.3 Model

2.3.1 Polymers

We use the theoretically informed coarse-grained(TICG) model to describe polymer melts with a volume V at temperature T. The chain is discretized into N beads, with the position of the sth bead in the ith chain denoted by $\mathbf{r}_i$(s). This TICG approach takes into account the following properties: the chain connectivity, chemical distinction between unlike monomers, and finite compressibility of the melt. The chain connectivity is given by the bond potential $\mathcal{H}_{bond}[\{\mathbf{r}_i(s)\}]$ in the form of a harmonic spring model

$$\frac{\mathcal{H}_{bond}[\mathbf{r}_i(s)]}{k_BT} = \frac{3}{2}\sum_{s=1}^{N-1}\frac{[\mathbf{r}(s+1)-\mathbf{r}(s)]^2}{b^2} \tag{2.1}$$

where k_B is the Boltzmann constant, b= $\sqrt{R_e^2/(N-1)}$ is the mean-squared bond length, and R_e is the mean-squared end-to-end distance for an isolated chain.

The chemical distinction between unlike monomers and the finite compressibility of the melts are both incorporated into the non-bonded potential $\mathcal{H}_{nb}$. This work uses the continuous non-bonded potential which assigns a density cloud $\omega(\mathbf{r})$ to each polymer bead [51]. The non-bonded energy is defined as

$$\mathcal{H}_{nb} = \sum_{j>i} U_{ij,nb} \tag{2.2}$$

$$\frac{U_{ij,nb}}{k_BT} = \frac{\sqrt{\bar{N}}}{R_e^3}[\chi N(1-\delta_{K_iK_j})+\kappa N]I(\mathbf{r}_{ij}) \tag{2.3}$$

$$I(\mathbf{r}_{ij}) = \int_V \omega(\mathbf{r}-\mathbf{r}_i)\omega(\mathbf{r}-\mathbf{r}_j)\mathrm{d}\mathbf{r} \tag{2.4}$$

where δ is the Kronecker delta and K_i is A or B, the type of bead i. In homopolymers, i and j beads are chemically identical, which makes $\delta_{K_iK_j}$ equal 1. The spherical density cloud function [51] is used in this work for simplicity.

$$\omega(\mathbf{r}) = \begin{cases} C & 0 \leq |\mathbf{r}| \leq R_{cloud} \\ 0 & R_{cloud} < |\mathbf{r}| \end{cases} \tag{2.5}$$

where C must satisfy the Equation (2.6).

$$N\sqrt{\bar{N}} \int \frac{\mathrm{d}\mathbf{r}}{R_e^3} \omega(\mathbf{r}) = 1. \tag{2.6}$$

The overall potential of the polymer melts is given by

$$\mathcal{H}[\{\mathbf{r}_i(s)\}] = \mathcal{H}_{bond}[\{\mathbf{r}_i(s)\}] + \mathcal{H}_{nb}[\{\mathbf{r}_i(s)\}] \tag{2.7}$$

In this work, since what we consider is homopolymers, the Flory-Huggins parameter χ is set to be 0.

2.3.2 Nanoparticles

The nanoparticle model in this work mimics hard nanoparticles grafted by a dense polymer brush. The core which has an excluded volume and the grafted polymer brush which interacts with surrounding polymers are represented by two potentials: the core potential and the shell potential. The core potential between nanoparticle and polymer is represented by a repulsive potential in the form of Equation (2.8). Likewise, Equation (2.9) accounts for the core potentials among nanoparticles themselves.

$$\frac{\mathcal{H}_{n2p}^{Core}(\mathbf{r})}{k_B T} = \begin{cases} A\{(\frac{|\mathbf{r}|^2}{R_C} - 3|\mathbf{r}|) + 2R_C + \frac{d_s}{3}\} & 0 \leq |\mathbf{r}| \leq R_C \\ A(1 - \frac{|\mathbf{r}| - R_C}{d_s})^3 \frac{d_s}{3} & R_C < |\mathbf{r}| \leq R_C + d_s \\ 0 & R_C + d_s < |\mathbf{r}| \end{cases} \tag{2.8}$$

$$\frac{\mathcal{H}_{n2n}^{Core}(\mathbf{r})}{k_BT} = \begin{cases} A\{(\frac{|\mathbf{r}|^2}{R_C+R} - 3|\mathbf{r}|) + 2*(R_C+R) + \frac{d_s}{3}\} & 0 \le |\mathbf{r}| \le R_C + R \\ A(1 - \frac{|\mathbf{r}|-R_C-R}{d_s})^3 \frac{d_s}{3} & R_C + R < |\mathbf{r}| \le R_C + R + d_s \\ 0 & R_C + R + d_s < |\mathbf{r}| \end{cases} \quad (2.9)$$

A is the coefficient controlling the strength of the core and d_s is the buffer region which ensures the continuity of the derivative of force, the force and energy. R is the distance from the center of the core to the surface of the grafted brush. For simplicity, we assume R = R_C+ 0.07R_e and d_s = 0.05R_e if $R_C \geq$ 0.18 R_e. When R_C < 0.18 we set R = R_C+0.04 R_e and d_s = 0.02R_e . Since in experiments, the grafted chains in also counted in the calculation of nanoparticles volume fraction, we use R to calculate the volume of a nanoparticle, where $V_{NP} = \frac{4}{3}\pi\ R^3$. In our study, A equals 320, which is strong enough to prevent the polymer beads from entering the core of the nanoparticle. In Figure 2.1, we compare our core potential in Equation (2.8) with the repulsive shift-force and shift-energy Lennard-Jones(LJ) potential in the following form:

$$\frac{\mathcal{H}_{n2p}^{LJ}(\mathbf{r})}{k_BT} = \begin{cases} \epsilon_{NP}\{(\frac{R_C^6}{\mathbf{r}^6} - 1 - \frac{6(R_c-\mathbf{r})}{R_C}\} & 0 \le |\mathbf{r}| \le R_C \\ 0 & R_C < |\mathbf{r}| \end{cases} \quad (2.10)$$

where ϵ_{NP} is the tuning parameter to adjust the strength of the LJ potential. Though the form of $\mathcal{H}_{n2p}^{Core}(\mathbf{r})$ is soft when compared with the LJ potential in equation (2.8) and (2.9), it has its unique advantages. In Figure 2.1a), we compare the value of the $\mathcal{H}_{n2p}^{Core}(\mathbf{r})$ with the value of $\mathcal{H}_{n2p}^{LJ}(\mathbf{r})$ in the region close to the center of the core. $\mathcal{H}_{n2p}^{Core}(\mathbf{r})$ has higher energy than $\mathcal{H}_{n2p}^{LJ}(\mathbf{r})$ in the region close to the surface of nanoparticles. Therefore, $\mathcal{H}_{n2p}^{Core}(\mathbf{r})$ is more effective in repelling the polymer beads out of the nanoparticles while maintaining low energy inside the nanoparticles core (r < 0.1 R_e). Figure 2.1a) gives the radial distribution function of the nanoparticles to polymer beads g_{n2p}. In Figure 2.1b), the LJ potential can keeping the polymer beads out of the core only if ϵ_{NP} is very large. However, when ϵ_{NP} is larger than 2, the polymer beads occasionally would enter the

region where the LJ force is large, and the slope of the LJ energy is steep, which would make the simulation unstable. The large force of the $\mathcal{H}_{n2p}^{LJ}(\mathbf{r})$ kicks the polymer beads thousands of R_e away, which increases the workload of periodic boundary conditions handling in the simulation tremendously. Our test shows that when ϵ_{NP} is larger than 2.0, the simulation becomes extremely slow. Therefore, we do not give the result of g_{n2p} when ϵ_{NP} is greater than 2.0.

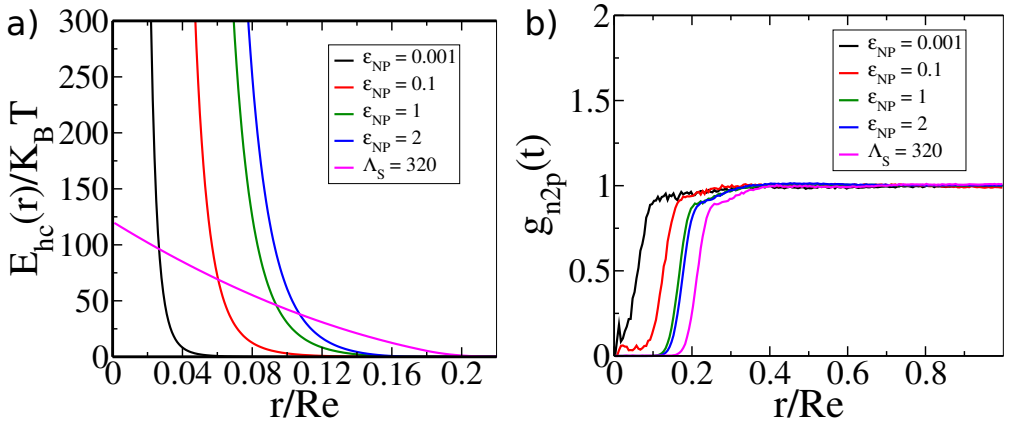

Figure 2.1: $R_C = 0.18R_e$. a) The black, red, green and blue curves come from the LJ potential in the Equation (2.10) and the magenta curve comes from the Equation (2.8). b) Radial distribution function(g_{n2p}) which measures the density of polymer beads surround one single nanoparticle. The core potentials originate from the same equations as in a).

Besides the core potential, a continuous potential describing the shell chemical interaction with polymer beads is added to the surface of the core in the form of the following:

$$\frac{\mathcal{H}_{n2p}^{Shell}(\mathbf{r})}{k_BT} = \begin{cases} 0.0 & 0 \le |\mathbf{r}| < 2R_C - R \\ \Lambda_S(-2(\frac{|\mathbf{r}|-R_C}{R-R_C})^3 - 3(\frac{|\mathbf{r}|-R_C}{R-R_C})^2 + 1) & 2R_C - R < |\mathbf{r}| \le R_C \\ \Lambda_S(2(\frac{|\mathbf{r}|-R_C}{R-R_C})^3 - 3(\frac{|\mathbf{r}|-R_C}{R-R_C})^2 + 1) & R_C < |\mathbf{r}| \le R \\ 0.0 & R < |\mathbf{r}| \end{cases} \tag{2.11}$$

where Λ_S is the parameter controlling the affinity of polymer beads to the nanoparticles, and can be positive or negative. Positive Λ_S means that polymer beads are repulsive to the nanoparticles, and negative Λ_S means that polymer beads and nanoparticles are

attractive to each other.

The overall core potential in the system is given by:

$$\mathcal{H}_{hc} = \sum_{i=1}^{nN} \sum_{j=1}^{n_{NP}} \mathcal{H}_{n2p}(\mathbf{r}_i^{bead} - \mathbf{r}_j^{NP}) + \sum_{i=1}^{n_{NP-1}} \sum_{j=i+1}^{n_{NP}} \mathcal{H}_{n2n}(\mathbf{r}_i^{NP} - \mathbf{r}_j^{NP}) \tag{2.12}$$

$$\mathcal{H}_{n2p}(\mathbf{r}) = \mathcal{H}_{n2p}^{Core}(\mathbf{r}) + \mathcal{H}_{n2p}^{Shell}(\mathbf{r}) \tag{2.13}$$

$$\mathcal{H}_{n2n}(\mathbf{r}) = \mathcal{H}_{n2n}^{Core}(\mathbf{r}) \tag{2.14}$$

where $\mathbf{r}_j^{bead}$ is the position of the jth polymer bead and $\mathbf{r}_j^{NP}$ is the position of the jth nanoparticle. The force or energy associated with equations (2.8),(2.9) and (2.11) is denoted by 'hc'. Figure 2.2 gives a schematic of the nanoparticle in our model and the potential $\mathcal{H}_{n2p}(\mathbf{r})$ in the case of the attractive nanoparticle with $R_C = 0.18\ R_e$.

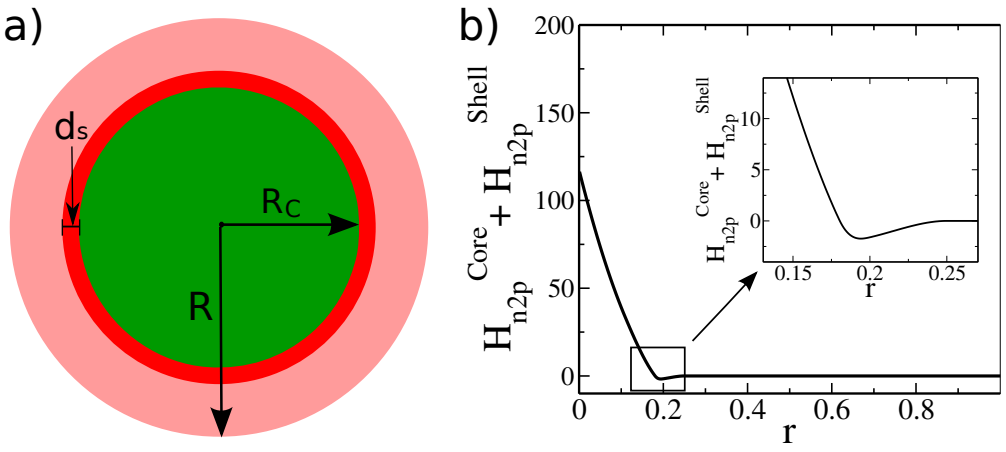

Figure 2.2: a)The schematic of the nanoparticle model defined in Equation 2.8 and Equation 2.11. b) The core potential and shell potential with parameters: $R_C = 0.18\ R_e$, R = 0.25 R_e, Λ_S = -2.0, A = 320 and $d_s = 0.02\ R_e$.

Figure 2.3 gives an illustration of the nanoparticles in entangled nanocomposites. And we also plot the radial distribution function between nanoparticles to nanoparticles in the neutral nanocomposites and attractive nanoparticles, with $\Lambda_S = 0.0$ and Λ_S = -2.0, respectively.

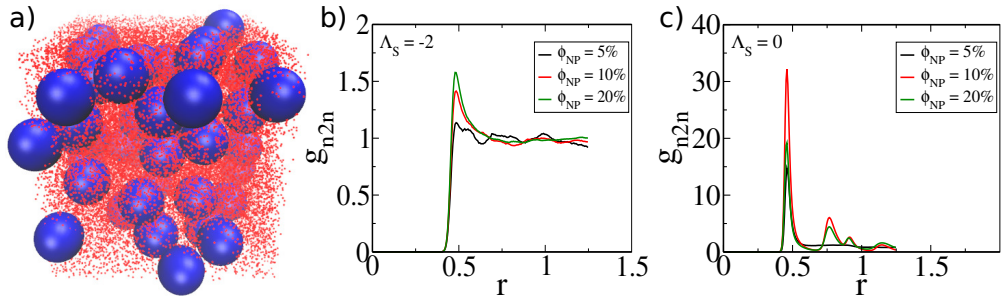

Figure 2.3: a)Illustration of the nanoparticles in nanocomposites in Visual Molecular Dynamics software. [1] b) and c) represent the radial distribution function of nanoparticles to nanoparticles $g_{n2n}(r)$ in the attractive and neutral nanoparticles composites, respectively, with $R_C = 0.18\ R_e$.

2.4 Molecule Dynamics

2.4.1 Brownian Dynamics

After established the TICG model for nanocomposites, the next thing is to define the equations governing the temporal evolution of the system. We have considered both the Dissipative Particle Dynamics(DPD) and Brownian Dynamics(BD) as the potential integration method. The DPD method has the advantage of conserving momentum, which is important when the hydrodynamics plays an important role. Several reports have highlighted the importance of DPD thermostats in non-equilibrium flows. [52, 53] However, our calculation shows that the DPD method is unable to capture some short time dynamical properties, especially the stress relaxation function, when the harmonic bond potential is dominant, which is exactly the case of our model. Details about this can be found in the supplementary materials section of this chapter. For this reason, we choose BD as the integration method in our work since our system does not involve with non-equilibrium flows. The evolution of each polymer bead is governed by the following stochastic differential equations:

$$\nu_{bead}\frac{d\mathbf{r}_j(t)}{dt} = \mathbf{f}_j(t)_{bond} + \mathbf{f}_j(t)_{nb} + \mathbf{f}_j(t)_{hc} + \boldsymbol{\zeta}_j(t) \tag{2.15}$$

where $\mathbf{f}_j(t)_{bond}$ and $\mathbf{f}_j(t)_{nb}$ are the intra- and intermolecular forces, which comes from the bond potential and non-bonded potential respectively, acting on particle j. The $\mathbf{f}_j(t)_{hc}$ is the force associated with nanoparticles acting on the j^{th} bead. The friction coefficient of the polymer beads is denoted by ν_{bead}, and $\boldsymbol{\zeta}_j(t)$ expresses a random force which satisfies the fluctuation dissipation relation: $\langle \zeta_{i\alpha}(t_1)\zeta_{j\gamma}(t_2)\rangle = 2\nu_{bead}k_BT\delta_{ij}\delta_{\alpha\gamma}\delta(t_1-t_2)$, where $\alpha,\gamma \in$ x,y,z. The random force is drawn from the Gaussian distribution with the mean of zero and variance: $2\nu_{bead}k_BT$.

The evolution of the j^{th} nanoparticle is governed by a slightly different stochastic differential equation:

$$\nu_{NP}\frac{d\mathbf{r}_j(t)}{dt} = \mathbf{f}_j(t)_{hc} + \boldsymbol{\zeta}_j(t) \tag{2.16}$$

The only force governing the motion of nanoparticles is the core interaction in Equations (2.8), (2.9) and (2.11). The fluctuation dissipation relation $\langle \zeta_{i\alpha}(t_1)\zeta_{j\gamma}(t_2)\rangle = 2\nu_{NP}k_BT\delta_{ij}\delta_{\alpha\gamma}\delta(t_1-t_2)$, should still be satisfied. The variance of the Gaussian force is $2\nu_{NP}k_BT$, in which ν_{NP} follows the Stokes-Einstein relation $\mathrm{D} = \frac{k_BT}{f\pi\eta R}$, where η is the viscosity, $f = 4$ or 6 for slip or stick boundary conditions and R is the radius of the nanoparticle. With Einstein relation $\mathrm{D} = \frac{k_BT}{\nu_{NP}}$, we can get the linear relation between ν_{NP} and R: $\nu_{NP} \sim \mathrm{R}$. Therefore, we can estimate the friction coefficient of nanoparticles through the relation $\nu_{NP} = \nu^0_{NP}(\eta)\mathrm{R}/\mathrm{R}^0$ in the short time interval dt. The $\nu^0_{NP} = 50\nu_{bead}$ and $\mathrm{R}^0 = \mathrm{R}_e$ is set in the simulations of this work. The rationale behind our choice of ν^0_{NP} is that the nanoparticles should diffuse slower than the polymer beads but faster enough so that we can observe apparent 'caging' effect in Figure 2.7. Too large ν^0_{NP} will make the nanoparticles diffuse extremely slow, and it will take too much time for the nanoparticles to diffuse out of the intermediate region, which is characterized by the mesh size formed by entanglements.

The stochastic differential Equations (2.15 and 2.16) are solved with the Euler integration algorithm. $\tau_0 = \mathrm{l}_0^2/\mathrm{D}_0$, where $\mathrm{D}_0 = \mathrm{k}_B\mathrm{T}/\nu_{bead}$, rescales the time in the simulation. The physical meaning of τ_0 is the time that a bead takes to diffuse the reference length scale l_0, where l_0 is chosen as $\mathrm{l}_0 = \mathrm{R}_e$ in this work. $\mathrm{D}_0 = \mathrm{k}_B\mathrm{T}/\nu_{bead}$ is the diffusion constant and the rescaled time is given by $\mathrm{t}^* = \mathrm{t}/\tau_0$. $\Delta\mathrm{t}^* = 2\times10^{-4}$ is used in this work

to integrate the equations of motion. The following results are all presented in rescaled units.

2.4.2 Mean-Square Displacement

Mean-square displacement is one of the most common ways to characterize the equilibrium dynamical behavior. The bead's mean-square displacement, $g_1(t)$, is define by

$$g_1(t) = \langle [\mathbf{r}(t) - \mathbf{r}(0)]^2 \rangle \tag{2.17}$$

where the angle brackets indicate ensemble average. The polymer chains also have the mean-square center-of-mass displacements, $g_3(t) = \langle [(r)_{cm}(t) - \mathbf{r}_{cm}(0)]^2 \rangle$, to describe diffusion of the polymer chains. Similar to the Equation (2.17), we use $g_2(t) = \langle [\mathbf{r}(t) - \mathbf{r}(0)]^2 \rangle$ to characterize the dynamics of nanoparticles, where $\mathbf{r}$ denotes the position of nanoparticles instead of polymer beads.

2.5 The Grand Canonical Slip-Springs Model for Entanglements

The pure TICG model as described above relies on soft interactions between polymer beads. These polymer beads can cross each other, which doesn't exhibit any phenomenon of entanglements (the plateau in the stress relaxation for example). The major breakthrough in the theory of entangled polymers is the Edwards' tube model of entangled polymer networks. In tube model, the transverse motion of a polymer is restricted by the surrounding chains. Each polymer reptates effectively in a tube-like region. However, our description of the entanglements is not based on tubes. We use the concept of slip springs(SS) to force the reptation motion of polymers.

In our implementation of the slip springs, slip springs exist in pairs. Each pair of slip springs consist of two rings, which are attached to different polymer beads belonging to different chains. The slip springs move only along the polymer chains and are deleted only when the slip springs move out of the chain ends.

The slip springs are introduced in the grand canonical ensemble. Instead of fixing the number of slip springs in the simulation, we allow the number of slip springs to fluctuate around the local equilibrium number, which is dependent on the fugacity parameter β and the local density of polymer beads $\rho(\mathbf{r})$. With fixed density, lower β means lower equilibrium slip springs number. The dynamics of the polymers and slip springs are updated simultaneously in a hybrid scheme. After every time interval τ_{ss} of the integration process, slip springs are updated in the system in the grand canonical ensemble. The time interval τ_{ss} governs the entanglements effect of the slip springs. The larger τ_{ss} means the slip springs are updated less frequently. When the τ_{ss} is infinite, which means the slip springs is never updated, the polymer chains would form cross-link network.

The slip-spring potential is modeled by a harmonic spring potential, with energy given by

$$\frac{\mathcal{H}_{ss}}{k_B T} = \sum_{k=1}^{N_{ss}} \frac{u_{ss}(\mathbf{r}_k)}{k_B T} = \frac{3}{2} \sum_{k=1}^{N_{ss}} \frac{\mathbf{r}_k^2}{b_{ss}^2} \tag{2.18}$$

where r is the distance between two ends of the slip spring pair. N_{ss} is the instantaneous total number of pairs of slip springs in the system. The instantaneous total number of slip springs in the system is $2N_{ss}$. b_{ss} characterizes the average length of the slip springs.

The next step is to define algorithms governing the evolution of slip springs. After every time interval τ_{ss}, with the probability of $\frac{N\beta}{2+N\beta}$ we choose to displace a randomly chosen slip spring. Otherwise, with the probability of $\frac{2}{2+N\beta}$ we choose the add a slip spring to a random chain end, which shouldn't be occupied by another slip spring. The updating process is repeated (N_{ss}+2n) times in one updating session, where n is the number of chains in the nanocomposites.

In the displacement updating session, a random end of a randomly chosen slip spring is moved discretely to the neighboring beads if the slip spring end does not attempt to move out of the chain. This displacement move is accepted with Metropolis criterion $P_{accept}(\mathbf{r} -> \mathbf{r'})$=min(1,$e^{-\frac{u_{ss}(\mathbf{r'})-u_{ss}(\mathbf{r})}{k_B T}}$), where $u_{ss}(\mathbf{r'})$ is the slip spring energy in the new position and $u_{ss}(\mathbf{r})$ is the slip spring energy in the old position. If the slip spring moves

out of the chain end, that slip spring will be destroyed with probability $\min(1,\frac{4.0*N_{ss}}{nN\beta^2W})$, where W is the Rosenbluth factor calculated based on the local density. The formula of W is given by:

$$W = \sum_{bead\ i} \mathbf{e}^{u_{ss}(\mathbf{r}_i)/k_BT} \tag{2.19}$$

where i is the i^{th} bead which hasn't been occupied by any slip spring within the cut of radius r_c^{ss}, where r_c^{ss} is the maximum length of a slip spring the slip-spring creating process can create. The other end of original slip spring, which is not attached to the polymer chain end, in the deleting process is also considered as an unoccupied bead in Equation (2.19) in order to satisfy the detailed balance restriction. In our simulation, we set $r_c^{ss} = 2.5b_{ss}$. If the length of the original slip spring is larger than r_c^{ss}, the slip spring would not be deleted because no slip-spring-creating process in our simulation cannot create the slip spring with the length larger than r_c^{ss}. If the slip spring is not deleted when it tends to move out of the chain end, it would be kept unchanged at the chain end.

In the creating session, a random chain end which is not occupied by another slip spring is chosen to add one end of a slip spring on. If the chain end has already been occupied, the creating process will end immediately. If the end is empty, with probability $\mathbf{e}^{u_{ss}(\mathbf{r}_m)/k_BT}/W$ a random bead denoted m within the distance of r_c^{ss} around the chain end is chosen as the candidate for the other end of the slip spring. The W is the Rosenbluth factor calculated by summing $\mathbf{e}^{u_{ss}/k_BT}$ of all possible beads within the cut of radius r_c^{ss}, which is shown in Equation (2.19). Then, with the probability $\min(1,\frac{nN\beta^2W}{4*(N_{ss}+1)})$ the slip spring pair will be added on the chain end and the chosen m bead. In equilibrium, the average number of slip springs per chain in pure entangled homopolymer melts should be given by $\langle Z\rangle = (\mathrm{N}\beta W+1)/(\beta W+1)$-1. Figure 2.4 gives the comparison of the average number of slip springs per chain in simulation and the corresponding theoretical value from the single chain theory by Schieber [54].

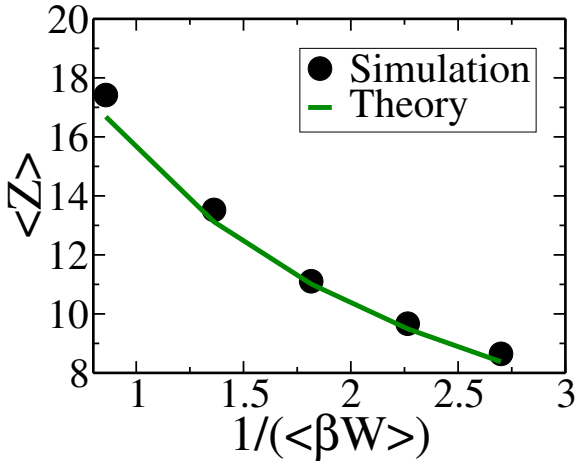

Figure 2.4: The average number of slip springs per chain in simulation and the corresponding theoretical value. The theoretical value is calculated with the following formula: $\langle Z \rangle$ = (NβW+1)/(βW+1)-1.

With the introduction of slip springs, the BD equation of motion in Equation (2.15) will be altered in the following form

$$\nu_{bead}\frac{d\mathbf{r}_j(t)}{dt} = \mathbf{f}_j(t)_{bond} + \mathbf{f}_j(t)_{nb} + \mathbf{f}_j(t)_{ss} + \mathbf{f}_j(t)_{hc} + \boldsymbol{\zeta}_j(t) \tag{2.20}$$

The meaning of the previous terms in this equation is the same as in Equation (2.15), except that we have now added a new term $\mathbf{f}_j(t)_{ss}$, which is the forces associated with the slip-spring that affect the motion of the jth bead. The analytical expression of $\mathbf{f}_j(t)_{ss}$ can be easily derived from Equation (2.18).

The slip springs introduce an additional attractive potential between the chains, which would lead to 'swelling' of polymer chains in the limit of low polymer concentrations. The low concentration limit, however, is not related to this work because such a system would no longer be entangled. To exactly compensate for the additional attractions introduced by slip springs, a compensating potential is in need to cancel the effect of the slip-springs on the thermodynamics. Chappa et al[55], for example, have deduced a functional form of that potential which can be shown in the form of v$_{eff}(\mathbf{r})$ = Ck$_B$Te$^{-u_{ss}(\mathbf{r})/k_BT}$, where C is a constant and $\mathbf{r}$ is the distance between polymer beads. Uneyama and Masubuchi[56]

also have introduced similar compensating potential to compensate the effects of slip springs. In the systems of this work, the structure and thermodynamic properties are found to be unaltered by the introduction of the slip springs. The results presented in this work do not include the compensating potential.

2.6 A Single Nanoparticle System

2.6.1 Radial Distribution Function

First, we study the influence of a single nanoparticle on the local structure of the polymer melts and the slip springs. The system is set up with entangled homopolymer($\beta = 1/160$, N = 32 and $\sqrt{N} = 96.41$) and a single nanoparticle with different radii. The average number of slip springs per chain is approximately 6.43. In Figure 2.5a) we compute the radial distribution function of the polymer bead surrounding the nanoparticle: $g_{n2p}(r)$ and the radial distribution function of the slip springs surrounding the nanoparticles: $g_{n2s}(r)$. Four sizes of nanoparticles are explored. By comparing the $g_{n2p}(r)$ and the $g_{n2s}(r)$, we can notice that the relative density of the slip springs is lower than the relative density of the polymer beads in the vicinity of all sizes of nanoparticles. It means that the polymer chains are less entangled in the region close to the nanoparticle surface than in the bulk. One possible explanation could be that the Rosenbluth number W in the vicinity of nanoparticles surface is lower than the W in the bulk because the existence of the nanoparticles reduces the number of possible sites to create the slip springs on. For large nanoparticles, the depletion layer where the density of the polymer beads is lower than that in the bulk also decrease the W surrounding the nanoparticles. The depletion layer is a result of the entropy effects as polymer chains have more possible conformations in the bulk than that in the vicinity of the nanoparticle surface, which leads to lower density of polymers surrounding large nanoparticles. By Dividing $g_{n2s}(r)$ by $g_{n2p}(r)$, we can get the radial distribution probability function: $Pr_{ss}(r)$, which is plotted in Figure 2.5 b). The physical meaning of $Pr_{ss}(r)$ is the relative probability for a polymer bead to get entangled compared with the probability of being entangled in the

bulk. Figure 2.5 indicates that large nanoparticles has stronger effect to get the polymer chains unentangled in the vicinity of the nanoparticle surface than the small nanoparticle. One of the possible reasons could be that the large nanoparticle has a stronger depletion layer than that of small nanoparticles which reduces the density of polymer beads. The other reason is that the large nanoparticle can decrease the W by occupying more volume, which otherwise could be spots for adding slip springs. Since a small single nanoparticle has less volume and less depletion effect, the probability of creating slip springs would be much higher.

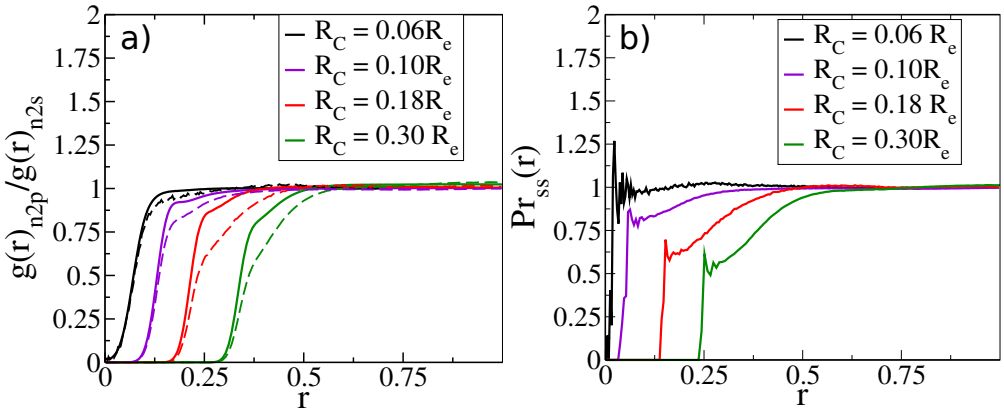

Figure 2.5: a) Solid line is g_{n2p} and dashed line is g_{n2s}. b) The relative probability radial distribution function:$Pr_{ss}(r)$ for different sizes of nanoparticles.

Figure 2.6a) gives the radial distribution function of polymer chain ends surround a single nanoparticle: $g_{n2e}(r)$ and Figure 2.6b) gives the distribution of slip springs along the chain in the vicinity of the single nanoparticle. In Figure 2.6a), unlike $g_{n2p}(r)$, the chain ends distribute much more homogeneously outside the nanoparticles and no significant depletion layer is observed in the radial distribution of polymer chain ends $g_{n2e}(r)$ even for large nanoparticles. In Figure 2.6b), we then calculate the distribution of slip springs, which are close to the surface of the single nanoparticle, along the chains. The x(ss)/N, which is the relative position of a slip spring along the chain, is recorded only if they are within the distance of R_C+0.1R_e to the center of the nanoparticle in Figure 2.6b). We choose the distance of 0.1R_e such that the depletion layer exists in the region of interest.The slip springs still distribute homogeneously within the range of

R_C+0.1R_e to the center of the nanoparticle.

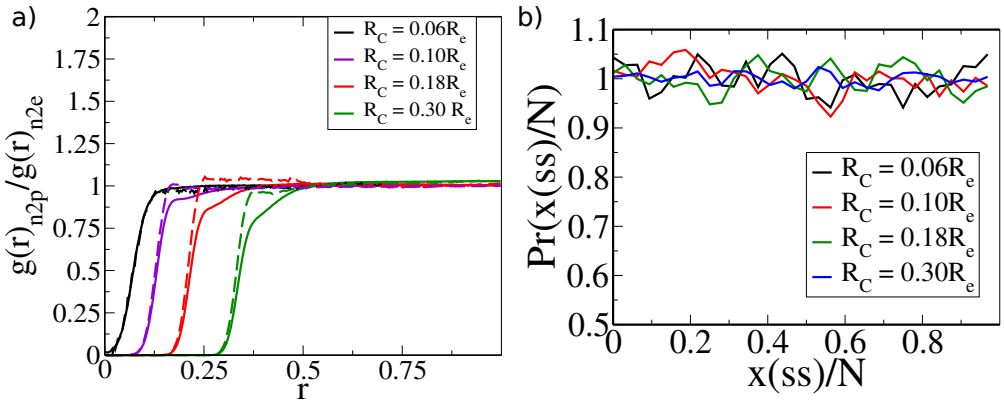

Figure 2.6: a) Solid line is $g_{n2p}(r)$ and dashed line is $g_{n2e}(r)$. b) The distribution of slip springs, which are within the distance of R_C+0.1R_e to the center of the nanoparticle, along the chains in the single nanoparticle system.

2.6.2 Diffusion of A Single Nanoparticle

We then examine the diffusion process of a single nanoparticle. We focus on two aspects of the nanoparticle: the affinity of the nanoparticles to polymers and the size of the nanoparticle . Table 2.1 shows parameters characterizing the unentangled and entangled nanocomposites systems, where D_{NP} is defined in the linear region as $g_2(t)/(6t)$ in the unit of D_0 and $D_0 = k_BT/\nu_{bead}$(see text above). As shown in Figure 2.7, the emerging entanglement constraints reduce the diffusion coefficient of nanoparticles. The larger the size of the nanoparticle is, the more extent the diffusion coefficient will be reduced. There is also 'caging' effect by the entanglement mesh on nanoparticles in the intermediate time, and this effect grows as the nanoparticles become bigger(or the entanglement mesh size becomes smaller). Such anomalous behavior ($\Delta\ r^2 \sim t^\beta, \beta$<1) also has been seen by Guo *et al.* [46], Omari et al [47]. Wong *et al.* [48], Amblard *et al.* [57], Cai *et al.* [28], and Kalathi *et al.* [49]. These last workers [49] studied the time-dependent nanoparticles mean-squared displacement for a series of particles sizes. And they reported the minimum apparent exponent, defined locally as $g_2(t) \sim t^x$, varies from x $\sim$ 1 for the smallest particle to $\sim$ 0.4 for the largest particle. This 'caging' region arises from transient trapping and

slowing down of particles motion due to emerging entanglement constraints. Therefore, we can estimate the order of magnitude of the entanglements mesh size by the range of the 'caging' region in Figure 2.7. In Figure 2.7, since the nonlinear region in the diffusion process is in the range of $0.01R_e^2$–$0.1R_e^2$, the size of the mesh formed by the slip springs is estimated to be $0.1R_e$–$0.3R_e$. In our simulation, the diffusion is non-linear in the 'caging' space with power law $g_2(t) \sim t^x$, varies from x$\sim$0.93 for the small nanoparticle and x$\sim$0.30 for the large nanoparticle. After the nanoparticle escapes the 'caging' region, the diffusion recovers the linear region. The surface energy of the nanoparticle also plays a crucial role in the diffusion of the intermediate nanoparticle. When the size of the nanoparticle is small($t^x \sim t^{0.93}$), changing the nanoparticle from neutral($\Lambda_S = 0.0$) to attractive(Λ_S = -2.0) only increase the diffusion coefficient of the nanoparticle since there is no 'caging' effect. When R_C is comparable to the size of the mesh formed by entanglements, where $t^x \sim t^{0.52}$ in the 'caging' region, modifying the surface energy from neutral to attractive not only increases the diffusion coefficient but also changes the scaling of diffusion to $t^{0.74}$ in the 'caging' region. However, when the size of the nanoparticle becomes much bigger than entanglements mesh size, the scaling in the 'caging' region is not affected much by modifying the affinity from neutral to attractive, though the diffusion coefficient is still improved. The reason could be that the size effect is the dominant factor in this case and simply changing the affinity of nanoparticles is difficult to moderate the physical constraints imposed by the entanglements mesh on the nanoparticle since the size of nanoparticles is too big. In general, the attractive affinity to polymer beads increases the diffusivity of the nanoparticle. And such a phenomenon is also observed when the entanglements of polymer chains are removed, which is shown in Figure 2.8. The attractive surface makes the nanoparticle more likely to mingle with the polymer melts and this increases the diffusivity no matter whether the entanglements exist or not. We also noticed that when $R_C = 0.1\ R_e$, the entanglements cannot change the diffusion process of the nanoparticle and the diffusion curve in Figure 2.7 and Figure 2.8 can almost overlap. However, when the size of the nanoparticle increases, the entanglements of polymers would slow down the diffusion process of the nanoparticle.

Table 2.1: Parameters Characterizing a Single Neutral or Attractive Nanoparticle with Different Sizes in Entangled Polymer Melts.

N	n	$\sqrt{\bar{N}}$	n_{NP}	R_C	ϕ_{NP}	D_{NP}	Λ_S
32	1331	96.41	1	$0.10R_e$	0.083%	$0.02352D_0$	0.0
32	1481	96.41	1	$0.18R_e$	1.68%	$0.0002687D_0$	0.0
32	4112	96.41	1	$0.30R_e$	0.5%	$3.6032E\text{-}5D_0$	0.0
32	1331	96.41	1	$0.10R_e$	0.083%	$0.02544D_0$	-2.0
32	1481	96.41	1	$0.18R_e$	1.68%	$0.001186D_0$	-2.0
32	4112	96.41	1	$0.30R_e$	0.5%	$4.1683E\text{-}5D_0$	-2.0

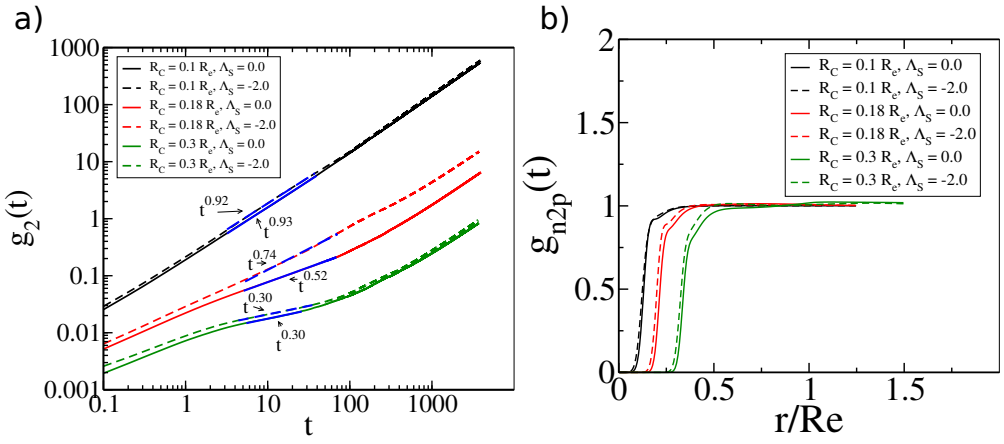

Figure 2.7: a) Time evolution of the mean-square-displacement for a single nanoparticle with different sizes and affinities. Slip springs reduce the diffusivity of nanoparticles even though they are not directly attached to the nanoparticles. b) The radial distribution function g_{n2p} of the nanoparticle with different sizes and affinity.

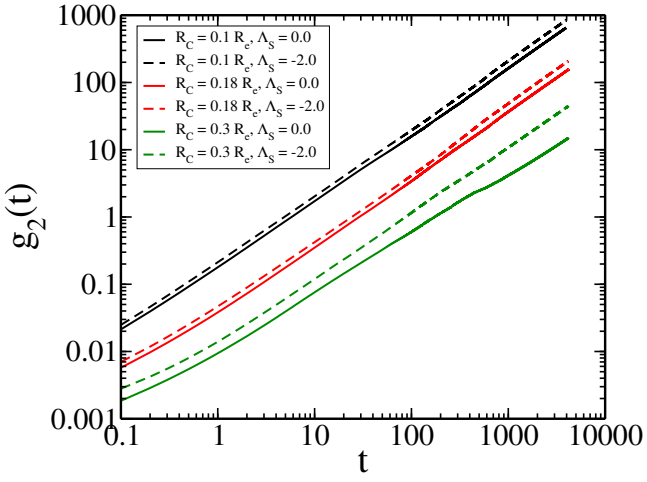

Figure 2.8: Time evolution of the diffusion process for a single nanoparticle with different sizes and affinities. The parameters are the same as Table 2.1, except that the polymers are unentangled.

2.7 Loaded Nanocomposites

After study of a single nanoparticle system, we then examine the behaviors of loaded nanocomposites. The first property we focus is how the volume fraction of nanoparticles affect the the statistics of slip springs.

2.7.1 Slip Springs in Loaded Nanocomposites

The Z, Q, M are introduced in the theoretical work of Schieber [58] as a way to measure the entanglements formed by slip springs. Z is the number of slip springs distributed on any random chain. CP(Z) is the cumulative probability density that a chain has Z slip springs on it. Q is the distance between two neighbor slip springs on a chain and M is the number of beads between two neighbor slip springs on a chain. We use neutral($\Lambda_S = 0.0$) nanoparticles with $R_C = 0.18R_e$ as a representative to study the influence of nanoparticles volume fraction on the slip springs distributions. With the radius of the nanoparticles comparable to the length of the polymer bonds, the polymer bond cannot cross the center of nanoparticles directly. Also, from the diffusion calculations in Figure 2.7, we notice that the size of the mesh formed by entanglements is approximately $0.2R_e$. Therefore,

nanoparticles with $R_C = 0.18R_e$ can be treated as intermediate nanoparticles, which show 'caging' effect during the diffusion process of nanoparticles in entangled polymer melts. Particles with $R_C = 0.1R_e$ are too small as it can cross the entanglement mesh without showing any 'caging' effect. However, even though the size of nanoparticles affects some properties significantly, its influence on the slip springs distribution is negligible as long as the the R_C of nanoparticles are smaller than r_c^{ss}, which is $2.5b_{ss}$=$0.45R_e$ in our work. When the R_C of nanoparticles is larger than r_c^{ss}, the surface area of the nanoparticles replaces the volume fraction as the dominating factor in determining the ensemble average Rosenbluth factor of the nanocomposites system since the increase of the volume beyond the distance r_c^{ss} to the surface of the nanoparticles cannot be felt by the slip-springs creating or deleting process any more, as shown in Figure 2.9. Therefore, when the R_C of nanoparticles is larger than r_c^{ss}, which is $0.45R_e$ in our system, large-size particles will decrease $\langle Z \rangle$ less than small-size particles with the same volume fraction. However, that is not the case in our discussion since the R_C in our work is small enough and the volume fraction of nanoparticles is still the dominating factor in determining $\langle Z \rangle$ of the entangled nanocomposites. Theoretically, r_c^{ss} could be infinite. However, the possibility of creating a slip spring beyond r_c^{ss} is so small and therefore, the W decreased by large nanoparticles beyond r_c^{ss} is also negligible. So the size of the r_c^{ss} doesn't change the conclusion. In Figure 2.11 we give the Q, Z, M distribution when the R_C of nanoparticles are $0.18R_e$ as a representative. The distributions are similar for particles with $R_C = 0.1R_e$ and $R_C = 0.3R_e$. Figure 2.11 a) shows that Q distribution shifts to the right with more nanoparticles. It means that there is an increase of distance between two neighboring slip springs. Figure 2.11 b) shows that M distribution also shifts to the right, which means there are more beads between neighboring slip springs as the volume fraction of nanoparticles increases. All of those two plots are consistent with Figure 2.11 c), which shows the number of slip springs per chain shifts to a smaller value as the volume fraction of nanoparticles increase. Figure 2.11 d) demonstrates that the addition of nanoparticles does not alter the distribution of slip springs along the chain, and the distribution remains homogeneous. Figure 2.10 gives the ensemble average value of Z and W as a function of

the volume fraction of nanoparticles with three different radii $R_C = 0.30\ R_e$, $R_C = 0.18\ R_e$ and $R_C = 0.10\ R_e$. When the volume fraction of nanoparticles increases, the average number of slip springs per chain decreases and the influence of the nanoparticles' size on this trend is negligible. This is because the number of possible sites to create the other end of slip springs decreases linearly with the volume fraction of nanoparticles, which leads to a decrease of $\langle W \rangle$, as shown in Figure 2.10b). The decrease of $\langle W \rangle$ directly leads to the decrease of the probability of creating slip springs and the increase of the probability of deleting slip springs.(see text in **Entanglement** section) Therefore, the average slip springs per chain would decrease ultimately and the system becomes less entangled with the addition of nanoparticles. Please be noted that when the size of nanoparticles is larger than r_c^{ss}, nanocomposites with large-size nanoparticles would have more slip springs than that of nanocomposites with small-size nanoparticles given the same volume fraction of nanoparticles since surface area is the dominating factor in calculating the Rosenbluth factor.

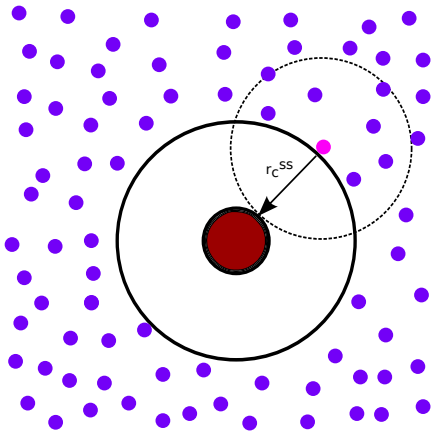

Figure 2.9: The purple circle represents the polymer beads. The pink circle represents one end of the slip spring in the slip-spring creating or deleting process. The large circle represents one single nanoparticles. The red region of the nanoparticle cannot influence the creating or deleting process of slip springs when the size of nanoparticle continuous to increase.

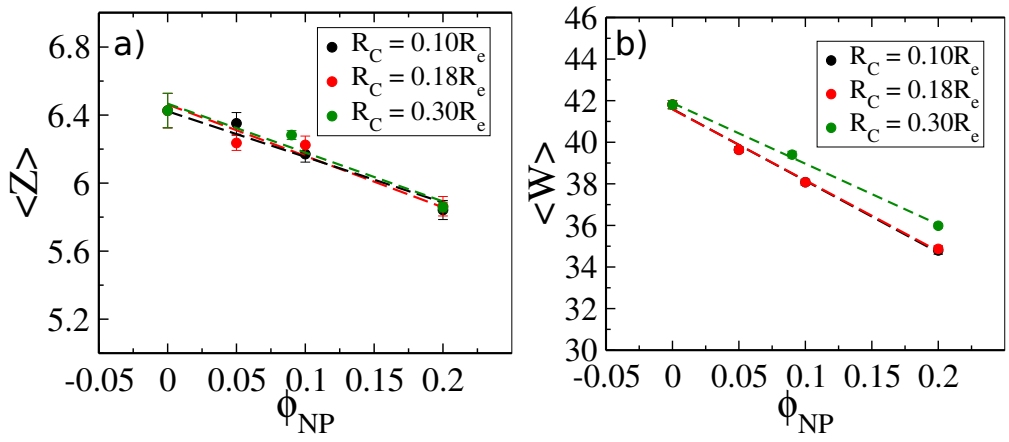

Figure 2.10: The ensemble average of Z in a) and W in b) as a function of volume fraction with different sizes of nanoparticles.

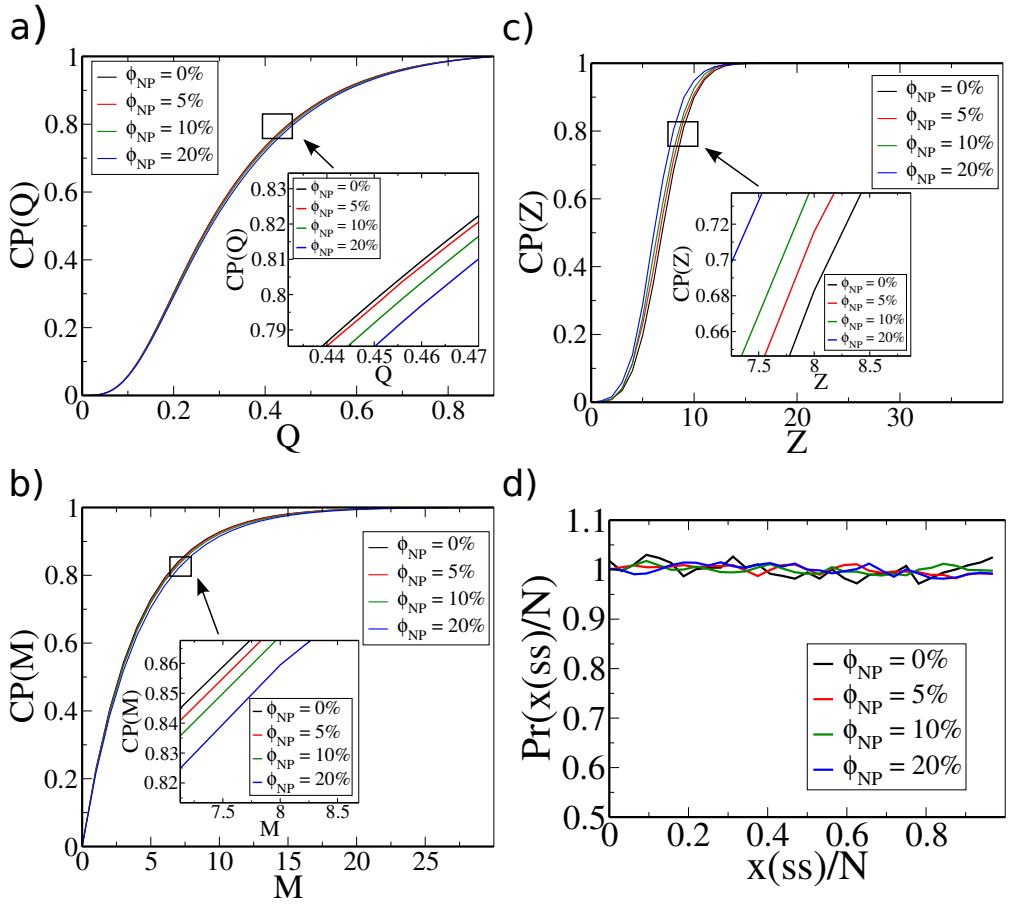

Figure 2.11: a) The Z distribution in different volume fraction of nanoparticles(0%,5%,10% and 20%). b) The Q distribution in different volume fraction of nanoparticles. c) The M distribution in different volume fraction of nanocomposites. d) the distribution of slip springs on a chain, where x(ss) is the bead sequence number that a slip spring resides on.

2.7.2 Diffusion in the Loaded Nanocomposites.

Diffusion of Polymers We begin our discussion by comparing the behavior of polymers in unentangled and entangled nanocomposites melts. The nanoparticles are neutral(Λ_S = 0.0) and $R_C = 0.18\ R_e$.Figure 2.12 shows results for the mean-square displacements, $g_1(t)$ and $g_3(t)$ for different volume fractions of nanoparticles without slip springs. Figure 2.13 corresponds to the same calculations in systems with slip springs ($\langle Z \rangle$ = 6.43 and τ_{ss} = 0.5). Table 2.2 and Table 2.3 show parameters characterizing the unentangled and

entangled nanocomposites respectively, where τ is the longest relaxation time defined as $\tau = R_e^2/D$. D is the diffusion coefficient of the chain's center of mass by the long-time behavior of $g_3(t)$.

Figure 2.12 and Table 2.2 show that in unentangled nanocomposites, the longest relaxation time increases with the introduction of nanoparticles. The diffusivity of polymer beads are decreased slightly in Figure 2.12. The reason is that the nanoparticles act as confinement points to chain motion and the diffusion of polymer beads is not as free as it is in the bulk with the introduction of nanoparticles. The same constraint is also felt by the nanoparticles with more and more nanoparticles are introduced in unentangled nanocomposites, which is shown in Figure 2.14.

Table 2.2: Parameters Characterizing the Unentangled Polymer Nanocomposites.

N	n	$\sqrt{\bar{N}}$	n_{NP}	R_C	ϕ_{NP}	τ
32	1506	96.41	0	$0.18R_e$	0%	34.26
32	1436	96.41	11	$0.18R_e$	5%	34.60
32	1361	96.41	23	$0.18R_e$	10%	36.36
32	1209	96.41	47	$0.18R_e$	20%	38.32

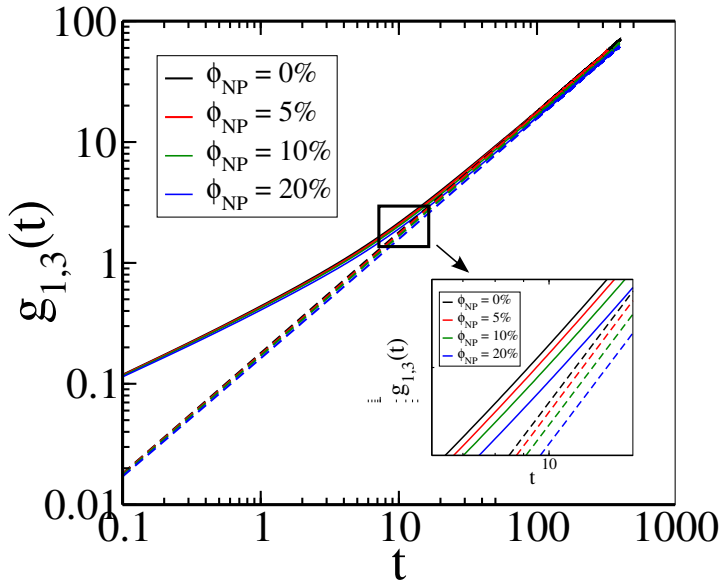

Figure 2.12: Time evolution of the mean-square-displacement for beads($g_1(t)$, solid lines) and center of mass of the chains($g_3(t)$, dashed lines) for different volume fractions of nanoparticles without slip springs. The diffusion curves shift down with the addition of nanoparticles, which means a decrease of diffusivity.

Unlike the unentangled nanocomposites, the entangled nanocomposites show totally different behaviors because there is competition between the nanoparticles confinement barriers and the decrease of entanglements density with the addition of nanoparticles. In Figure 2.13 and Table 2.3, the polymer beads and chains diffuse faster with the addition of nanoparticles. This is because when the volume fraction of nanoparticles increases, decrease of entanglements(Figure 2.10) has replace the nanoparticles confinement barriers as the dominating factor in determining the diffusion process of polymer beads. And the polymer beads have higher diffusivity with fewer entanglements. Therefore, in entangled nanocomposites, both the polymer beads in Figure 2.13 and small-size nanoparticles in Figure 2.14 demonstrate higher diffusivity with the addition of nanoparticles.

Table 2.3: Parameters Characterizing the Entangled Polymer Nanocomposites.

N	n	$\sqrt{\bar{N}}$	n_{NP}	R_C	ϕ_{NP}	τ
32	1506	96.41	0	$0.18R_e$	0%	8378.02
32	1433	96.41	13	$0.18R_e$	5%	8039.55
32	1361	96.41	26	$0.18R_e$	10%	7318.50
32	1210	96.41	53	$0.18R_e$	20%	6108.67

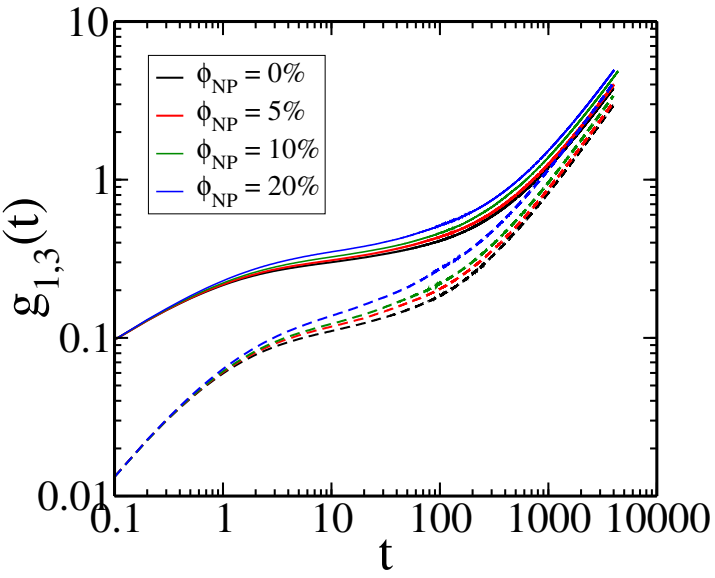

Figure 2.13: Time evolution of the mean-square-displacement for beads(g_1(t), curve lines) and center of mass of the chains(g_3(t), straight lines) for different volume fractions of nanoparticles with slip springs. The diffusion curves shit up with the addition of nanoparticles, which means an increase of diffusivity.

Diffusion of Nanoparticles

In Figure 2.14a), We inspect the diffusion of nanoparticles in systems characterized by Table 2.2 and Table 2.3. The increase of nanoparticles volume fraction leads to the decrease of the neutral nanoparticles diffusivity in both unentangled and entangled nanocomposites because of the barriers imposed by the excluded volume of nanoparticles. This is different from the diffusion of polymer beads in the entangled nanocomposites in Fig-

ure 2.13, where the effect of entanglements density decrease is the dominating factor since the excluded volume effect on polymer beads is small. However, if we change the size of the nanoparticles to 0.1 R_e, the result would be the same as Figure 2.13. As shown in Figure 2.14b), we plot the diffusion of nanoparticles with $R_C = 0.1\ R_e$. Though the diffusivity of the nanoparticles in the rouse polymer melts still decreases with the addition of nanoparticles, the diffusion coefficient of the corresponding nanoparticles in entangled polymer melts increases as the volume fraction of nanoparticles increases. Similar to the polymer diffusion in Figure 2.13, the reason lies in the fact that the number of entanglements decreases due to the introduction of nanoparticles and it shows up in the diffusion of small-size nanoparticles since small-size nanoparticles have less barriers in diffusion due to small excluded volume.

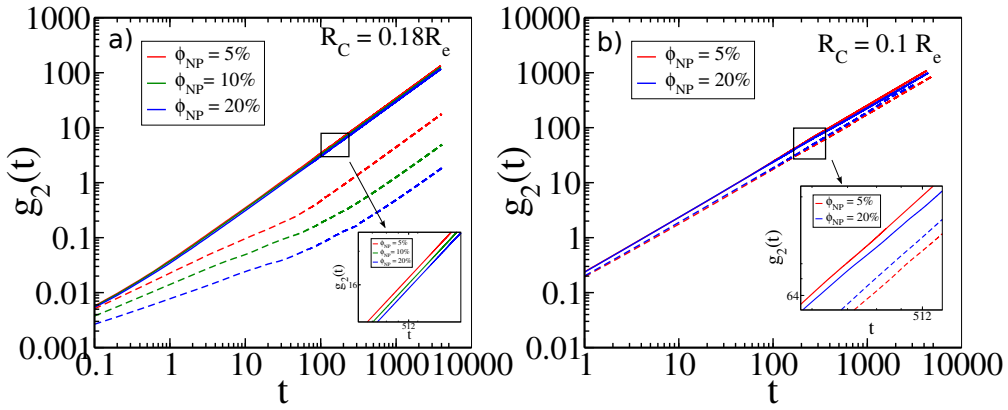

Figure 2.14: Time evolution of the mean-square-displacement for nanoparticles with/without slip springs. The solid line is the result of neutral nanoparticles in rouse polymer melts, and the dashed line is the result of neutral nanoparticles in entangled polymer melts. The left Figure a) is nanoparticles with core radius $R_C = 0.18\ R_e$ and the right Figure b) is the nanoparticles with core radius $R_C = 0.1R_e$.

2.7.3 Linear Rheology of the Loaded Nanocomposites.

To characterize the response of nanocomposites linear rheological properties to the volume fraction of nanoparticles, we compute the stress relaxation function defined by

$$G(t) = \frac{G_{xy}(t) + G_{yz}(t) + G_{xz}(t)}{3} \tag{2.21}$$

$$G_{\alpha\gamma}(t) = \frac{V}{k_B T} < \sigma_{\alpha\gamma}(t)\sigma_{\alpha\gamma}(0) > \tag{2.22}$$

The system stress is given by

$$\sigma_{\alpha\gamma}(t) = \sigma_{\alpha\gamma}(t)_{bond} + \sigma_{\alpha\gamma}(t)_{nb} + \sigma_{\alpha\gamma}(t)_{ss} + \sigma_{\alpha\gamma}(t)_{hc} \tag{2.23}$$

$$\sigma_{\alpha\gamma}(t)_{\mathbf{x}} = \frac{k_B T}{V} \sum_{i=1}^{(nN+n_{NP}-1)} \sum_{j=i+1}^{(nN+n_{NP})} f_{\mathbf{x}\alpha}^{ij} r_{\gamma}^{ij} = \frac{k_B T}{V} \sum_{i=1}^{nN+n_{NP}-1} \sum_{j=i+1}^{nN+n_{NP}} f_{\mathbf{x}\gamma}^{ij} r_{\alpha}^{ij} \tag{2.24}$$

where ($\alpha/\gamma \in$ {x ,y ,z}), (**x**=bond, nb, ss, hc) and $G_0 = k_B TnN/V$. $f_{\mathbf{x}\alpha}^{ij}$ means the force of type **x** between i^{th} bead and j^{th} bead in the α direction at time t. r_{α}^{ij} is the distance between the i^{th} bead and j^{th} bead in the direction of α at time t. The bead in the Equation (2.24) is either a polymer bead or a nanoparticle. The sequence of nanoparticles is appended after the sequence of polymer beads in this equation. For example, the j^{th} nanoparticle is treated as the $(nN+j)^{th}$ bead.

To characterize the contributions to the total stress correlation function from different types of forces, we also define the sub-component stress correlation function in Equation 2.25 and the cross stress correlation function in Equation 2.26:

$$G_{\alpha\gamma}(t)_{\mathbf{x}} = \frac{V}{k_B T} < \sigma_{\alpha\gamma}(t)_{\mathbf{x}}\sigma_{\alpha\gamma}(0)_{\mathbf{x}} > \tag{2.25}$$

$$G_{\alpha\gamma}(t)_{\mathbf{x,y}} = \frac{V}{2k_B T} < \sigma_{\alpha\gamma}(t)_{\mathbf{x}}\sigma_{\alpha\gamma}(0)_{\mathbf{y}} + \sigma_{\alpha\gamma}(0)_{\mathbf{x}}\sigma_{\alpha\gamma}(t)_{\mathbf{y}} > . \tag{2.26}$$

The shear viscosity η, is computed from the stress relaxation function through the

Green-Kubo relation.

$$\eta = \int_0^\infty G(t)dt \tag{2.27}$$

It was predicted by Einstein nearly a century ago that particle addition to liquids produces an increase in viscosity, even in polymeric liquids. However, it is experimentally observed in Mackay *et al.* [32] that the addition of small-size nanoparticles reduces the blend viscosity. The average radius of crosslinked M_r 52k nanoparticles in is 2.7nm and the M_r 75K undiluted linear polystyrene has the radius of gyration(R_g) 7.5-15nm, where M_r represents the Molecular Weight. Therefore, if the relation: $6R_g^2 = R_e^2$ holds, the nanoparticles in experiments are of order 0.07-0.15R_e, which is similar to the size of nanoparticles in our model. Also M_r 75k polystyrene has approximately 4.7 entanglements per chain, which is close to that of our system.

This unusual polymer dynamics is captured by our model, as shown in Figure 2.15. However, our model also predicts a decrease of entanglements which is not observed in the work of Mackay *et al.* [32] Their argument is that if the viscosity reduction were caused by an increase in the entanglement molecular weight, both the plateau modulus and the viscosity should decrease. But they observed that the average of plateau modulus for all concentrations is approximately the same. We use N = 32, $\beta = 1/160$ and $\tau_{ss} = 0.5$ as the parameters in the study of the entangled nanocomposites, which generates the entanglements per chain $\langle Z \rangle = 6.43$.

The simulation box size is set to $(2.5\ R_e)^3$, which is big enough to exclude any size issues in the periodic boundary conditions since we only consider nanoparticles with $R_C = 0.18R_e$.

In Figure 2.15, we study the stress relaxation function G(t) of neutral nanoparticles($R_C = 0.18R_e$) with different volume fraction. The overall G(t) decays faster with the addition of nanoparticles, which indicates a non-Einstein-like decrease in the shear viscosity. The experimental work of Mackay *et al.* [32] confirms this phenomenon. However, when the slip springs are removed, such a dramatic viscosity decrease phenomenon cannot be captured in the TICG model, as shown in Figure 2.16. To arrive at a direct comparison

with the Rouse theory, we compute the following analytical expression:

$$G^{Rouse}(t) = \frac{G_0}{N} \sum_{p=1}^{p_{max}} e^{-6\pi^2 p^2 t/\tau} \tag{2.28}$$

where τ is the longest relaxation time in the bulk, as shown in Table 2.2.

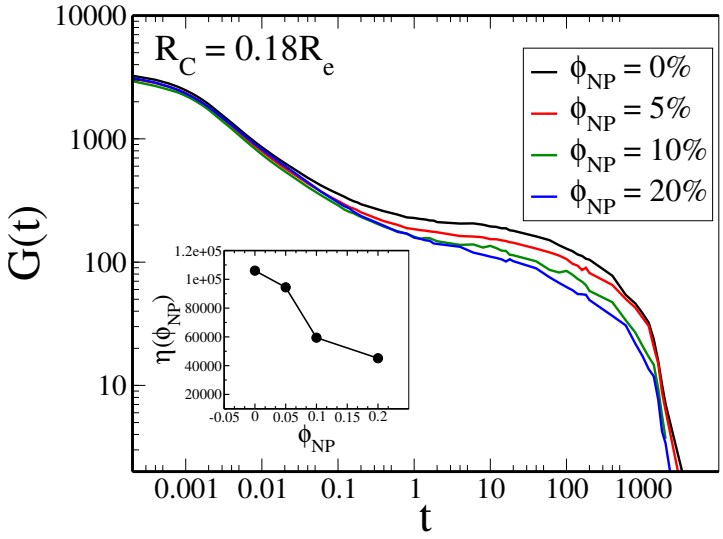

Figure 2.15: Stress relaxation function as a function of time in various volume fraction of nanoparticles in the entangled nanocomposites.

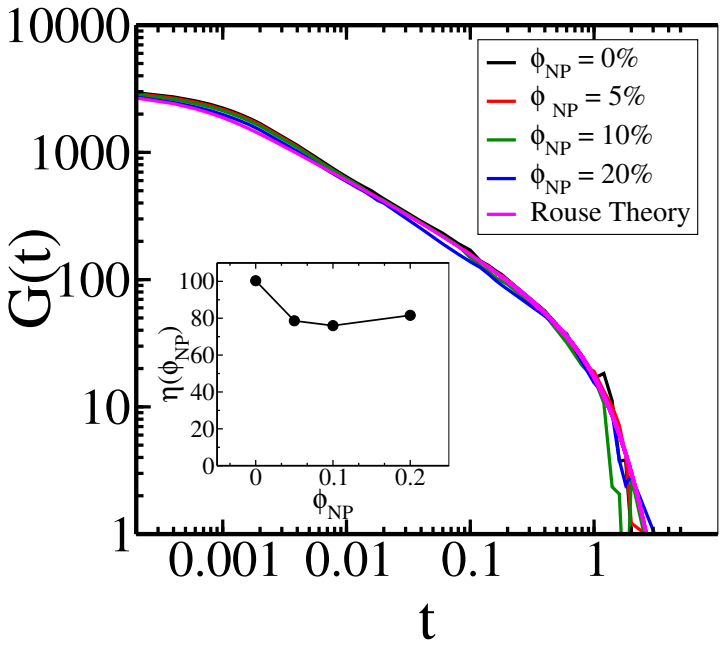

Figure 2.16: Stress relaxation function as a function of time in various volume fraction of nanocomposites in the unentangled nanocomposites.

Mackay *et al.* [32] claims that the unusual decrease in viscosity due to the addition of nanoparticles comes from the free volume introduced by nanoparticles since the entanglements seem not to be affected at all with the addition of nanoparticles. We examine this problem by decomposing the overall the stress relaxation function in Figure 2.15 at $\phi_{NP} = 20\%$ into its sub-component terms: $G(t)_{bond}$, $G(t)_{nb}$, $G(t)_{ss}$ and $G(t)_{hc}$, as shown in Figure 2.17 a). The remaining cross correlation terms: $G(t)_{bond,hc}$, $G(t)_{bond,nb}$, $G(t)_{bond,ss}$, $G(t)_{hc,nb}$,$G(t)_{hc,ss}$ and $G(t)_{nb,ss}$ are plotted in Figure 2.17 b). From Figure 2.17 b) we can notice that the cross correlation terms are negligible compared with the sub-component terms. Therefore, for simplicity we can ignore the cross correlation terms when analyzing the contributions to the total stress correlation function from each sub-component term of stress. By decomposition in to sub-component terms, we notice two points. First, in loaded nanocomposites the core stress correlation function becomes important compared with the dilute system. Second, the core stress correlation function has a much faster decay rate, which scales in $t^{-0.430}$ in Figure 2.17, than the decay rate of the G_{bond}, which scales with the power law of $t^{-0.118}$. Therefore, the increase of

the fast-decaying core stress correlation with the addition of nanoparticles is the critical free volume effect which leads to the unusual non-Einstein-like decrease in the viscosity observed by Mackay *et al.* [32].

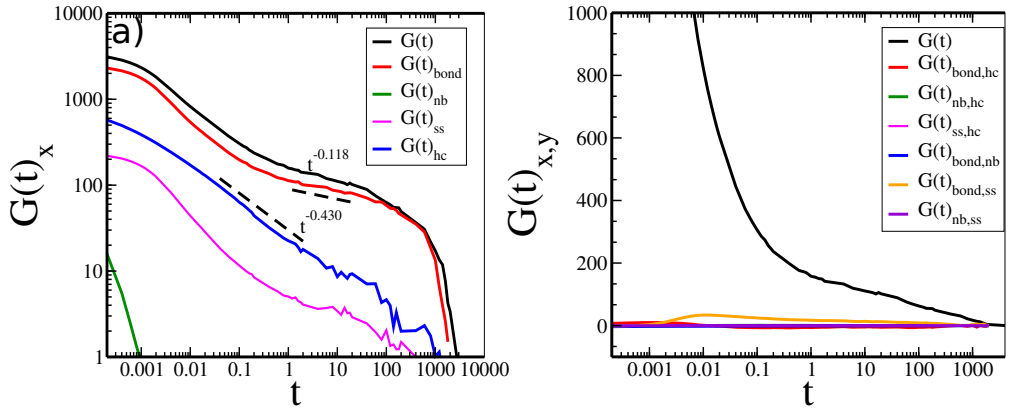

Figure 2.17: a) Sub-component stress correlation function in ϕ_{NP} =20% nanocomposites with slip springs. The G(t)$_{bond}$ decays with the power law of t$^{-0.118}$ in the plateau region, while G(t)$_{hc}$ $\sim$ t$^{-0.43}$. b) the cross correlation terms G(t)$_{x,y}$ compared with the total stress correlation G(t).

To compare with the entangled nanocomposites, we also decompose G(t) when ϕ_{NP} = 20% and the nanocomposites do not have slip springs, which is shown in Figure 2.18. Similar to Figure 2.17, the core stress relaxation function decays with the scaling of t$^{-0.55}$. However, the bond stress correlation function also decays fast, with the scaling of t$^{-0.55}$. Because the decaying speeds of the core stress correlation function and the bond stress correlation function are close, The decaying speed of the total stress correlation function is not affected by the increase of the core stress relaxation function. Therefore, the free volume effect does not show up in the unentangled nanocomposites.

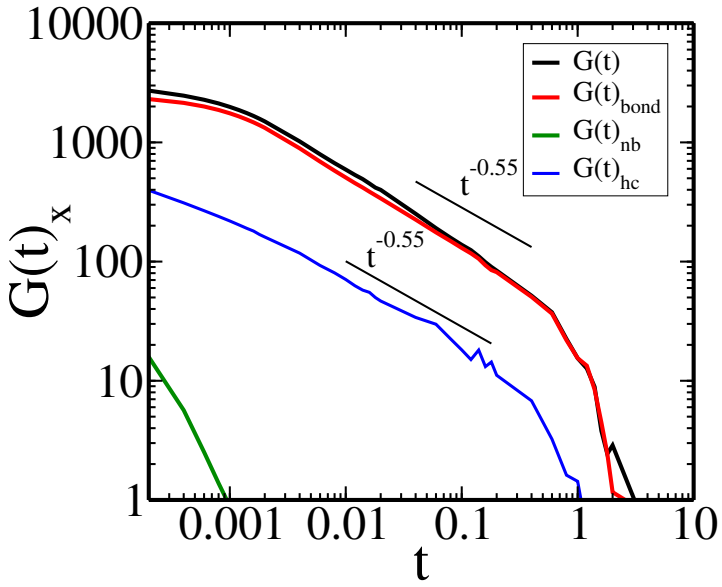

Figure 2.18: Sub-component core stress correlation function $G(t)_{hc}$ in ϕ_{NP} =20% nanocomposites without slip springs.

Besides the free volume effect, our model also predicts increase of the entanglement molecular weight M_e as the $\langle Z \rangle$ decrease with the addition of nanoparticles. As a result, the $G(t)_{bond}$ shows faster decaying speed with the decrease of slip springs. Figure 2.19 gives $G(t)_{bond}$, which are the subcomponents of G(t) from Figure 2.15.

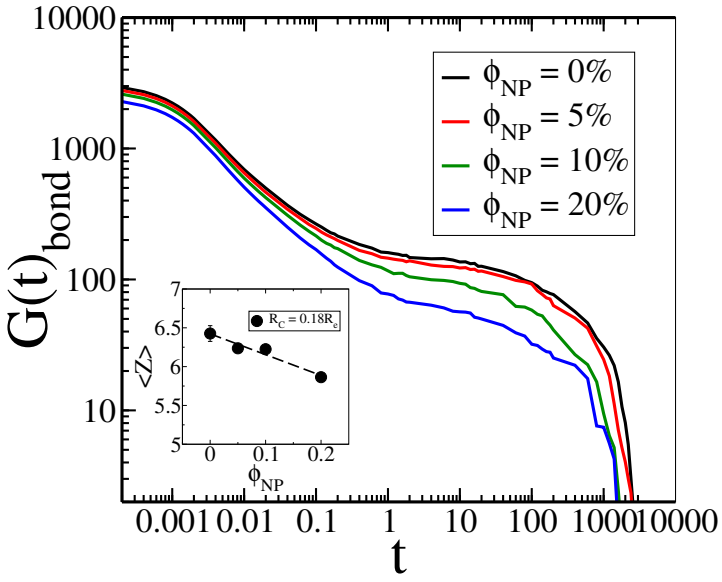

Figure 2.19: Sub-component stress correlation function $G(t)_{bond}$ in various volume fraction of $R_C = 0.18R_e$ nanocomposites with slip springs from Figure 2.15.

Up to now, we have studied the stress correlation function of $R_C = 0.18R_e$ nanocomposites. Smaller Nanoparticles, for example $R_C = 0.1R_e$, have similar behaviors as the $G(t)_{bond}$ is similar to that of the intermediate nanoparticles composite and the $G(t)_{hc}$ decays even faster. Therefore, the non-Einstein-like decrease of viscosity still holds for smaller nanoparticles. As for the large nanoparticles, because it requires huge simulation box to simulate. We did not compute the whole stress correlation function directly in this work. For example, Mackay *et al.* [32] claims that the addition of 1.6-um diameter crosslinked PS microspheres shows the conventional viscosity increase with particle addition to M_r 75K linear polystyrene. The diameter of 1.6-um corresponds to R_C = 44–88 R_e nanoparticles in our model. Even though we cannot compute the stress relaxation function directly, we can still give some estimations. Since the non-bonded stress is negligible in the calculation of the total stress correlation function, we focus on two kinds of stresses: the bonded stress together with the slip-spring stress and the core stress. Because in our algorithm, the number of slip springs in equilibrium is influenced by the average Rosenbluth number, which is directly related to homopolymer volume fraction. Therefore, the entanglement will decrease as the volume fraction of large nanoparticles increases. However, as the R_C of nanoparticles increases to 44–88 R_e, the surface area has already been the dominant factor in determining the Rosenbluth factor in nanocomposites. As 75%-87% of the nanoparticles' volume cannot effectively reduce the Rosenbluth factor when R_C is 44–88R_e, the entanglements would decrease much less for large particles than that for small particles given the same volume fraction of particles. Therefore. even though the entanglements in particles composites still decrease with the addition of particles, the extend is not as much as that of small-size nanoparticles when the size of particles enters the micro scale. On the other hand, Figure 2.20 give the sub-stress correlation function-$G(t)_{hc}$ at the volume fraction of approximate 20%. The size of the nanoparticles varies from $0.1R_e$ to $0.5R_e$. Unlike the previous definition of the nanoparticle volume fraction where we use R to define V_{NP}, we use R_C to define the volume fraction of nanoparticles in this section in ordered to make the total volumes occupied by the nanoparticles cores be the same. From Figure 2.20, we found that $G(t)_{hc}$ in the

entangled nanocomposites have slower decaying power rate than it in the unentangled nanocomposites. The difference becomes larger as the size of the nanoparticles grows. In the entangled nanocomposites, the $G(t)_{hc}$ of large nanoparticles($R_C = 0.5R_e$) has much slower decaying power rate than the small size nanoparticles($R_C = 0.1R_e$). Though the difference exists in the unentangled nanocomposites, it is especially large in the entangled nanocomposites. The decaying power rate of $G(t)_{hc}$ in the entangled nanocomposites with large nanoparticles can even be slower than the decaying power rate of $G(t)_{bond}$ when we compare the decaying power rate in Figure 2.20 and Figure 2.17. Therefore, when the size of the nanoparticles increase, the free volume effect of loaded nanoparticles even has the possibility of increasing the viscosity of the system instead of decreasing it However, the question still remains as a question how large the particles should be in order to increase the viscosity in loaded nanocomposites.

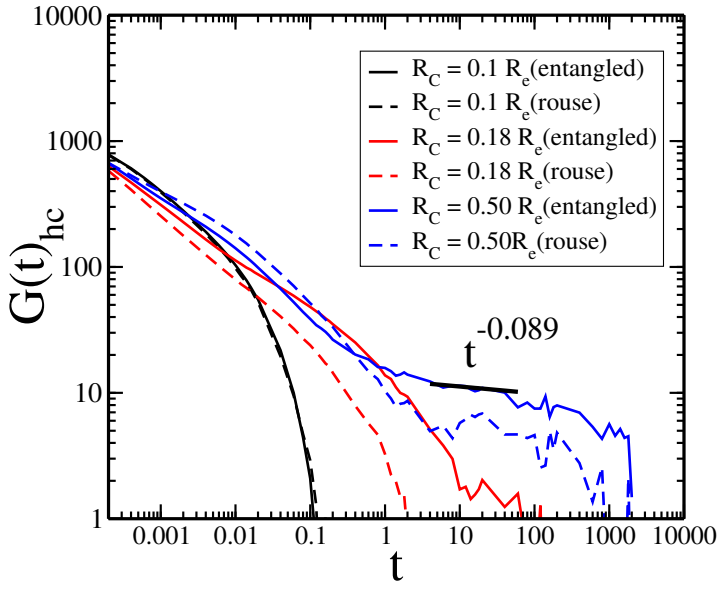

Figure 2.20: Sub-component stress correlation function $G(t)_{hc}$ with various sizes of nanoparticles at the volume fraction of 20% in the entangled and unentangled polymer melt. The volume fraction of nanoparticles calculated in this graph is defined as: $V_{NP} = \frac{4}{3}\pi\ R_C^3$.

2.8 Conclusion

In conclusion, we first studied the diffusion of a single nanoparticles in entangled homopolymers with various sizes and affinities to the polymers. When the size of the nanoparticle is comparable to or larger than the size of the entanglements mesh, the mean-square displacement of the nanoparticle shows non-linear behavior in the early stage of diffusion, which arises from the transient trapping and the slowing down of particles' motion imposed by emerging constraints of entanglements. Changing the nanoparticle affinity to polymers from neutral can increase the diffusivity of the nanoparticle and help the nanoparticle escape the nonlinear region. We then study the properties of loaded nanocomposites. As the volume fraction of nanoparticles increases, the number of entanglements would decrease. Therefore, the diffusivity of polymer beads and small nanoparticles increases with the addition of nanoparticles. However, when the size of nanoparticles is large, constraint due to the excluded volume of nanoparticles overcomes the decrease of entanglements as the dominating factor, which decreases the diffusivity of both polymer beads and nanoparticles.

Next, we study the rheology of the nanocomposites by calculating the stress correlation function and the viscosity. We focus on the $\mathrm{R}_C = 0.18\mathrm{R}_e$ nanoparticles, which is in the same order of magnitude as the R_g of the entangled polymer chains and the entanglements mesh size. The $\mathrm{G(t)}_{hc}$, which is the stress correlation function calculated by the stress related to the core potentials $\mathcal{H}_{n2p}^{Core}$ and $\mathcal{H}_{n2n}^{Core}$, has faster decaying speed than that of the $\mathrm{G(t)}_{bond}$, which is calculated from the stress related to the bond potentials $\mathcal{H}_{bond}$. Therefore, as the volume fraction of nanoparticles increases and the $\mathrm{G(t)}_{hc}$ replaces part of $\mathrm{G(t)}_{bond}$ in the contribution of the total G(t), the G(t) of the nanocomposites shows faster decaying power rate. The cross correlation terms are negligible to either $\mathrm{G(t)}_{hc}$ or $\mathrm{G(t)}_{bond}$. Another reason for the non-Einstein-like decrease in viscosity with the addition of nanoparticles in our TICG model is that the increase of nanoparticles volume fraction also decrease the number of slip springs per chain in the system. With fewer entanglements, the stress correlation function will also have faster decaying power rate. Last but not the least, we found that $\mathrm{G(t)}_{hc}$ has different decaying power rates with different sizes

of particles in the entangled nanocomposites. Large nanoparticles have longer relaxation time of $G(t)_{hc}$ in entangled nanocomposites. And the decaying power rate of $G(t)_{hc}$ in the plateau region is comparable to or even larger than that of $G(t)_{bond}$ in the plateau region. What's more, when the size of nanoparticles is large enough, the degree of the decrease of slip springs by the introduction of nanoparticles will be mitigated. Both of the two factors will make nanocomposites with large nanoparticles have higher viscosity than that of small nanoparticles systems given the same volume fraction. And it is possible that the Einstein law can be recovered in the limit of micro-size particles.

2.9 Supplementary Materials

The Dissipative Particle Dynamics(DPD) thermostat consists of the summation of conservative forces($\boldsymbol{f}^C$), random forces($\boldsymbol{f}^R$) and dissipative forces($\boldsymbol{f}^D$). The conservative forces are summation of the bond force($\boldsymbol{f}_{bond}$, the non-bonded force($\boldsymbol{f}_{nb}$), the slip-spring force($\boldsymbol{f}_{ss}$) and the hardcore force($\boldsymbol{f}_{hc}$). The random forces and the dissipative forces on the i_{th} particle, respectively, are defined in the following way:

$$\boldsymbol{f}_i^R = \sigma \sum_{i<j} \omega^R(\mathbf{r}_{ij}) \hat{\mathbf{r}}_{ij} \zeta_{ij} / \sqrt{\delta t} \tag{2.29}$$

$$\boldsymbol{f}_i^D = -\gamma \sum_{i<j} \omega^D(\mathbf{r}_{ij}) (v_{ij} \mathbf{r}_{ij}) \hat{\mathbf{r}}_{ij} \tag{2.30}$$

where ζ_{ij} is a random variable following Gaussian distribution and unit variance and ζ_{ij}=ζ_{ji}. $\mathbf{r}_{ij} = \mathbf{r}_i - \mathbf{r}_j$ and $\mathbf{v}_{ij} = \mathbf{v}_i - \mathbf{v}_j$, and $\hat{\mathbf{r}_{ij}}$ is the unit vector in the direction of $\mathbf{r}_{ij}$. The functions $\omega^R(\mathbf{r}_{ij})$ and $\omega^D(\mathbf{r}_{ij})$ satisfy are given by

$$[\omega^R]^2 = \omega^D = \begin{cases} 1 - |\mathbf{r}_{ij}|/R_{cloud} & |\mathbf{r}_{ij}| \leq R_{cloud} \\ 0 & |\mathbf{r}_{ij}| > R_{cloud} \end{cases} \tag{2.31}$$

where R_{could} is defined in density cloud of the non-boned energy. The σ and γ are related to the temperature by the fluctuation-dissipation theorem: $\sigma = (2\gamma k_B T)^{1/2}$.

Next, a modified velocity verlet algorithm is used to integrate the motion of the polymer beads in the following way:

$$\begin{aligned}
\mathbf{r}_i(t+dt) &= \mathbf{r}_i(t) + \mathbf{v}_i(t)dt + \frac{1}{2}\boldsymbol{f}_i(t)dt^2 \\
\mathbf{v}_i(t+1/2dt) &= \mathbf{v}_i(t) + \frac{1}{2}\boldsymbol{f}_i(t)dt \\
\boldsymbol{f}_i(t+dt) &= \boldsymbol{f}_i(\mathbf{r}_i(t+dt)) \\
\mathbf{v}_i(t+dt) &= \mathbf{v}_i(t+1/2dt) + \frac{1}{2}\boldsymbol{f}_i(t+dt)dt
\end{aligned} \tag{2.32}$$

Results: Linear Rheology of the DPD thermostat. Then we implemented the DPD thermostat to the rouse homopolymer melts and calculate the stress correlation function in Figure 2.21. The stress from $\boldsymbol{f}^R$ and $\boldsymbol{f}^D$ is not added in the Figure 2.21 since we want to compare the stress relaxation function calculated from the DPD thermostat with the theoretical stress relaxation function of the rouse homopolymer. Adding the stress from $\boldsymbol{f}^R$ and $\boldsymbol{f}^D$ will shift the total stress relaxation function upwards, which depends on the magnitude of σ. When $\sigma = 3.0$ and the bond length b is $0.18\mathrm{R}_e$, a fluctuation period $\delta\ \mathrm{t}_{os} = 0.17$ shows up in the beginning of the stress correlation function, which is an artifact. The oscillation originates from the dominant harmonic spring bond energy. The fluctuation period scales linearly with the bond length b, as shown in Figure 2.21b). And the stress correlation function associated with different bond length is plotted in Figure 2.22. We also tested the DPD thermostat with different values of σ and we found that though increasing the magnitude of the random forces($\boldsymbol{f}^R$) and dissipative forces($\boldsymbol{f}^D$) can remove the oscillation, the shape of the stress correlation function still cannot follow the theoretical prediction of the rouse. Therefore, the DPD thermostat introduces artifacts in our model.

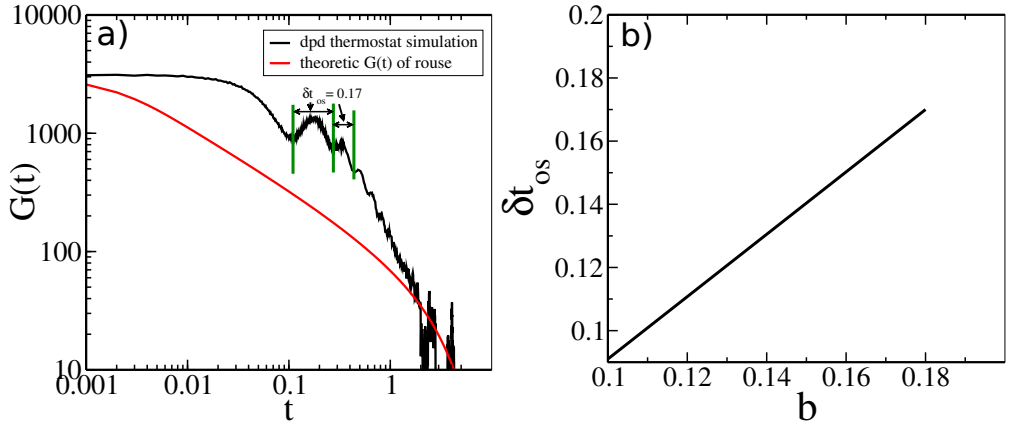

Figure 2.21: a) The stress correlation function of the rouse homopolymer from the DPD thermostat with $\sigma = 3.0$. b) The oscillation period as a function of the bond length b when $\sigma = 3.0$.

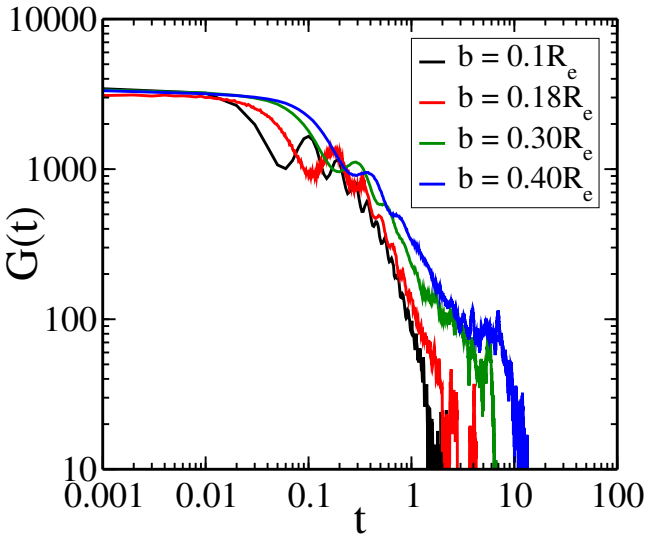

Figure 2.22: The stress correlation function with different the bond lengths when $\sigma = 3.0$.

CHAPTER 3

EVOLUTIONARY PATTERN DESIGN FOR COPOLYMER/HOMOPOLYMER MIXTURES DIRECTED SELF-ASSEMBLY HOLE-SHRINK PROCESS WITH SIMPLIFIED MODEL

3.1 Abstract

The directed self-assembly of copolymers for 'hole-shrink' applications has attracted considerable attention. Most work to date, however, has focused on pure copolymers. In this work, we report on a fast approach that is amenable for layout design involving hole-shrink and related geometries. Specifically, we consider the behavior of copolymer-homopolymer mixtures assembled in cylindrical holes. To do so, the OK model for diblock copolymer and homopolymer mixtures is combined with the CMA-ES, thereby resulting in an efficient algorithm for on-the-fly optimization of key material design variables such as composition and wetting conditions. For completeness, the results of the OK-model predictions are examined by comparing with results of a particle-based Theoretically Informed Coarse-Grained(TICG) model. The calculations presented in this work indicate that pure A-B copolymers or A-B copolymers with B homopolymers are the best combination for the hole-shrink process. When A-B copolymers are mixed with C homopolymers, the resulting blends are inferior for creating perfect hole morphologies, irrespective of surface conditions and hole shape.

3.2 Introduction

As critical dimensions in traditional lithographic fabrication continue to shrink, directed self-assembly(DSA) has received considerable attention as a viable option for lithographic patterning of ultra-small features. Indeed, DSA-based patterning process offers advantages for fabricating dense, periodic arrays of lines or spots in manufacturing settings [59, 60].

The so-called DSA hole-shrink process is of importance for semiconductor device manufacturing. In this process, cylinder-forming polymeric materials are filled into wide holes that are etched using conventional lithographic methods. After annealing, part of the polymeric material is ordered into a small cylinder inside the confining hole. The characteristic dimensions of the inner cylinder are considerably smaller than those of the wide hole. The material in the inner cylinder can be removed selectively, thereby shrinking the original hole by as much as a factor of four [61]. The central question in the hole-shrink process is to identify conditions leading to ideal inner cylinders that span the entire thickness of the confining hole.

Multiple articles have reported that a neutral bottom surface and a minor block preferential side-wall interaction are necessary to produce ideal inner cylinders. [62, 63] For example, Peters *et al.* [62] examined the effect of wetting characteristics on hole-shrink assembly using a particle based TICG model. They confirmed that full cylinders are formed when the attractive interaction between the minor block and the wall is strong and the interaction between the bottom wall and the polymer is weak. They also found that homopolymer addition can improve the assembly process. Yoshimoto *et al.* [63] used a simplified diblock copolymer OK model to describe the hole-shrink process. They also reported that by simply varying the shape of the guiding hole, it is difficult to eliminate morphological defects, and that changing the affinity of the bottom surface from 'attractive' to 'neutral' is more effective. While the effects of the wetting characteristics on the hole-shrink assembly process have been widely studied with different models, it is still not well understood how the composition of the polymer blends, together with the wetting conditions, influence the hole-shrink assembly process.

In this work, we combine the OK model for the polymer blends comprised of copolymers and homopolymers with the CMA-ES to arrive at an on-the-fly optimization approach that is able to identify optimal design variables, such as composition, wetting conditions and polymer chemistry, to form ideal inner cylinders spanning the entire confining hole. We also confirm the optimization results by evaluating the optimized conditions using a more reliable TICG model. Our simulations indicate that A-B copolymer hole-

shrink assembly, the addition of B homopolymer can improve the hole-shrink process. However, the addition of a C homopolymer can lead to defect formation.

3.3 Model and Methods

3.3.1 Ohta-Kawasaki(OK) Model for blends

We consider a system of A-B diblock copolymers and B or C homopolymers. The local volume fractions of these monomers are denoted, respectively, by $\phi_A(\mathbf{r})$, $\phi_B(\mathbf{r})$ and $\phi_{B'}(\mathbf{r})/\phi_C(\mathbf{r})$, where B' corresponds to the B monomers of the homopolymer. Conservation of mass requires that $\phi_A + \phi_B + \phi_{B'}/\phi_C = 1$. Following Ohta *et al.* [3], we use the free energy form developed by Ohta and Kawasaki [64] to characterize the system morphology. This formalism has the advantage of being computationally efficient and straightforward to implement in GPU parallel environments. The total free energy $\mathbf{F}[\psi, \phi]$ in the system is given by the sum of three terms:

$$\mathbf{F}[\psi, \phi] = \mathbf{F_S}[\psi, \phi] + \mathbf{F_L}[\psi, \phi] + \int d\mathbf{r} H_{ext}[\psi, \phi]. \tag{3.1}$$

Here ϕ is the order parameter field quantifying the extent of microphase separation between A monomers and B monomers, defined as the monomer volume fraction difference, $\phi \equiv \phi_A - \phi_B$ in the A-B diblock copolymer and C homopolymer case, and $\phi \equiv \phi_A - \phi_B - \phi_{B'}$ in the A-B diblock copolymer and B homopolymer case. The variable ψ , defined as $\psi \equiv \phi_A + \phi_B$ in both cases, is the order parameter field describing the macrophase separation of the copolymer and the homopolymer. Here ϕ and ψ are independent variables.

The short-range part $\mathbf{F_S}$ corresponds to the usual Ginzburg-Landau(GL) free energy function and is given by

$$\mathbf{F_S}[\psi, \phi] = \int d\mathbf{r}[\frac{1}{2}(\nabla\psi)^2 + \frac{1}{2}(\nabla\phi)^2 + W[\psi, \phi]]. \tag{3.2}$$

The two gradient terms represent the free energy cost associated with spatial inhomo-

geneities in both ψ and ϕ. The $W[\psi, \phi]$ term is the local free energy density that drives the microphase separation between monomer A and monomer B, and the macrophase separation between the copolymer and the homopolymer. The $W[\psi, \phi]$ term can be written as

$$W(\psi, \phi)[\eta, \phi] = g_1(\eta) + g_2(\phi) + b_1\eta\phi - \frac{1}{2}b_2\eta\phi^2 - \frac{1}{2}b_3\eta^2\phi. \tag{3.3}$$

We have introduced a new variable, η as $\eta = \psi - \psi_c$, where ψ_c is the volume fraction at the critical point of the macrophase separation. Since we want to avoid macrophase separation in our system, we set $\psi_c = \bar{\psi}$, where $\bar{\psi}$ is the spatial average value of ψ in the system. The two independent functions $g_1(\eta)$ and $g_2(\phi)$ are assumed to be even functions of the argument. Below the macrophase/microphase separation temperature, $g_1(\eta)$ and $g_2(\phi)$ exhibit a double-well potential. Following Ohta *et al.* [3], the form of the local interactions g_i(x)(i = 1 and 2) is chosen as $g_i(x) = -A_i ln\ cosh(x) + x^2/2$. Parameter A_i controls the degree of phase separation, and $g_i(x)$ exhibits one minimum at x = 0 for $0 < A_i < 1$ and has two minima for $A_i > 1$. The shapes of g_i(x) at A_i = 0.5, 1.0, and 1.3 are shown in Figure 3.1

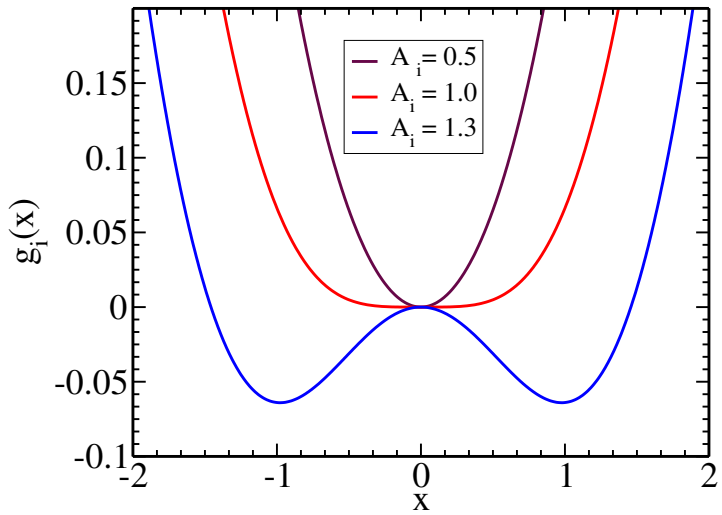

Figure 3.1: Local demixing free energy as a function of order parameter x.

The term with the factor b_1 is associated with the short-range interaction between

monomers. The constant b_1 is given by

$$b_1 = \frac{1}{4}(u_{AA} - u_{BB}) - \frac{1}{2}(u_{AC} - u_{BC}) \tag{3.4}$$

where $u_{ij}(i,j = \text{A , B , C})$ is the interaction strength between i and j monomers and can be written as

$$u_{ij} = \frac{1}{2}\sum_{ij}\int dr\phi_i\phi_j. \tag{3.5}$$

The term with the coefficient b_2 is necessary to ensure that microphase separation occurs only in the copolymer-rich region, because a large absolute value of ϕ is energetically favorable in the region $\eta > 0$. Both b_1 and b_2 are set to be non-negative variables under the evolutionary optimization procedure outlined below.

The other constant, defined as $b_3 = b_0(1/\bar{\phi}_A - 1/\bar{\phi}_B)$, with b_0 a positive value, changes sign under the interchange between A and B in order for the last term to be invariant under the transformations $\eta \rightarrow -\eta$ and $\phi \rightarrow -\phi$. Here $\bar{\phi}_i(i = \text{A , B , B'/C})$ is the spatial average volume fraction of i in the system.

The long-range $\mathbf{F_L}$ term in Equation 3.1 originates from the reduction of conformational entropy of each polymer chain due to chain connectivity. It can be written as [3]

$$\mathbf{F_L}[\psi,\phi] = \int dr \int dr'\mathbf{G}[\mathbf{r},\mathbf{r'}][\frac{\alpha}{2}\delta\phi(\mathbf{r})\delta\phi(\mathbf{r'}) + \frac{\beta}{2}\delta\phi(\mathbf{r})\delta\psi(\mathbf{r'}) + \frac{\gamma}{2}\delta\psi(\mathbf{r})\delta\psi(\mathbf{r'})]. \tag{3.6}$$

Here G[$\mathbf{r}$,$\mathbf{r'}$] satisfies the relation -∇^2G[$\mathbf{r}$,$\mathbf{r'}$]=$\delta(\mathbf{r} - \mathbf{r'})$ and δx($\mathbf{r}$)=x($\mathbf{r}$)-$\bar{x}$(x=ϕ,ψ) with $\bar{x}$ the spatial average of x. For simplicity, we consider $G[\mathbf{r},\mathbf{r'}] = -ln(|\mathbf{r} - \mathbf{r'}|)/2\pi$ here.[64] The constants α, β, and γ are given, respectively, by

$$\alpha = a[\frac{1}{\phi_A} + \frac{1}{\phi_B}]^2 \tag{3.7}$$

$$\beta = a[\frac{1}{\phi_A^2} - \frac{1}{\phi_B^2}] \tag{3.8}$$

$$\gamma = a[\frac{1}{\phi_A^2} - \frac{1}{\phi_B^2}] \tag{3.9}$$

where a is a positive constant. Following the original model by Ohta [3], we set α to be the typical value of 0.02 and adjust the β and γ according to the above equations in our simulation.

The third term $\int d\mathbf{r} H_{ext}[\psi, \phi]$ describes the interaction between the surfaces (side-wall and bottom surfaces) and the polymers, which is similiar to the surface energy defined by Yoshimoto *et al.* [63]. The surface energy term is given by

$$\begin{aligned}\int d\mathbf{r} H_{ext}[\psi, \phi] = & \int d\mathbf{r} \lambda_{w-\phi}[\phi(\mathbf{r}) - \phi_w]^2 exp(-\mathbf{z}^2/\sigma_s^2) \\ & + \int d\mathbf{r} \lambda_{w-\psi}[\psi(\mathbf{r}) - \psi_w]^2 exp(-\mathbf{z}^2/\sigma_s^2) \\ & + \int d\mathbf{r} \lambda_{b-\phi}[\phi(\mathbf{r}) - \phi_b]^2 exp(-\mathbf{z}^2/\sigma_s^2) \\ & + \int d\mathbf{r} \lambda_{b-\psi}[\psi(\mathbf{r}) - \psi_b]^2 exp(-\mathbf{z}^2/\sigma_s^2).\end{aligned} \tag{3.10}$$

Here, ϕ_w, ψ_w, ϕ_b and ψ_b are parameters controlling the values of ϕ and ψ in the vicinity of the side wall and bottom, with w representing wall and b representing bottom, respectively. $\phi_{w/b}$ can be positive or negative. A positive $\phi_{w/b}$ means that the wall/bottom surface is attractive to the A block as ϕ is defined as ϕ_A - ϕ_B. $\psi_{w/b}$ is restricted to be a positive value as ϕ_A + ϕ_B is non-negative. The coefficients $\lambda_{w-\phi}$, $\lambda_{w-\psi}$, $\lambda_{b-\phi}$ and $\lambda_{b-\psi}$, which are all positive, controls the strength of the wall/bottom affinity. $\mathbf{z}$ is the closest distance to the surface and σ_s is the decaying length in the direction of the closest distance. We set $\sigma_s = 1$ in our simulation and the cut of radius for the exponential decaying function to be $2\sigma_s$.

To identify the equilibrium morphology, we use the Cahn-Hilliard equation where ϕ and ψ evolve simultaneously, as is appropriate for conserved order parameters. The

Cahn-Hilliard equations can be written in the form:

$$\frac{\partial \psi}{\partial\, t} = L_1 \nabla^2 \frac{\partial\, F}{\partial \psi} \tag{3.11}$$

$$\frac{\partial \phi}{\partial\, t} = L_2 \nabla^2 \frac{\partial\, F}{\partial \phi}. \tag{3.12}$$

After substituting the free energy expression in the Cahn-Hilliard equation, we get

$$\begin{aligned}\frac{\partial \psi}{\partial\, t} = L_1\{\nabla^2[-\nabla^2\psi - A_1 tanh(\eta) + \eta + b_1\phi - \frac{1}{2}b_2\phi^2 - b_3\eta\phi \\ + \lambda_{w-\psi}[\psi - \psi_w]exp(-\mathbf{z}^2/\sigma_s^2) + \lambda_{b-\psi}[\psi - \psi_b]exp(-\mathbf{z}^2/\sigma_s^2)] - \gamma\delta\psi - \beta\delta\phi\}\end{aligned} \tag{3.13}$$

$$\begin{aligned}\frac{\partial \phi}{\partial\, t} = L_2\{\nabla^2[-\nabla^2\phi - A_2 tanh(\phi) + \phi + b_1\eta - b_2\eta\phi - \frac{1}{2}b_3\eta^2 \\ + \lambda_{w-\phi}[\phi - \phi_w]exp(-\mathbf{z}^2/\sigma_s^2) + \lambda_{b-\phi}[\phi - \phi_b]exp(-\mathbf{z}^2/\sigma_s^2)] - \alpha\delta\phi - \beta\delta\psi\}\end{aligned} \tag{3.14}$$

where ϕ and ψ are short for $\phi(\mathbf{r}, t)$ and $\psi(\mathbf{r}, t)$, respectively. The transport coefficients L_1 and L_2 are positive. The relative magnitude of these coefficients is not known *apriori*. Here, for simplicity, we set them both to unity.

3.3.2 Theoretically Informed Coarse-Grained(TICG) Model

The Theoretically Informed Coarse-Grained(TICG) model is a reliable particle based approach to describe polymer melts with a volume V at temperature T. We verify the equilibrium morphology predicted by the OK model with the TICG model. Details about the TICG model can be found in Detcheverry *et al.* [2]

Briefly, in the TICG approach, the chain connectivity for the jth chain is given by a harmonic bond potential $\mathcal{H}_{bond}[\{\mathbf{r}_j(s)\}]$:

$$\frac{\mathcal{H}_{bond}[\{\mathbf{r}_j(s)\}]}{k_B T} = \frac{3}{2}\sum_{s=1}^{N_j=1}\frac{[\mathbf{r}_j(s+1) - \mathbf{r}_j(s)]^2}{b^2} \tag{3.15}$$

where $\{\mathbf{r}_j(s)\}$ means the set of coordinates of the coarse-grained beads, k_B is the Boltzmann constant, and b = 0.179 is the mean-square bond length. The mean-square end-to-end distance for the j^{th} chain is $Re_j = b\sqrt{N_j - 1}$.

The non-bonded potential $\mathcal{H}_{nb}$ incorporates both the chemical distinction between unlike monomers and the finite compressibility of the melts. The form of the the non-bonded potential $\mathcal{H}_{nb}$ for A-B copolymer and C homopolymer is given by

$$\frac{\mathcal{H}_{nb}[\{\phi_A, \phi_B\, \phi_C\}]}{k_B T} = \rho_0 \int_V d\mathbf{r}[\chi_{AB}\phi_A\phi_B + \chi_{AC}\phi_A\phi_C + \chi_{BC}\phi_B\phi_C + \frac{\kappa}{2}(1-\phi_A-\phi_B-\phi_C)^2] \tag{3.16}$$

where ρ_0 is the average bulk number density of beads for the polymer blends. Here $\chi_{\alpha\beta}$ is the Flory-Huggins parameter between monomer α and monomer $\beta(\alpha,\beta \in$ A,B,C), which characterizes the incompatibility between unlike beads. The compressibility is quantified by the κ term, which restricts fluctuations of the local densities away from the average value. The local densities ϕ_A, ϕ_B, ϕ_C are estimated based on the 'particle-to-mesh'(PM) technique. Details about their calculation can be found in Detcheverry *et al.* [2]

The interaction between the i^{th} polymer bead and the wall surface is denoted by $U_w(\mathbf{r}_i)$. The interaction between the i^{th} polymer bead and the bottom surface is denoted by $U_b(\mathbf{r}_i)$. The expressions for $U_w(\mathbf{r}_i)$ and $U_b(\mathbf{r}_i)$ are given by

$$\frac{U_w[\{\mathbf{r}_i(s)\}]}{k_B T} = \sum_{bead\ i} \frac{\Lambda_w^{x_i}}{2d_s} exp[-\frac{\mathbf{z}_i^2}{d_s^2}] \tag{3.17}$$

$$\frac{U_b[\{\mathbf{r}_i(s)\}]}{k_B T} = \sum_{bead\ i} \frac{\Lambda_b^{x_i}}{2d_s} exp[-\frac{\mathbf{z}_i^2}{d_s^2}] \tag{3.18}$$

where $\mathbf{z}_i$ is the closest distance from the i^{th} bead to the wall/bottom surface. In the direction of the closest distance, the exponential potentials decay over a distance d_s. $\Lambda_w^{x_i}$ controls the interaction strength between the i^{th} bead and the wall surface, where $x_i \in$ {A,B,C} is the type of the i^{th} polymer bead. Similarly, $\Lambda_b^{x_i}$ controls the interaction strength between the i^{th} bead and the bottom surface.

The overall Hamiltonian is given by the summation of all terms:

$$\mathcal{H} = \sum_{chain\ j} \mathcal{H}_{bond}[\{\mathbf{r}_j(s)\}] + \mathcal{H}_{nb}[\{\phi_A, \phi_B\, \phi_C\}] + U_w[\{\mathbf{r}_i(s)\}] + U_b[\{\mathbf{r}_i(s)\}]. \quad (3.19)$$

We use the MC method described in Detcheverry *et al.* [2] to sample configurations in order to identify the equilibrium morphology of the blends during the hole-shrink process.

3.3.3 CMA-ES Optimization

Let $\hat{\phi}(\mathbf{r})$ be the ϕ order parameter in the target morphology. Then $\phi_{eq}(\mathbf{r})$ is the order parameter in the equilibrium morphology for a specific set of parameters. The objective function is quantified by the average squared difference between $\phi_{eq}(\mathbf{r})$ and $\hat{\phi}(\mathbf{r})$ per cell

$$\Omega \equiv \frac{1}{V} \int d\mathbf{r} \{\phi_{eq}(\mathbf{r}) - \hat{\phi}(\mathbf{r})\}^2. \quad (3.20)$$

where V is the number of cells or the volume inside the cylinder. Our goal is to minimize this function by optimizing the parameters.

To do so, we resort to the CMA-ES. The CMA-ES has achieved tremendous success as an optimization tool in the context of swimming fish simulation [65], crystal structure predictions [66], combustion control [67] and the DSA of block copolymers for design-oriented structures [68, 69]. Since the CMA-ES algorithm does not require the calculation of gradients inside the black-box, the search costs of the algorithm are just the number of black-box calls. The CMA-ES algorithm evolves in the following way. At each generation, a finite number(λ) of offspring derived from the previous generation is evaluated with a black-box function. Then, those offspring are sorted according to the objective function. The 'best' μ offspring are used to mutate and recombine to create offspring for the next generations.

Our implementation of the CMA-ES method is based on the state-of-art algorithm discussed in Ref [70]. In our problems, the population size λ and the number of surviving offspring μ are 28 and 4, respectively. They are chosen based on heuristic arguments in

Ref [70].

3.3.4 Simulation Methods

The target morphology of $\phi(\mathbf{r})$ is generated with $\hat{\phi}(\mathbf{r}) = 1.0$ in the A rich region and $\hat{\phi}(\mathbf{r}) = -1.0$ in the B rich region. The transition region has $\hat{\phi}(\mathbf{r}) = -0.5$, $\hat{\phi}(\mathbf{r}) = 0.5$ and $\hat{\phi}(\mathbf{r}) = 0.0$, depending on how wide we want the transition region to be. There are three parameters that characterize the dimensions of the double hole: R, L and H. A single hole represents a degenerate case of the double hole, where L is 0. Figure 3.2 gives an example of the double hole target, where R = L_0, L = L_0 and H = 1.33L_0, where L_0 is the natural periodicity of the block copolymer and the value of L_0 is 15 in our system. We set L and R to be multiples of L_0 because Peters *et al.* [62] predicted that the confined single hole with critical dimensions multiples of L_0 gives the largest window for generating perforated holes in the single hole-shrink process.

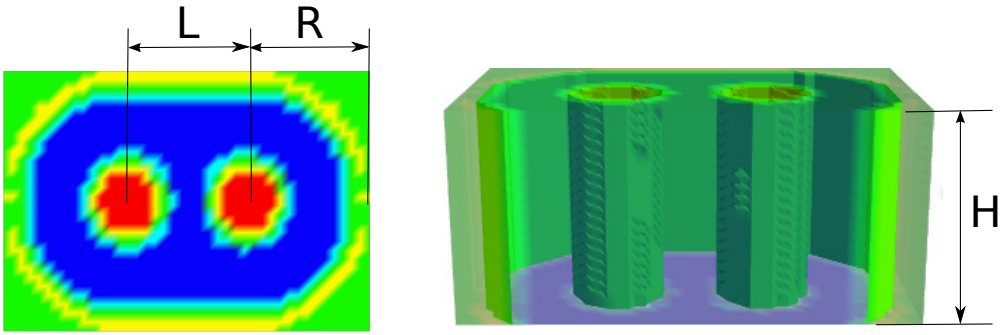

Figure 3.2: Target morphology characterized by parameters R = L_0, L = L_0 and H = 1.33L_0.

The simulation is run with parameters generated by the CMA-ES algorithm. The parameters to be optimized in this work are the composition of the polymers($\phi_A, \phi_B, \phi'_B/\phi_C$), the strength of wall interactions with the polymer($\lambda_{w-\phi}, \lambda_{w-\psi}, \lambda_{b-\phi}, \lambda_{b-\psi}$), and the polymer chemical characteristics(A_1, A_2, b_1, b_2, b_0). After the simulation reaches equilibrium, the order parameter $\Omega = \frac{1}{V}\int d\mathbf{r}\{\phi_{eq}(\mathbf{r}) - \hat{\phi}(\mathbf{r})\}^2$ characterizing the average squared difference between the current morphology and the target morphology per cell is calculated.

If the order parameter Ω of this generation is converged, the simulation should stop with the solution. Otherwise, the simulation generates the next generation children using CMA-ES algorithm and continue evaluating the equilibrium morphology again.

Solving the Cahn-Hilliard equation We discretized the simulation box into an N×N×N grid to solve the CH equations. The gradient terms in Equations 3.13 and 4.5 are estimated using a central-difference method. We propagate the composition field $\phi(\mathbf{r}, t)$ using the forward Euler's method, with δt as the time step difference. (The mobility factor L_1 and L_2 can be absorbed into the term of δt). The time complexity of this algorithm scales with O(N^3), where N^3 is the number of grid points in the system.

Boundary Conditions

For cells in the middle region of the domain of interest, we use the central difference method to calculate the gradient operator and the Laplace operator without any special techniques. For cells at a boundary, the gradient operator and Laplace operator of the cells have to be 0 to ensure conservation of mass. In our implementation, the values of $\phi(\mathbf{r})$ or $\psi(\mathbf{r})$ in cells outside the simulation boundary does not have a fixed value and is automatically set to be the same as the value of $\phi(\mathbf{r})$ or $\psi(\mathbf{r})$ in the cell which we are evaluating. However, there are still flux of $\phi(\mathbf{r})$ and $\psi(\mathbf{r})$ on the surface of cylinder because of the long range $F_{\mathbf{L}}$ term. Therefore, after each iteration time step, the $\phi(\mathbf{r})$ and $\psi(\mathbf{r})$ which leave the cylinder boundary, should be added back to the original cells on the cylinder boundary. In this way, the mass is conserved.

Simulation time and time step

To determine necessary simulation time required to reach an equilibrium morphology when evolving the CH equations, we compare results along a simulation trajectory at different time points. Since the double hole simulation box has more cells than the single hole, we use the double hole as the test system. In Figure 3.3 we plot the hole-shrink morphology evolution at different time points and in Figure 3.4 we plotted the profile of ϕ in the x and y directions at different time points. As shown in Figure 3.3, where we use a time step δt=0.01, after t = 100 or time steps = 10000 the equilibrium morphology has been found. Here, the time step δt = 0.01 is a good enough time step. With a

fixed simulation time t, any time step less than 0.01 generates the same equilibrium morphology. For robustness, we use t = 600 in our simulations.

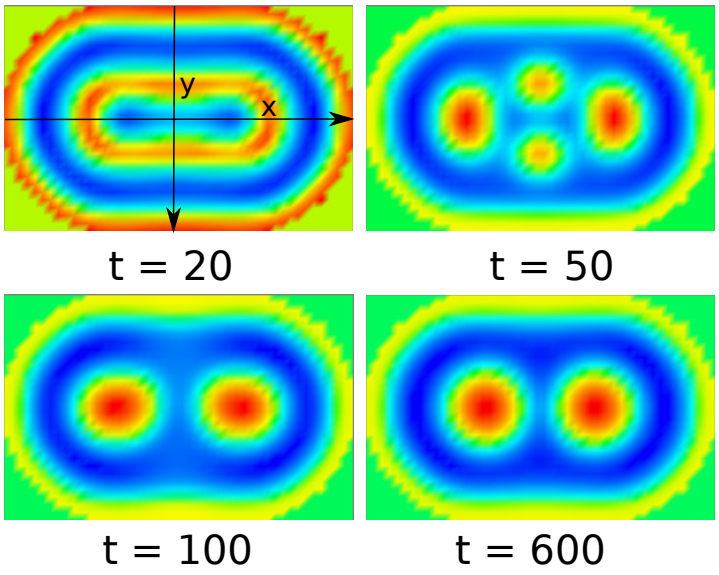

Figure 3.3: Time dependence of the morphology evolution. Morphology at different time using δt = 0.01. Parameters:R = L_0, L = L_0, H = 1.33L_0, α = 0.02, A_1 =0.0, A_2 = 2.1, $\bar{\phi}_A = 0.3$, $\bar{\phi}_B = 0.7$

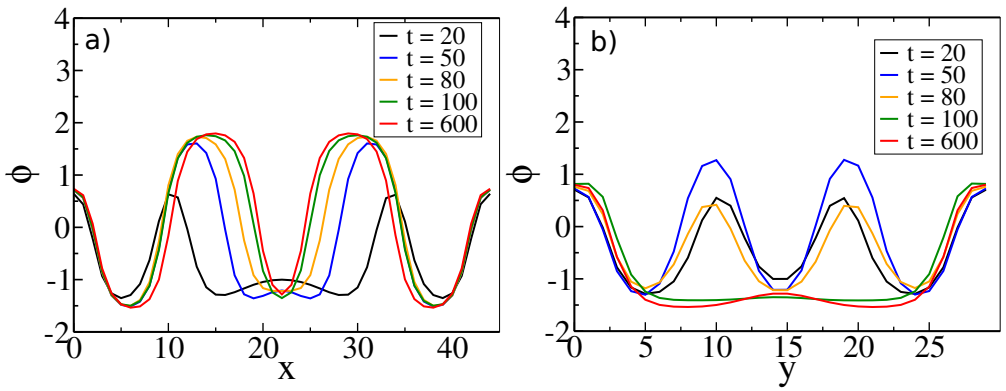

Figure 3.4: a)The profile of ϕ in the x axis direction at different time points. b)The profile of ϕ in the y axis direction at different time points. The x axis and y axis are noted in Figure 3.3.

3.4 Simulation Results

3.4.1 Single Hole-Shrink Process

In Figure 3.5, we consider the pure block copolymer hole-shrink process in two conditions: a neutral bottom surface(a and b) and an attractive bottom surface(c and d). The compositions of the block copolymer are $\bar{\phi}_A = 0.33$ and $\bar{\phi}_B = 0.67$. The chemical characteristics of the pure block copolymer are $A_1 = 0$, $A_2 = 1.5$, and $b_1 = b_2 = b_0 = 0$. In both cases, the side wall is attractive to the A block with $\lambda_{w-\phi} = 1.5$. As reported in the literature, a perfect hole-shrink morphology appears for the neutral bottom surface condition, while an attractive bottom surface leads to a residual B block layer near the bottom of the hole.

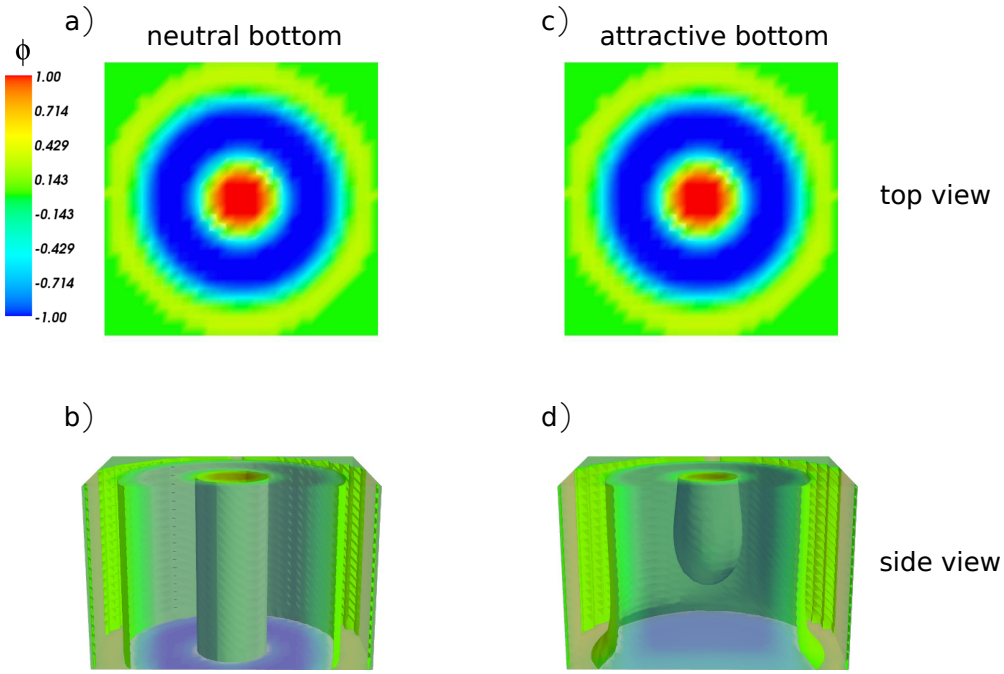

Figure 3.5: The side-wall surfaces in the four figures are the same and are attractive to the A block, where A is the minority block and $\phi = \phi_A - \phi_B$. a) & b) show the top view and the side view of the neutral bottom surface hole-shrink process, respectively. Parameters: $\bar{\phi}_A = 0.33$, $\bar{\phi}_B = 0.67$,$A_1 = 0$, $A_2 = 1.5$,$b_1 = b_2 = b_0 = 0$, $\lambda_{w-\phi} = 1.5$ and $\lambda_{b-\phi} = 0.0$. c) & d) show the top view and the side view of the A block attractive bottom surface hole-shrink process, respectively. Parameters: $\bar{\phi}_A = 0.33$, $\bar{\phi}_B = 0.67$,$A_1 = 0$, $A_2 = 1.5$,$b_1 = b_2 = b_0 = 0$, $\lambda_{w-\phi} = 1.5$ and $\lambda_{b-\phi} = 1.5$.

3.4.2 The Interfacial Energies in the OK Model

It is not easy to directly map the surface potentials in the OK model to real units since the molecular weight and chain length are not specified in the OK model. The coefficients ϕ_w, ψ_w, ϕ_b and ψ_b control which component wets the surfaces, while the coefficients $\lambda_{w-\phi}$, $\lambda_{w-\psi}$, $\lambda_{b-\phi}$ and $\lambda_{b-\psi}$ control the relative strength of the interfacial energies. In order to understand those surface potentials in real units, we used the TICG model as a calibration tool. When the TICG model and the OK model produce the same morphology while having the correctly matched other parameters, we have an understanding of the OK-model coefficients in real units by comparing to the interfacial parameters in the

TICG model. The $\Lambda_w^A N$ = -2.0 employed in the TICG model corresponds to a surface energy differences in the vicinity of 0.02 $k_B T/nm^2$ according to Umang Nagpal *et al.* [71].

3.4.3 Single hole-shrink process optimization

We use the artificial 'bitmap' morphology as the target for evolutionary optimization of ϕ. The 'bitmap' morphology has a value of $\hat{\phi}(\mathbf{r})$ =1 in the A-rich region and $\hat{\phi}(\mathbf{r})$ =-1 in the B-rich region. The interface has $\hat{\phi}(\mathbf{r}) = 0.5$ and -0.5 in the transition region. The natural periodicity of the 'bitmap' target morphology should be similar to the natural periodicity of the real morphology. With the CMA-ES method, we can successfully determine a near-optimal condition (components and surface chemistry) to generate the desired morphology.

For simplicity, we first use a 'bitmap' target, which is similar to the morphology in Figure 3.5 a)&b), to study the evolutionary process of the pure A-B block copolymer in the single hole shrink. The pure block copolymer represents a degenerate case of the mixtures; if the mixtures cannot find better optimization results, they will converge to the pure copolymer during the CMA-ES process. If the mixtures exhibit better performance, there will be an optimal solution for mixtures. In the case of the pure copolymer, the ψ in the OK model is constrained to be 1.0 everywhere in the hole. The diameter of the single hole is set to be $2L_0 = 30$ because the natural periodicity of the pure copolymer in Figure 3.5a)&b) is $L_0 = 15$. The height of the single hole is set to be $1.33L_0 = 20$, which can be changed without affecting the condition of the hole-shrink cylinder.

As expected, the best composition of the A block is found to be 32.25%, which is in agreement with literature [63]. As $\phi_w = 0.427$ is a positive value and $\lambda_{w-\phi}$ is nontrivial, the wall surface is attractive to the A block. The bottom surface is neutral since $\lambda_{w-\phi}$ reduces to almost zero even though ϕ_b is a positive number. The lowest residual value of the objective function is 0.01631. Since the actual $\phi(\mathbf{r})$ in a certain cell can be -1 and the $\hat{\phi}(\mathbf{r})$ can be 1, the maximum value of the objective function can be 4 in the worst case. Therefore, the lowest average squared difference between $\phi(\mathbf{r})$ and $\hat{\phi}(\mathbf{r})$ in Figure 3.6 is only 0.4% of the maximum residual value of the objective function. The residual value of

the Ω describes how close the pure block copolymer morphology is to the target 'bitmap' morphology on average, with $\Omega = 0.0$ meaning that the ϕ in every cell of the equilibrium morphology is exactly the same as the target morphology, which is unachievable in the real hole-shrink process.

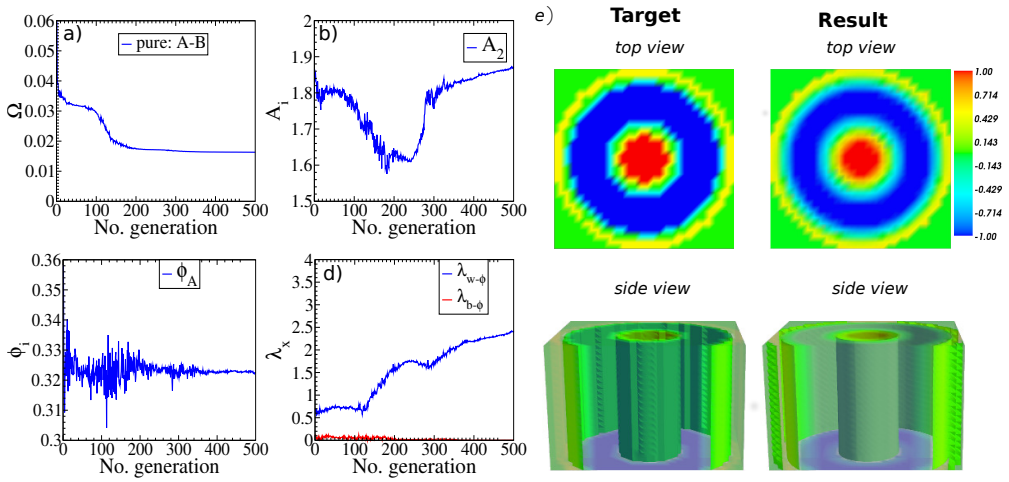

Figure 3.6: Pure A-B copolymer in the single hole-shrink CMA-ES process. a) Evolution of the objective function. c) Evolution of the chemical incompatibility parameter: A_2. b) Evolution of the components volume fraction. d) Evolution of the wall and bottom surface energy. e) Top and side views of the 'bitmap' target morphology and the morphology generated at the end of the CMA-ES process.

$\bar{\phi}_A$	$\bar{\phi}_B$	A_2	$\lambda_{w-\phi}$	ϕ_w	$\lambda_{b-\phi}$	ϕ_b
0.3225	0.6775	1.87	2.42	0.427	0.00147	0.2225

Table 3.1: Evolutionary results of the A-B pure block copolymer in the single hole-shrink CMA-ES process.

Having established the CMA-ES optimization process for the pure block copolymer in the single hole, we can optimize block copolymer mixtures and compare the optimized results with those in the case of pure block copolymers. Figure 3.7 shows results for mixtures of A-B copolymer and B homopolymer. The B monomers in the B homopolymer are denoted as B', to differentiate them from the B monomers in the A-B diblock

copolymer. We assume that the B homopolymers are well mixed with the A-B diblock copolymers, and therefore A_1 is fixed to 0 and there is no macrophase separation. The optimized volume fraction of the A monomers is 32.7%, which is very close to the result in Figure 3.6 and Table 3.1. The optimized wall surface energy remains attractive to the minority block. The fact that ψ_w is much larger than 1.0 and $\lambda_{w-\psi}$ is large means that the wall surface is dominated by the A-B block copolymer. The bottom surface still remains neutral as $\lambda_{b-\phi}$ is trivial. The bottom surface is also non-preferential to A-B block copolymer and B homopolymer as $\lambda_{b-\psi}$ is almost zero. The lowest residual value of the objective function in the A-B/B' mixtures is 0.0153, which even lower than the lowest residual value of the objective function in the pure block copolymer CMA-ES process. It means that the mixtures of A-B block copolymer and B homopolymer also can form the hole-shrink morphology close to the target morphology with the optimized parameters in Table 3.2. Furthermore, in Figure 3.6c), the composition of the A-B/B' has tried to converge to the pure copolymer condition. But the CMA-ES algorithm helps the optimization process escape the local minimum and the compositions converges back to A-B mixtures. Therefore, the A-B/B' mixtures system in Table 3.2 is even more competitive than the pure A-B block copolymer condition in forming the target hole-shrink morphology.

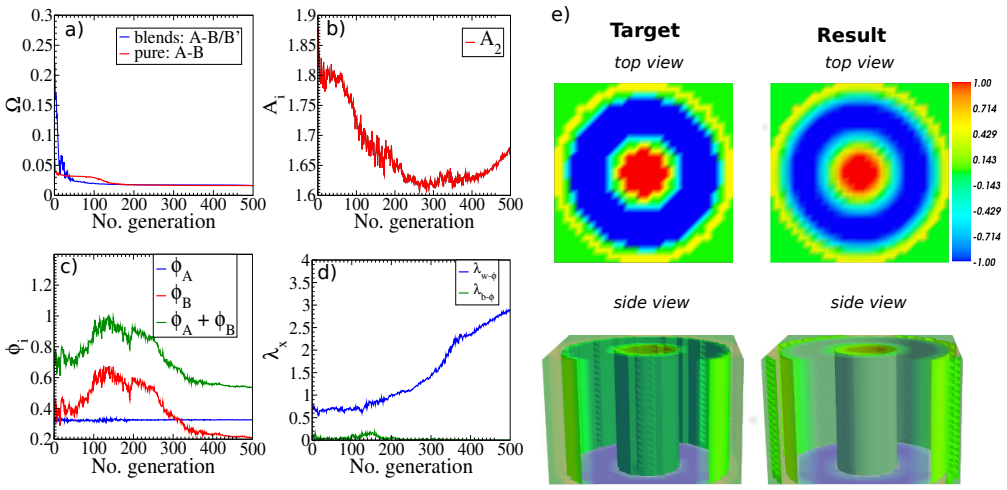

Figure 3.7: A-B copolymer/B homopolymer mixtures(A-B/B' mixtures) in the single hole-shrink CMA-ES process. a) Evolution of the objective function. b) Evolution of the components volume fraction(B' represents the B homopolymer in contrast to the B block in copolymer). c) Evolution of A_1 and A_2. d) Evolution of the wall and bottom surface energy. e) top and side views of the 'bitmap' target morphology and the morphology generated at the end of the CMA-ES process.

$\bar{\phi}_A$	$\bar{\phi}_B$	$\bar{\phi}'_B$	A_2	$\lambda_{w-\phi}$	$\lambda_{w-\psi}$	ϕ_w	ψ_w	$\lambda_{b-\phi}$	$\lambda_{b-\psi}$	ϕ_b	ψ_b
0.327	0.208	0.465	1.68	2.9	2.0	1.12	6.2	0.0016	0.0013	-0.76	0.52

Table 3.2: Evolutionary results of A-B/B' mixtures in the single hole-shrink CMA-ES process.

In order to determine the reliability of our results using the OK model, we also use the Theoretical Informed Coarse Grained(TICG) model for the optimal solutions of the A-B copolymer and B homopolymer CMA-ES process. There is no one-to-one mapping function to transfer the reduced parameters in the OK model to the detailed parameters in the TICG model, since one set of parameters in the OK model can correspond to multiple sets of parameters in the TICG model. And no formula has been determined to transfer the value of A_1 and A_2 to Flory Huggins parameter in the TICG model. Therefore, we use the trial-and-error method to get the parameters in the TICG model that produce a

similar equilibrium morphology as that observed in the OK model optimization. There are some restrictions that we should follow in order to make the parameters in the TICG model consistent with the parameters in the OK model. Those restrictions are the following: the Flory-Huggins parameters between monomers B in copolymer and homopolymer should be 0: $\chi_{BB'}$=0, the Flory-Huggins parameters χ_{AB} and $\chi_{AB'}$ should the same, and both should be above the order-disorder transition temperature(ODT), the volume fraction of the homopolymer should be $\bar{\phi}_{B'} = 0.465$, and the relationship between the volume fraction and chain discretization should follow the following formula: $\bar{\phi}_A/(\bar{\phi}_A + \bar{\phi}_B) = N_A/(\mathrm{N}_A + \mathrm{N}_B)$, $\bar{\phi}_B/(\bar{\phi}_A+\bar{\phi}_B) = N_B/(\mathrm{N}_A + \mathrm{N}_B)$ and $\bar{\phi}_A/\bar{\phi}_B = \mathrm{N}_A/\mathrm{N}_B = 0.327/0.208 \approx 1.572$. The side wall should be attractive to the minority block and the bottom wall should be neutral. Through trial and error, we vary the parameters, including radius of the cylinder, and found a set of parameters which satisfies the parameter restrictions in the OK model and generate a similar morphology to that in the OK model, as shown in Table 3.3. In the TICG model, we found that in the A-B/B' mixtures, B homopolymers with short chains is better than B homopolymer with long chains at forming perfect hole shrink morphology with the same volume fraction of $\bar{\phi}_{B'}$. Therefore, we use $\mathrm{N}_{B'} = 4$ for the homopolymer and $\mathrm{N}_{A-B} = 32$ for the diblock copolymer in the TICG model. However, this degree of freedom is lost in the OK model since the OK model does not specify the chains length directly. The morphology generated in the TICG simulation with those parameters in Table 3.3 is shown in Figure 3.8. The pink, green and purple beads represent the A,B and B' polymer beads, respectively.

χ_{AB}	κ	N_A	N_B	$N_{B'}$	$\bar{\phi}_{B'}$	Λ_w^A	Λ_w^B	Λ_b^A	Λ_b^B	H	R	L	$\sqrt{\bar{N}}$
1.15625	1.5625	20	12	4	0.465	-2.0	0.0	0.0	0.0	$2.0\mathrm{R}_e$	$2.0\mathrm{R}_e$	0	96

Table 3.3: Parameters for generating the perfect single hole shrink morphology in the TICG model with A-B/B' mixtures.

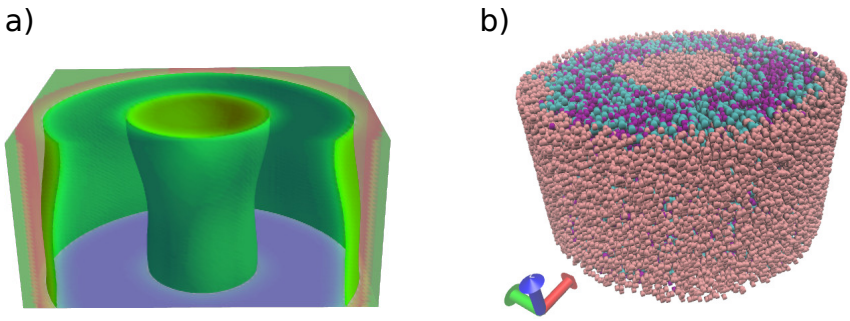

Figure 3.8: Single hole-shrink morphology generated by the TICG model using CMA-ES optimized volume fractions and surfaces energies for A-B/B' mixtures. a)The color map of the quantity: $(\phi_A\text{-}\phi_B)/(\phi_A+\phi_B)$. b) The polymer bead representation generated by the Visual Molecular Dynamics(vmd) software.

We now turn our attention to the A-B block copolymer and C homopolymer mixtures. By substituting the definition $\phi \equiv \phi_A - \phi_B - \phi_{B'}$ with $\phi \equiv \phi_A - \phi_B$, we can use the Cahn-Hilliard Equations to find the equilibrium morphology for A-B/C blends. We use the same CMA-ES process to identify the optimal parameters in Figure 3.9 and Table 3.4. It is found that the C homopolymer volume fraction ϕ_C is automatically reduced to zero and A_1 also reduces to zero, which means there is no macrophase separation in the system. Because the C homopolymer is gone, the bottom and the wall surface are dominated with diblock copolymers, which is consistent with the result $\psi_w > 1.0$ and $\psi_b > 1.0$ in Table 3.4. By comparing Table 3.1 and Table 3.4, we find that the optimization parameters, such as ϕ_A, A_2, $\lambda_{w-\phi}$ and ϕ_w, for A-B/C mixtures is close to those for the pure A-B diblock copolymer. The average residual value of the objective function in degenerate A-B/C mixtures is 0.01635, which is approximately the same as that in the pure copolymer. Therefore, the optimal result of A-B copolymer/C homopolymer mixtures degenerates to the case of pure A-B copolymer.

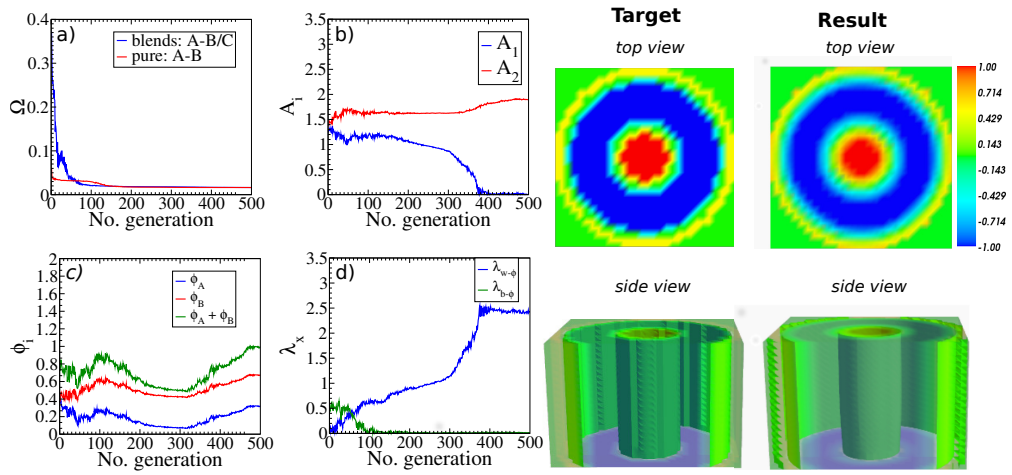

Figure 3.9: A-B copolymer/C homopolymer mixtures(A-B/C mixtures) in the single hole-shrink CMA-ES process. a) Evolution of the objective function. b) Evolution of the components volume fraction. c) Evolution of A_1 and A_2. d) Evolution of the wall and bottom surface energy. e) top and side views of the 'bitmap' target morphology and the morphology generated at the end of the CMA-ES process.

$\bar{\phi}_A$	$\bar{\phi}_B$	$\bar{\phi}_C$	A_1	A_2	$\lambda_{w-\phi}$	$\lambda_{w-\psi}$	ϕ_w	ψ_w	$\lambda_{b-\phi}$	$\lambda_{b-\psi}$	ϕ_b	ψ_b
0.317	0.673	0.01	0.005	1.90	2.4	3.35	0.40	3.77	0.014	0.206	1.22	1.16

Table 3.4: Evolutionary results of A-B/C mixtures in the single hole-shrink CMA-ES process.

As before, we reproduce the single hole-shrink morphology in the TICG model using the same volume fractions as in Figure 3.10. Through trial and error under the following restrictions:$\bar{\phi}_A = N_A/(N_A + N_B) \approx 0.317$, $\bar{\phi}_C = 0.0$ and the χ_{AB} should be above the ODT, we find one set of parameters which can generate full cylinder morphology in the single hole, as shown in Table 3.5. The morphology generated using parameters in Table 3.5 is shown in Figure 3.10, which shows a perfect single hole shrink.

χAB	κ	N_A	N_B	ϕ_C	Λ_w^A	Λ_w^B	Λ_b^A	Λ_b^B	H	R	L	$\sqrt{\bar{N}}$
1.15625	1.5625	11	23	0	-2.0	0.0	0.0	0.0	2.55R_e	1.91R_e	0	96

Table 3.5: Parameters for generating the perfect single hole shrink morphology in the TICG model with the A-B copolymer.

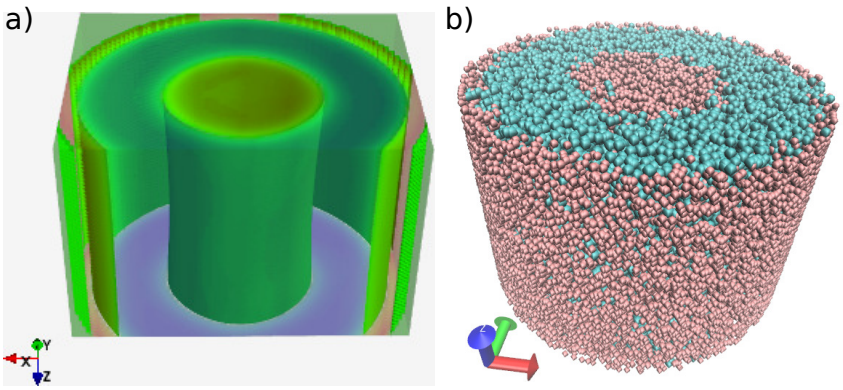

Figure 3.10: Single hole-shrink morphology generated by the TICG model using CMA-ES optimized volume fractions and surface energies for the A-B copolymer. a) The color map of the quantity:$(\phi_A$-$\phi_B)/(\phi_A$+$\phi_B)$. b) The VMD representation of the polymer beads in the TICG model, with the pink bead representing the A bead and the green bead representing the B bead.

3.4.4 Double/multiple hole-shrink process optimization

In what follows, we apply similar techniques to examine the double hole-shrink process. Like the single hole-shrink case, we first consider a pure block copolymer. We then compare the residual value of the objective function in the pure block copolymer with the residual value of the objective function for blends to understand the performance of mixtures in the double hole-shrink process. The simulation box in the double hole shrink is set up with parameters: R = L_0 , L = L_0 and H = 1.33L_0.

The result of the CMA-ES process with pure copolymer in the double hole shrink is shown in Figure 3.11, where the lowest residual value of the objective function is 0.0161. Similar to the single hole-shrink process, the lowest average squared difference

between $\phi(\mathbf{r})$ and $\hat{\phi}(\mathbf{r})$ per cell in the pure block copolymer is the benchmark to compare the performance of the blends with the pure block copolymer. The optimized volume fraction of the A monomers shifts to 32.85% in the double hole-shrink process, which is similar to 32.2% in the single hole-shrink process. As expected, the side wall remains attractive to the minority block and the bottom surface remains neutral.

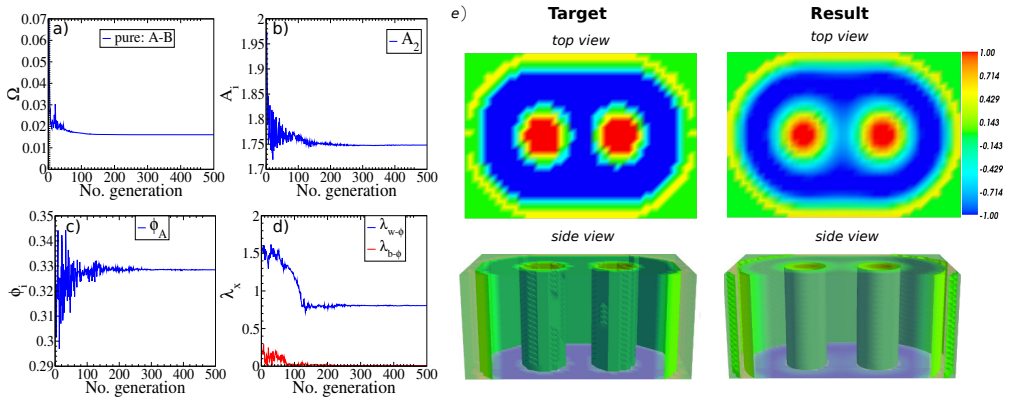

Figure 3.11: Pure A-B copolymer in the double hole-shrink CMA-ES process. a) Evolution of the objective function. b) Evolution of the components volume fraction. c) Evolution of A_2. d) Evolution of the wall and bottom surface energy. e) top and side views of the 'bitmap' target morphology and the morphology generated at the end of the CMA-ES process.

$\bar{\phi}_A$	$\bar{\phi}_B$	A_2	$\lambda_{w-\phi}$	ϕ_w	$\lambda_{b-\phi}$	ϕ_b
0.3285	0.6715	1.75	0.8	0.25	0.00096	-0.29

Table 3.6: Evolutionary results of the pure A-B copolymer in the double hole-shrink CMA-ES process.

Figure 3.12 shows the CMA-ES evolutionary results for A-B/B mixtures in the double hole. The lowest residual value of the objective function in Figure 3.12 is 0.0159, which is lower than that for the pure A-B copolymer. Therefore, a certain volume fraction of B homopolymer has a positive effect on the hole-shrink process with A-B/B' mixtures. Table 3.7 shows that the A monomers correspond to 32.9% and the B monomers correspond to 15.8% of the total composition; the B' monomers in the homopolymer take

up the remaining 51.3% in the final optimization formulation. The wall surface is still attractive to the minority block and the bottom surface is neutral.

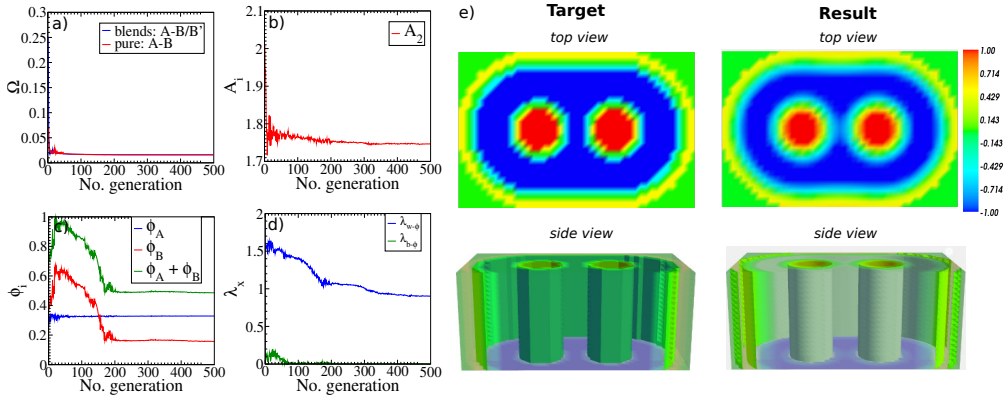

Figure 3.12: A-B/B' mixtures in the double hole-shrink process. a) Evolution of the objective function. b) Evolution of the components volume fraction. c) Evolution of A_1 and A_2. d) Evolution of the wall and bottom surface energy. e) Top and side views of the 'bitmap' target morphology and the morphology generated at the end of the CMA-ES process.

$\bar{\phi}_A$	$\bar{\phi}_B$	$\bar{\phi}_{B'}$	A_2	$\lambda_{w-\phi}$	$\lambda_{w-\psi}$	ϕ_w	ψ_w	$\lambda_{b-\phi}$	$\lambda_{b-\psi}$	ϕ_b	ψ_b
0.329	0.158	0.513	1.75	0.9	0.076	0.278	0.345	0.0036	0.00011	-0.74	0.37

Table 3.7: Evolutionary results of A-B/B' mixtures in the double hole-shrink CMA-ES process.

As in the single hole-shrink process, through trial and error under the restrictions from the optimal condition in the CMA-ES process: $N_A/N_B = \bar{\phi}_A/\bar{\phi}_B = 0.329/0.158 \approx 2.0$ and $\bar{\phi}_{B'} = 0.513$, we found one set of parameters, as shown in Table 3.8, in the TICG model to verify the results of the double hole-shrink CMA-ES process. The morphology generated in the TICG model with A-B/B' mixtures is shown in Figure 3.13. The bottom wall surface is still neutral and the side wall surface is attractive to the minority monomers.

χ_{AB}	κ	N_A	N_B	$N_{B'}$	$\bar{\phi}_{B'}$	Λ_w^A	Λ_w^B	Λ_b^A	Λ_b^B	H	R	L	$\sqrt{N}$
1.15625	1.5625	22	11	4	0.513	-2.0	0.0	0.0	0.0	2.55R_e	2.0R_e	2.0R_e	96

Table 3.8: Parameters for generating the perfect double hole shrink morphology in the TICG model with the A-B/B' mixtures.

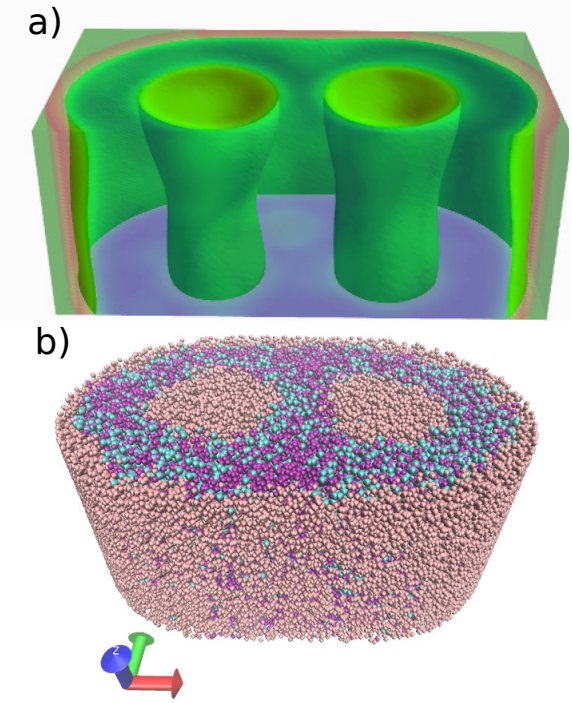

Figure 3.13: Double hole-shrink morphology generated by the TICG model using the optimal volume fractions and surface energies for A-B/B' mixtures from the CMA-ES process. a)The color map of the quantity:$(\phi_A$-$\phi_B)/(\phi_A$+$\phi_B)$.b)The bead representation in the TICG model, where the pink beads, green beads and the purple beads are the A, B and B' monomers, respectively.

Figure 3.14 and Table 3.9 show evolutionary results for A-B/C mixtures in the double hole. In the optimal composition, the A monomers in the copolymer take up 32.8% of the volume fraction and the B monomers take up 67.1%. The concentration of the C monomers in the homopolymer is negligible, below 0.1%. This indicates that pure A-B diblock copolymers are better than A-B copolymer and C homopolymer mixtures for the double hole-shrink geometry. The fact that the lowest residual value of the

objective function in Figure 3.14a) is 0.0161 also supports this conclusion since the lowest average residual value of the objective function in the double hole-shrink process with pure copolymers is also 0.161. As to the surface energy, the side wall remains attractive to the minority block and the bottom surface is neutral. A_1 reduces to zero as there is no macrophase separation.

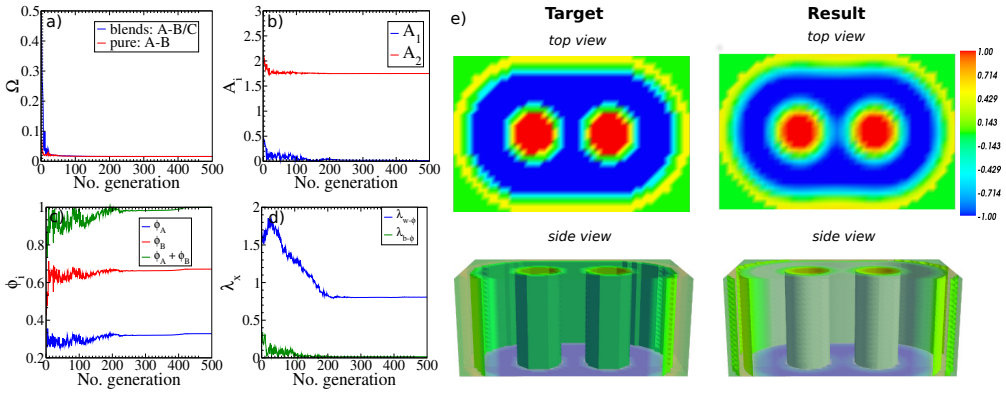

Figure 3.14: A-B/C mixtures in the double hole-shrink CMA-ES process. a) Evolution of the objective function. b) Evolution of the components volume fraction. c) Evolution of A_1 and A_2. d) Evolution of the wall and bottom surface energy. e) Top and side views of the 'bitmap' target morphology and the morphology generated at the end of the CMA-ES process.

$\bar{\phi}_A$	$\bar{\phi}_B$	$\bar{\phi}_C$	A_1	A_2	$\lambda_{w-\phi}$	$\lambda_{w-\psi}$	ϕ_w	ψ_w	$\lambda_{b-\phi}$	$\lambda_{b-\psi}$	ϕ_b	ψ_b
0.328	0.671	0.001	0.0133	1.75	0.806	0.000322	0.25	0.0378	0.015	0.278	-0.294	0.859

Table 3.9: Evolutionary results of A-B/C mixtures in the double hole-shrink CMA-ES process.

We then use the optimal parameters for A-B/C mixtures obtained from the CMA-ES process as restrictions to explore which parameters in the TICG model generate a perfect double hole-shrink morphology. Same as the single hole shrink, since the A-B/C mixtures have degenerated to the A-B copolymer we only need to explore the pure A-B diblock copolymer in the TICG model. Through trial and error, we found a set of parameters which generate perfect double hole shrink morphology and also follow the restrictions:

$\bar{\phi}_A = \mathrm{N}_A/(\mathrm{N}_A + \mathrm{N}_B) \approx 0.328$, as shown in Table 3.10. The morphology generated from the parameters in Table 3.10 is shown in Figure 3.15.

χAB	κ	N_A	N_B	$\bar{\phi}_C$	Λ_w^A	Λ_w^B	Λ_b^A	Λ_b^B	H	R	L	$\sqrt{\bar{N}}$
1.3	1.5625	10	22	0.0	-2.0	0.0	0.0	0.0	$2.55\mathrm{R}_e$	$1.91\mathrm{R}_e$	$1.91\mathrm{R}_e$	96

Table 3.10: Parameters for generating the perfect double hole shrink morphology in the TICG model with the A-B copolymer.

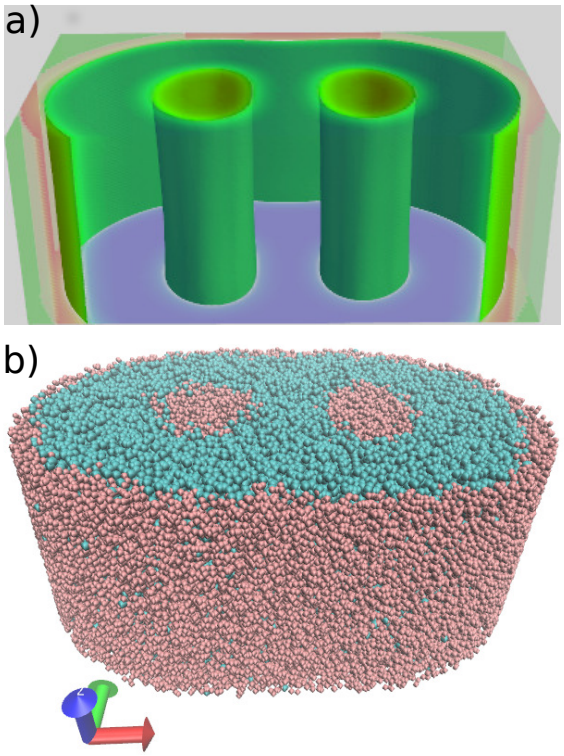

Figure 3.15: Double hole-shrink morphology generated by the TICG model using CMA-ES optimized volume fractions and wall surfaces energy for A-B/C mixtures. As before, a) is the color map of the quantity: $(\phi_A\text{-}\phi_B)/(\phi_A+\phi_B)$. The pink and green beads in b) are A and B monomers, respectively.

3.5 Discussion and Summary

In summary, we have combined the OK model for blends with the CMA-ES algorithm to present a methodology for optimizing the composition and wetting conditions of the

hole-shrink process. This algorithm is computationally inexpensive and can be applied to the DSA of polymer blends in any confinement.

The systems studied in our work are the single cylinder with R = L_0 and H = 1.33L_0 and the double hole with R = L_0, L = L_0 and H = 1.33L_0. We were able to determine the best composition and wetting conditions to generate an equilibrium morphology closest to the artificial 'bitmap' morphology. The target morphology was replicated best with polymer melts comprised of approximately 32% A-type monomers by volume fraction in both the single hole-shrink process and the double hole-shrink process. Both the pure block copolymer and the A-B/B' mixtures can assemble the desired equilibrium morphology with certain wetting conditions. However, the A-B/C mixtures cannot regardless of the wetting conditions.

Although the OK model is a computationally inexpensive method that produces reasonably accurate results, it does have limitations. First, the OK model only uses the volume fractions of monomer components as input parameters and does not include the connectivity of the polymer chains explicitly. Therefore, after the CMA-ES optimization it remains unknown the ideal molecular weight of the polymers for assembly the desired morphology. To address this issue, we have to use the more physically descriptive TICG model. In our work, we found that even with the same volume fraction different molecular weights of the homopolymer B in the A-B/B' blends result in different morphologies. When the homopolymer is short ($N_{B'} = 4$) compared with the A-B block copolymer ($N_{AB} = 32$), the homopolymer B mixes well with the A-B block copolymer and we achieves the desired hole-shrink morphology generated in the OK model. However, if the chain length of the homopolymer is comparable to that of the A-B copolymer ($N_{B'} = N_{AB} = 32$), the homopolymer aggregates into clusters, which leads to defective assembly in the hole-shrink process. Therefore, $N_{B'} = 4$ was used in the TICG model to generate the desired morphology given the volume fractions predicted by the OK model. Second, we have to get more accurate understanding of the energy scale in the OK model by calibrating the morphologies with those generated by the TICG model since the molecular weight and the chain connectivity are not specified in the OK model. It is not straightforward from

the OK model itself what the energy scale is in the system.

CHAPTER 4

EVOLUTIONARY PATTERN DESIGN FOR COPOLYMER DIRECTED SELF-ASSEMBLY

4.1 Abstract

Directed Assembly of Block Copolymers is rapidly becoming a viable strategy for lithography patterning of nanoscopic features. One of the key attributes of directed assembly is that an underlaying chemical or topographic substrate pattern used to direct assembly need not to exhibit a direct correspondence with the sought after block polymer morphology, and past work has largely relied on trial-and-error approaches to design appropriate patterns. With the CMA-ES algorithm introduced in the Chapter 2, we arrive at an efficient method for design of substrates leading to non-trivial, desirable outcomes.

4.2 Introduction

Lithography represents one of the key fabrication steps for nanoscopic devices, ranging from electronic circuits to storage media. [72] As critical device dimensions continue to shrink, alternative patterning strategies and materials are being sought to circumvent some of the challenges that arises at small length scales. These include roughness, pattern collapse, and defectivity. In recent years, the directed assembly of block copolymers on topographic or chemical patterns has received considerable attention as a viable and promising approach for lithographic patterning of ultra-small features. Block copolymers are known to spontaneously self-assemble into a wide range of ordered morphologies, including lamellar, cylindrical, and spherical structures. [72, 7] In thin films, the self-assembly can be directed through the use of chemical or topographic patterns on the underlying substrate. Past work has shown that it is possible to guide the assembly of simple diblock copolymers and their blends with homopolymers into all of the canonical features that arise in integrated circuits, including lines, bends, jogs, and spots.[7] An important concept in directed self-assembly is pattern interpolation, in which only a

subset of any desirable features appears on the substrate, and the block copolymer is used to fill-in the rest, thereby adding information to the fabrication process.

Dense, periodic arrays of lines or spots are of considerable interest for applications in dense storage media. [9, 73, 74, 75] As shown by Ruiz *et al.* [9], the underlying pattern used to direct the assembly of a cylinder forming diblock copolymer need not have the same density as the final storage device; one can pattern a subset of spots on the substrate, and then use the copolymer to create additional bits, thereby doubling, quadrupling, or generally multiplying the storage density of a device. For more complex layouts, such as those encountered in logic devices, a central challenge is to guide the materials to assemble into aperiodic, more versatile, and more complicated morphologies or geometries. Within the spirit of density multiplication, the underlying pattern used to guide the assembly need not have a one-to-one correspondence with the geometry of interest; therefore, we can use the same CMA-ES algorithm presented in Chapter 2 to design an optimal sparse pattern to direct block copolymer self-assembly into a target morphology.

4.3 Methodology

This work is described in the context of a surface pattern consisting of circular spots. Extensions to other types of patterns are trivial. The goal is to use the minimal number of spots on the surface to direct the assembly of a lamellar-forming diblock copolymer into a target morphology. To determine the equilibrium copolymer morphology for a given placement of the surface spots, we use the Ginzburg-Landau(GL) free energy functional, which is a simplified version of the OK model in pure block copolymer system. Similar to Chapter 2, we evolve the morphology using the Cahn-Hilliard equation. We also introduce the same "fitness" function which quantifies the difference between the target morphology and the current equilibrium morphology. The guiding patterns in this work are represented by a set of poles, with the number of spots held constant. The "fitness" function depends only on the spot positions as the composition of block copolymer is fixed. Then we use the CMA-ES strategy to minimize the fitness function.

4.3.1 Ginzburg-Landau Equation for Block Copolymer

We consider a system of pure diblock copolymers composed of A and B type monomers. A and B type monomers have the same reference volume and statistical segment length. The total number of beads and the volume fraction of A blocks are denoted as N and f, respectively. Because there is no homopolymer in the system, Equation 3.1 can be simplified to the following equation as $\psi = 1$.

$$\mathbf{F}[\phi] = \mathbf{F_S}[\phi] + \mathbf{F_L}[\phi] + \int d\mathbf{r} H_{ext}[\mathbf{r}]. \tag{4.1}$$

Same as in Chapter 2, $\phi \equiv \phi_A(\mathbf{r}) - \phi_B(\mathbf{r})$ is the order quantifying the extent of phase separation and $H_{ext}[\mathbf{r}]$ is the external potential representing the interaction between the guiding spots and the copolymers. The form of $H_{ext}[\mathbf{r}]$ is different from that in Chapter 2 as the guiding pattern becomes poles instead of a flat or curved surface. We use the hyperbolic tangent function introduced in ref. [76], $H_{ext}[\mathbf{r}] = -(1/2)V_0(tanh(-|\mathbf{r} - \mathbf{R}| + \sigma)/\lambda + 1)$, where $\mathbf{R}$ is the position of the spot center, V_0 is the strength of the potential, σ is the range of the potential, and λ controls the steepness of the decay.

The other terms $\mathbf{F_S}[\phi]$ and $\mathbf{F_L}[\phi]$ can be got by substituting $\psi = 1$ in Equation 4.1 and Equation 3.6, respectively.

$$\mathbf{F_S}[\phi] = \int d\mathbf{r}[\frac{1}{2}(\nabla\phi)^2 + W[\phi]. \tag{4.2}$$

$$W(\phi) = g_1(\phi) = -Aln\ cosh(\phi) + \phi^2/2 \tag{4.3}$$

$$\mathbf{F_L}[\phi] = \frac{\alpha}{2} \int dr \int dr' \mathbf{G}[\mathbf{r}, \mathbf{r'}]\delta\phi(\mathbf{r})\delta\phi(\mathbf{r'}). \tag{4.4}$$

The meaning of the parameters are the same as those illustrated in Chapter 2. Similar to Chapter 2, to find the equilibrium morphology, we use the Cahn-Hilliard equation to evolve the ϕ field, which is appropriate for conserved order parameters. Unlike the two Cahn-Hilliard equations in Chapter 2, there is only one Cahn-Hilliard equation, which is

Equation 3.12. Substituting the free energy expression in Equation 3.12, we get

$$\frac{\partial \phi}{\partial\, t} = \nabla^2[-\nabla^2\phi - Atanh(\phi) + \phi] + \nabla^2 H_{ext}(\mathbf{r}) - \alpha\delta\phi \tag{4.5}$$

To use the CMA-ES algorithm, we still quantify the objective function by the averaged squared difference between the current $\phi_{eq}(\mathbf{r})$ and $\hat{\phi}(\mathbf{r})$ per cell, which is Equation . Our goal is to optimize spot positions by minimizing Ω.

4.4 Results

4.4.1 Phase Diagram in the A-f Plane

Before optimizing the spot positions using the evolutionary algorithm, we explored the effects of various controlling parameters in the generic CH equation. Figure 4.1 shows the typical morphologies obtained for various values of A and f, and at a fixed value of α. Here $f \equiv \phi_A - \phi_B$ is the block volume fraction that controls the symmetry of the morphology. And A is the same parameter defined in Chapter 2, which controls the strength of incompatibility between different blocks.

The results in Figure 4.1 are consistent with the physical meaning of A and α. For $A \leq 1.0$, homogeneous morphologies are found for all f values. For $A > 1.0$, the lamellar patterns are found at compositions close to $f = 0.5$, and the hexagonally packed cylindrical morphologies are found at asymmetric compositions, even though in both cases the presence of defects is apparent.

In what follows, we focus on systems forming a lamellar morphology, and use the following parameters: A=1.3, f=0.5 and α=0.002. This set of parameter gives distinct lamellar having a natural periodicity of $L_0 \simeq 20$.

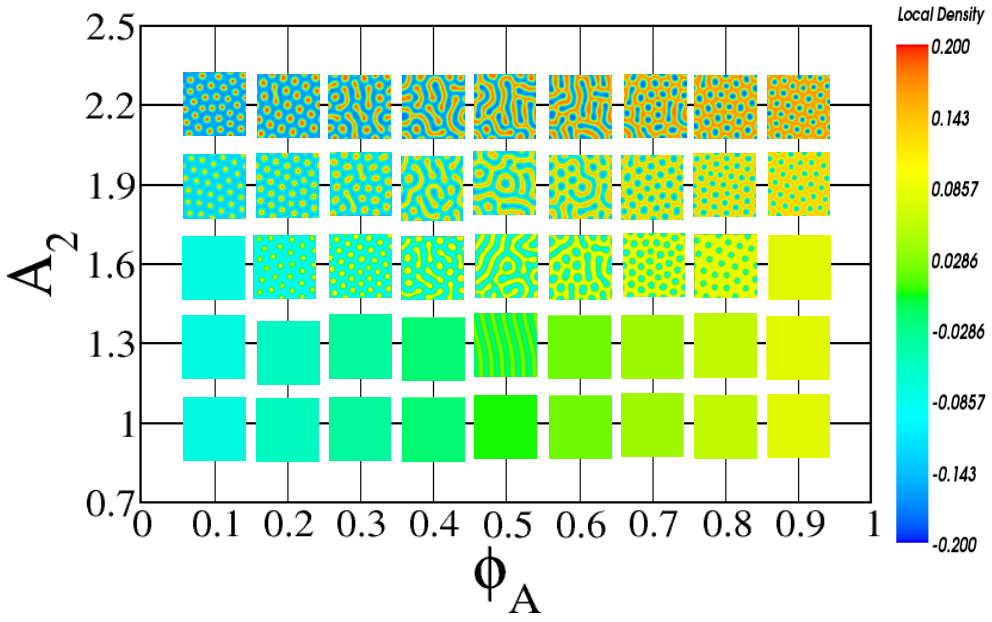

Figure 4.1: 2-D phase diagram at varying values of A and f, for $\alpha = 0.02$. Morphologies are obtained by evolving the CH equation for 2×10^8 steps from a random initial configuration(δt = 0.01). The grid size: 100×100.

4.4.2 Optimization Using Evolutionary Algorithm

We now presents results obtained using the CMA-ES optimization. As mentioned in Chapter 2, the population size is λ=28 and the number of fitting samples used to spawn new trajectories is μ=4. The first target morphology defined here is a pattern mimicking the letter "I", shown in Figure 4.2. The number of anchoring spots representing the chemical pattern is 9. Initial spot positions are generated at random, and the initial morphology is calculated by evolving the CH equation, as shown in the inset of Figure 4.2(a). At each iteration step, the spots are repositioned using the CMA-ES algorithm, and the equilibrium morphology is generated by solving the CH equation. The values of the objective function calculated using Equation 4.3.1 and are spotted in Figure 4.2(a), as a function of iteration number(also see the insert for a plot on a logarithmic scale). The results suggest that the magnitude of the objective function decays nearly exponentially,

and that there exists two convergence rate regimes. The first (below 150 iterations) has a smaller slope; the second regime (above 150 iterations) has a greater slope, implying that the spot positions are first optimized globally, and then locally. The results also show that the optimal spot positions are identified within 250 evolution iterations, and that the residual value of the objective function drops to the level of 10^{-8}. The final configuration and the corresponding spot positions are shown in Figure 4.2(c).

To verify that the solution identified by CMA-ES is at least a local optimal, we performed the following test: we first place the spots at ideal positions that are likely to generate the "I" pattern, and then use the solution of the CH equation as the target morphology and re-iterate from a random state. Since now the target morphology is a solution of the CH equation, it is also a well-defined minimum of the objective function Equation 4.3.1, and ideally the minimum should be bracketed by the CMA-ES algorithm. This is indeed confirmed by our results. On the other hand, in general, the exact spot positions obtained from CMA-ES optimization depend slightly on the initial configuration. One way to reduce this dependence is to conduct multiple optimizations, and use the average.

To further demonstrate that the CMA-ES only has a weak dependence on the initial pole arrangement, we show in Figure 4.3 the optimization results obtained using three distinct ways of generating the initial pole arrangement, by placing poles: (1) randomly, (2) regularly on a lattice, and (3) at a single point. In all three cases, the convergence rates as evidenced by the objective function values are comparable, and the converged morphologies are nearly identical. Indeed, one particularly attractive feature of the CMA-ES optimization is that it has a stronger dependence on the initial step size (searching radius) than the initial pole position. Furthermore, the searching radius in CMA-ES is self-adaptive; the algorithm can refine the value progressively as the morphologies are evolved based on the closeness to the target morphology.

To further test the efficiency of the CMA-ES algorithm, we used several other non-trivial patterns. Two sets of target and optimized morphologies are shown in Figure 4.4, which mimic the letters "M" and "E", respectively. Both of these two patterns are gen-

erated using the same parameter set as the pattern "I", and the convergence behaviors are similar.

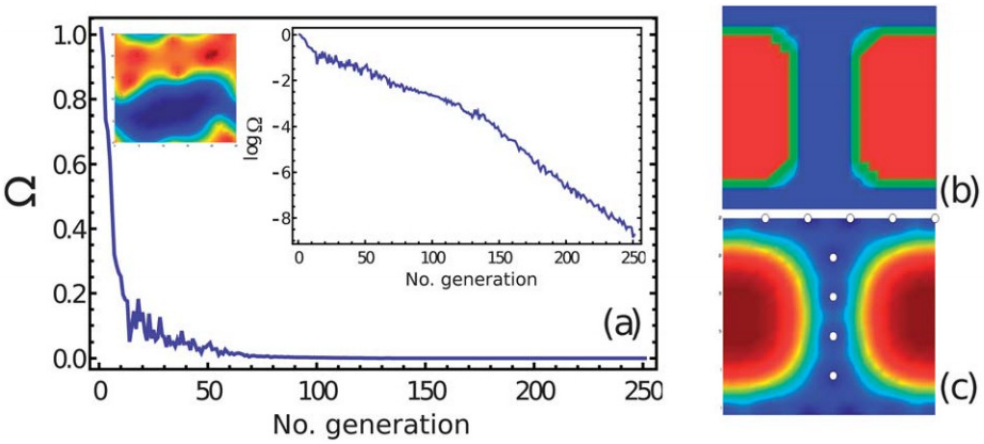

Figure 4.2: Evolutionary results of the "I" pattern. (a) Evolution of the objective function; (b) The target morphology. (c) The optimal morphology and the spot positions. Parameters: A=1.3, α=0.002, and N=50.

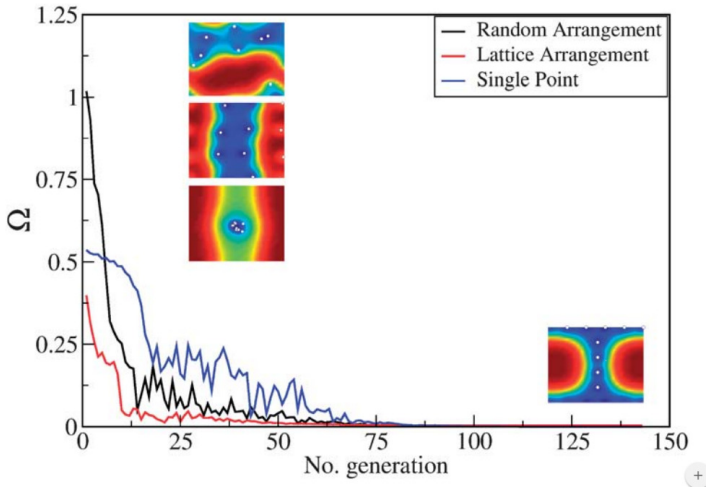

Figure 4.3: Convergence behavior of the CMA-ES optimization using three different ways of generating the initial set of pole arrangements: (1)completely random;(2) lattice based;(3)at the same starting point.

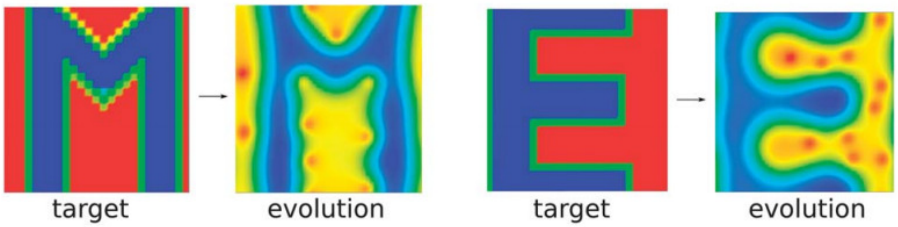

Figure 4.4: Target and optimal morphologies for the “M“ and “E“ patterns. The parameter set is the same as that in Figure 4.2

4.5 Summary

We have presented a methodology to solve the pattern design problem by using a Cahn-Hilliard equation to find the equilibrium morphology of diblock copolymers and by using the CMA-ES algorithm to optimize the underlying chemical pattern. The applicability and usefulness of the proposed strategy were demonstrated by using lamellar forming diblock copolymers to create three nontrivial target morphologies.

The size of the systems considered here was modest, about $2L_0 \times 2L_0$, and the overall calculation time required to generate an optimal solution was approximately 8 hours on a single processor. The extension of the methodology to larger systems and different morphologies is straightforward. The computational efficiency of the proposed approach could be easily increased by using parallel algorithms: (1) The numerical complexity for solving the CH equation scales with the system size(N^2). This step involves essentially matrix vector products, and can be readily parallelized. (2) The CMA-ES essentially involves a set of independent populations, which can also be parallelized in a trivial way.

The objective function used in this work is the simplest that one can think of. More elaborate versions could potentially be used to improve the rate of convergence. For instance, instead of calculating the difference in real space, one may consider the difference in Fourier mode coefficients. Assigning different weights to long and short wavelength modes may lead to a more efficient optimization behavior. The CahnHilliard equation was used in this work to resolve the composition profile. As a generic framework, the equation also enables us to study assembly dynamics, and can be adapted to study more

complex systems, including polymer mixtures in Chapter 2. These possibilities will be addressed in future work.

CHAPTER 5

FINAL REMARKS AND FUTURE WORK

This work attempts to address some of the key challenging issues pertaining to the rheology of entangled nanocomposites and the industrial applications of the DSA process.

In Chapter 2, We described the TICG model for homopolymers and nanoparticles. Then we also discussed how to use the grand-canonical ensemble and Monte Carlo (MC) algorithm to simulate slip springs in the nanocomposites, where we use Brownian Dynamics to evolve the system. The slip springs place temporary topological constraints to the polymer chains and act as entanglements in the nanocomposites. We first studied the radial distribution function of polymer beads and slip springs around a single nanoparticle. Though both the polymer beads and the slip springs have depletion layers surrounding the nanoparticle, the depletion layer of slip springs is deeper than the depletion layer of the polymer beads. Therefore the probability of forming slip springs on a single bead is actually lower than that probability in the bulk, which means that the polymers are less entangled close to the nanoparticle surface. Then we computed the radial distribution of polymer chain ends surrounding the nanoparticle. The polymer chains ends show much less depletion layer than that of polymer beads, which means that the polymer chains are less influenced by the depletion force.

Next, we studied the diffusion of the single nanoparticle in entangled and unentangled homopolymers. When the size of the nanoparticle is small, the diffusion of the nanoparticle in entangled polymer melts show linear scaling law $\sim$t. However, when the size of nanoparticle is comparable to or larger than the entanglement mesh size, the scaling law in entangled nanocomposites can be as low as $\sim t^0.3$. This nonlinear diffusion region does not show up in unentangled nanocomposites when the size of the nanoparticle increases.

Finally, we studied loaded nanocomposites system. The addition of the nanoparticles decreases the density of slip springs in our system, which make the nanocomposites less entangled. This effect will be reduced as the size of particles becomes larger. In addition, because the stress correlation function related to the core has faster decaying power rate than the stress correlation function related to the bond, the free volume effects also

contribute to the decrease of viscosity when the size of the nanoparticle is small. This non-Einstein like decrease in viscosity with the addition of nanoparticles has been confirmed Mackay. *et.al.* [32] After the size of the particles increases, the Einstein predictions will be recovered. However, it still remains a question where the turning point happens. What's more, the rheology of the non-equilibrium entangled nanocomposites also hasn't been explored. And the rotation of nanoparticles should be added into such systems as rotation is a very important feature of nanoparticles in the shear flow.

In Chapter 3, we introduced the CMA-ES algorithm and the OK model for copolymer/homopolymer mixtures. We combined these two methods and introduce a methodology which optimize the compositions and the surface energies together in order to generate the perfect hole-shrink morphology. We applied the new methodology in the pure block copolymers, the A-B/B' mixtures and the A-B/C mixtures in two different scenarios: the single hole-shrink process and the double hole-shrink process. We found that both the pure block copolymer and the A-B/B' mixtures can form the desired perfect hole-shrink morphology under certain conditions of compositions and surface energy. However, the A-B/C mixtures is always a bad choice in forming perfect cylinder in the hole-shrink process compared with the other two compositions. Current work only studied the hole-shrink process with side wall attractive to the minority block, in the future we should also study the systems with the side-wall surface attractive to the majority block and the shape of contact hole could also be taken into account as an optimization parameter.

In Chapter 4, we reduced the composition to only pure block copolymer and arrive at an efficient method for design of substrates leading to non-trivial, desirable morphologies in the 2-D system. The lamellar forming diblock copolymer is used in the system with $\phi_A = 0.5$. Then we use the CMA-ES method to optimize the pole positions and is able to generate the desirable morphologies in an efficient way. However, the applications of this methodology is still limited as the compositions we study is pure block copolymers and we assure that the system is in 2-D system with periodic boundary conditions, which is unrealistic. In the future work, the diverse compositions such as copolymer/homopolymer

mixtures should be explored and complex systems with different shapes and finite boundary conditions should also be examined.

REFERENCES

[1] William Humphrey, Andrew Dalke, and Klaus Schulten. VMD – Visual Molecular Dynamics. *Journal of Molecular Graphics*, 14:33–38, 1996.

[2] François A. Detcheverry, Huiman Kang, Kostas Ch. Daoulas, Marcus Müller, Paul F. Nealey, and Juan J. de Pablo. Monte carlo simulations of a coarse grain model for block copolymers and nanocomposites. *Macromolecules*, 41:4989–5001, 2008.

[3] Takao Ohta and Aya Ito. Dynamics of phase separation in copolymer-homopolymer mixtures. *Physical Review E*, 52:5250, 1995.

[4] Michael Rubinstein and Ralph H. Colby. *Polymer Physics*. Oxford University Press, Oxford, U.K., 2003.

[5] Ian W. Hamley. *The Physics of Block Copolymers*. Oxford University Press, New York, 1998.

[6] Frank S. Bates and Glenn H. Fredrickson. Block copolymersdesigner soft materials. *Physics Today*, 52, 1999.

[7] Mark P. Stoykovich, Huiman Kang, Kostas Ch. Daoulas, Guoliang Liu, Chi-Chun Liu, Juan J. de Pablo, Marcus Mller, and Paul F. Nealey. Directed self-assembly of block copolymers for nanolithography: Fabrication of isolated features and essential integrated circuit geometries. *ACS Nano*, 1, 2007.

[8] Mark P. Stoykovich, Huiman Kang, Kostas Ch. Daoulas, Guoliang Liu, Chi-Chun Liu, Juan J. de Pablo, Marcus Mller, and Paul F. Nealey. Directed assembly of block copolymer blends into nonregular device-oriented structures. *Science*, 308, 2005.

[9] Ricardo Ruiz, Huiman Kang, François A. Detcheverry, Elizabeth Dobisz, Dan S. Kercher, Thomas R. Albrecht, Juan J. de Pablo, and Paul F. Nealey. Density multiplication and improved lithography by directed block copolymer assembly. *Science*, 321, 2008.

[10] Ricardo Ruiz, Elizabeth Dobisz, and Thomas R. Albrecht. Rectangular patterns using block copolymer directed assembly for high bit aspect ratio patterned media. *ACS Nano*, 5, 2011.

[11] Lloyd R. Harriott. Limits of lithography. *Proceedings of IEEE*, 89, 2001.

[12] Takashi Ito and Shinji Okazaki. Pushing the limits of lithography. *Nature*, 406, 2000.

[13] C. Grant Willson and Bernard J. Roman. The future of lithography: Sematech litho forum 2008. *ACS Nano*, 2, 2008.

[14] Alain Diebold and Christina Hacker. *International Technology Roadmap for Semicondors*, 2012.

[15] Kosmas Galatsis, Kang L. Wang, Mihri Ozkan, Cengiz S. Ozkan, Yu Huang, Jane P. Chang, Harold G. Monbouquette, Yong Chen, Paul Nealey, and Youssry Botros. Patterning and templating for nanoelectronics. *Advanced Materials*, 22, 2010.

[16] M. Doi and S.F. Edwards. *The Theory of Polymer dynamics*. Oxford University Press, Oxford, U.K., 1986.

[17] P. G. de Gennes. Reptation of a polymer chain in the presence of fixed obstacles. *J. Chem. Phys.*, 55:572, 1971.

[18] Ph. Buffat and J-P Borel. Size effect on the melting temperature of gold partlclese. *Physical Review A*, 13:22872298, 1976.

[19] Robert A. Taylor, Todd Otanicar, and Gary Rosengarten. Nanofluid-based optical filter optimization for pv/t systems. *Nature: Light Science and Applications*, 1:1–7, 2012.

[20] Robert A. Taylor, Todd P. Otanicar, Yasitha Herukerrupu, Fabienne Bremond, Gary Rosengarten, Evatt R. Hawkes, Xuchuan Jiang, and Sylvain Coulombe. Feasibility of nanofluid-based optical filters. *Applied Optics*, 52:1413–1422, 2013.

[21] Robert A Taylor, Patrick E Phelan, Todd P Otanicar, Ronald Adrian, and Ravi Prasher. Nanofluid optical property characterization: towards efficient direct absorption solar collectors. *Nanoscale Research Letters*, 6:225, 2011.

[22] Saba Hasan. A review on nanoparticles: Their synthesis and types. *Res. J. Recent. Sci.*, 4:1–3, 2015.

[23] Charles Goodyear. Goodyear's verfahren zur fabrication von gegenstnden aus kautschuk und gutta-percha. *1856*, 139, 1856.

[24] Arimitsu Usuki, Yoshitsugu Kojima, Massaya Kawasumi, Akane Okada, Yoshiaki Fukushima, Toshio Kurauchi, and Osami Kamigaito. Synthesis of nylon 6-clay hybrid. *Journal of Materials Research*, 8:1179–1184, 1993.

[25] Yoshitsugu Kojima, Arimitsu Usuki, Massaya Kawasumi, Akane Okada, Yoshiaki Fukushima, Toshio Kurauchi, and Osami Kamigaito. Mechanical properties of nylon 6-clay hybrid. *Journal Of Materials Research*, 8:1185–1189, 1993.

[26] T. Kataoka, T. Kitano, M. Sasahara, , and K. Nishijima. Viscosity of particle filled polymer melts. *Rheologica Acta*, 17, 1978.

[27] Umi Yamamoto and Kenneth S. Schweizer. Theory of nanoparticle diffusion in unentangled and entangled polymer melts. *J. Chem. Phys.*, 135, 2011.

[28] Li-Heng Cai, Sergey Panyukov, and Michael Rubinstein. Mobility of nonsticky nanoparticles in polymer liquids. *J. Chem. Phys.*, 135, 2011.

[29] Anish Tuteja and Michael E. Mackay. Effect of ideal, organic nanoparticles on the flow properties of linear polymers: non-einstein-like behavior. *Macromolecules*, 38, 2005.

[30] Anish Tuteja and Michael E. Mackay. Breakdown of the continuum stokeseinstein relation for nanoparticle diffusion. *Nano Lett.*, 7, 2007.

[31] Anish Tuteja, Phillip M. Duxbury, and Michael E. Mackay. Multifunctional nanocomposites with reduced viscosity. *Macromolecules*, 40, 2007.

[32] Michael E. Mackay, Tien T. Dao, Anish Tuteja, Derek L. Ho, Brooke Van Horn, Ho-Cheol Kim, and Craig J. Hawker. Nanoscale effects leading to non-einstein-like decrease in viscosity. *Natural Materials*, 2, 2003.

[33] Benjamin J. Anderson and Charles F. Zukoski. Rheology and microstructure of entangled polymer nanocomposite melts. *Macromolecules*, 42, 2009.

[34] Rose S. Ndong and William B. Russel. Rheology of surface-modified titania nanoparticles dispersed in pdms melts: The significance of the power law. *J. Rheol.*, 56, 2012.

[35] So Youn Kim and Charles F. Zukoski. Super- and sub-einstein intrinsic viscosities of spherical nanoparticles in concentrated low molecular weight polymer solutions. *Soft Matter*, 8, 2012.

[36] Glenn V. Gordon, Randall G. Schmidt, Marlitt Quintero, Natalie J. Benton, Terence Cosgrove, Val J. Krukonis, Kara Williams, and Paula M. Wetmore. Impact of polymer molecular weight on the dynamics of poly(dimethylsiloxane)polysilicate nanocomposites. *Macromolecules*, 43, 2010.

[37] Sachin Jain, Johannes G. P. Goossens, Gerrit W. M. Peters, Martin van Duin, and Pieter J. Lemstra. Strong decrease in viscosity of nanoparticle-filled polymer melts through selective adsorption. *Soft Matter*, 4, 2008.

[38] Klaus Nusser, Gerald J. Schneider, Wim Pyckhout-Hintzen, and Dieter Richter. Viscosity decrease and reinforcement in polymersilsesquioxane composites. *Macromolecules*, 4, 2011.

[39] Jagannathan T. Kalathi, Gary S. Grest, and Sanat K. Kumar. Universal viscosity behavior of polymer nanocomposites. *Phys. Rev. Lett.*, 109, 2012.

[40] Mu Wanga and Reghan J. Hill. Anomalous bulk viscosity of polymer-nanocomposite melts. *Soft Matter*, 5, 2009.

[41] Venkat Ganesan Victor Pryamitsyn Megha Surve and Bharadwaj Narayanan. Noncontinuum effects in nanoparticle dynamics in polymers. *J. Chem. Phys.*, 124, 2006.

[42] Suchira Sen, James D. Thomin, Sanat K. Kumar, and Pawel Keblinski. Molecular underpinnings of the mechanical reinforcement in polymer nanocomposites. *Macromolecules*, 40, 2007.

[43] Francis W. Starr, Jack F. Douglas, and Sharon C. Glotzer. Origin of particle clustering in a simulated polymer nanocomposite and its impact on rheology. *J. Chem. Phys.*, 119, 2003.

[44] Grant D. Smith, Dmitry Bedrov, Liwei Li, and Oleksiy Byutner. A molecular dynamics simulation study of the viscoelastic properties of polymer nanocomposites. *J. Chem. Phys.*, 117, 2002.

[45] Diego Del Biondo, Elian M. Masnada, Samy Merabia, Marc Couty, and Jean-Louis Barrat. Numerical study of a slip-link model for polymer melts and nanocomposites. *J. Chem. Phys.*, 138, 2012.

[46] Hongyu Guo, Gilles Bourret, R. Bruce Lennox, Mark Sutton, James L. Harden, and Robert L. Leheny. Entanglement-controlled subdiffusion of nanoparticles within concentrated polymer solutions. *Phys. Rev. Lett.*, 109, 2012.

[47] Rami A. Omari, Andrew M. Aneese, Christopher A. Grabowski, and Ashis Mukhopadhyay. Diffusion of nanoparticles in semidilute and entangled polymer solutions. *Phys. Rev. Lett.*, 113, 2009.

[48] I. Y. Wong, M. L. Gardel, D. R. Reichman, Eric R. Weeks, M. T. Valentine, A. R. Bausch, and D. A. Weitz. Anomalous diffusion probes microstructure dynamics of entangled f-actin networks. *Phys. Rev. Lett.*, 92, 2004.

[49] Jagannathan T. Kalathi, Umi Yamamoto, Kenneth S. Schweizer, Gary S. Grest, and Sanat K. Kumar. Nanoparticle diffusion in polymer nanocomposites. *Phys. Rev. Lett.*, 112, 2014.

[50] Jagannathan T. Kalathi, Sanat K. Kumar, Michael Rubinstein, and Gary S. Grest. Rouse mode analysis of chain relaxation in polymer nanocomposites. *Soft Matter*, 11, 2015.

[51] François A. Detcheverry, Darin Q.Pike, Paul F. Nealey, Marcus M*ü*ller, and Juan J. de Pablo. Monte carlo simulation of coarse grain polymeric systems. *Phys. Rev. Lett.*, 102:197801, 2009.

[52] Hongxia Guo, Kurt Kremer, and Thomas Soddemann. Nonequilibrium molecular dynamics simulation of shear-induced alignment of amphiphilic model systems. *Physical Review E*, 66, 2002.

[53] Hongxia Guo. Shear-induced parallel-to-perpendicular orientation transition in the amphiphilic lamellar phase: A nonequilibrium molecular-dynamics simulation study. *J. Chem. Phys.*, 124, 2006.

[54] Jay D. Schieber. Fluctuations in entanglements of polymer liquids. *J. Chem. Phys.*, 118, 2003.

[55] Veronica C. Chappa, David C. Morse, Annette Zippelius, and Marcus Mller. Translationally invariant slip-spring model for entangled polymer dynamics. *Phys. Rev. Lett.*, 109, 2012.

[56] Takashi Uneyama and Yuichi Masubuchi. Multi-chain slip-spring model for entangled polymer dynamics. *J. Chem. Phys.*, 137, 2012.

[57] F. Amblard, A. C. Maggs, B. Yurke, A. N. Pargellis, and S. Leibler. Subdiffusion and anomalous local viscoelasticity in actin networks. *Phys. Rev. Lett.*, 77, 1996.

[58] Renat N. Khaliullin and Jay D. Schieber. Self-consistent modeling of constraint release in a single-chain mean-field slip-link model. *Macromolecules*, 42, 2009.

[59] Roel Gronheid, Paulina Rincon Delgadillo, Arjun Singh, Todd R. Younkin, Safak Suyan, Boon Teik Chan, Lieve Van Look, Joost Bekaert, Ivan Pollentir1, and Paul F. Nealey. Readying directed self-assembly for patterning in semi-conductor manufacturing. *J. Photopolym. Sci. Technol.*, 26, 2013.

[60] Yuriko Seino, Hiroki Yonemitsu, Hironobu Sato, Masahiro Kanno, Hirokazu Kato, Katsutoshi Kobayashi, Ayako Kawanishi, Tsukasa Azuma, Makoto Muramatsu, Seiji Nagahara, Takahiro Kitano, and Takayuki Toshima. Contact hole shrink process using graphoepitaxial directed self-assembly lithography. *J. Micro/Nanolith. MEMS MOEMS*, 12, 2013.

[61] Yuriko Seino, Hiroki Yonemitsu, Hironobu Sato, Masahiro Kanno, Hikazu Kato, Katsutoshi Kobayashi, Ayako Kawanishi, Tsukasa Azuma, Makoto Muramatsu, Seiji Nagahara, Takahiro Kitano, and Takayuki Toshima. Contact hole shrink process using directed self-assembly. *Proc. SPIE 8323, Alternative Lithographic Technologies IV*, 83230Y, 2012.

[62] Brandon L. Peters, Ben Rathsack, Mark Somervell, Takeo Nakano, Gerard Schmid, and Juan J de Pablo. Graphoepitaxial assembly of cylinder forming block copolymers in cylindrical holes. *Journal of Polymer Science Part B: Polymer Physics*, 53, 2015.

[63] Kenji Yoshimoto, Ken Fukawatase, Masahiro Ohshima, Yoshihiro Naka, Shimon Maeda, Satoshi Tanaka, Seiji Morita, Hisako Aoyama, and Shoji Mimotogi. Optimization of directed self-assembly hole shrink process with simplified model. *J. Micro/Nanolith. MEMS MOEMS*, 13, 2014.

[64] Takao Ohta and Kyozi Kawasaki. Equilibrium morphology of block copolymer melts. *Macromolecules*, 19:2621–2632, 1986.

[65] Stefan Kern and Petros Koumoutsakos. Simulations of optimized anguilliform swimming. *Journal of Experimental Biology*, 209, 2006.

[66] Artem R. Oganov and Colin W. Glass. Crystal structure prediction using ab initio evolutionary techniques: Principles and applications. *J. Chem. Phys*, 124, 2006.

[67] Nikolaus Hansen, Andr S. P. Niederberger, Lino Guzzella, and Petros Koumoutsakos. A method for handling uncertainty in evolutionary optimization with an application to feedback control of combustion. *IEEE Transactions on Evolutionary Computation*, 13, 2009.

[68] Jian Qin, Gurdaman S. Khaira, Yongrui Su, Grant P. Garner, Marc Miskin, Heinrich M. Jaegerb, and Juan J. de Pablo. Evolutionary pattern design for copolymer directed self-assembly. *Soft Matter*, 9, 2013.

[69] Gurdaman S. Khaira, Jian Qin, Grant P. Garner, Shisheng Xiong, Lei Wan, Ricardo Ruiz, Heinrich M. Jaeger, Paul F. Nealey, and Juan J. de Pablo. Evolutionary optimization of directed self-assembly of triblock copolymers on chemically patterned substrates. *ACS Macro Letters*, 3, 2014.

[70] Nikolaus Hansen, Sibylle D. Mller, and Petros Koumoutsakos. Reducing the time complexity of the derandomized evolution strategy with covariance matrix adaptation (cma-es). *Evolutionary Computation*, 11, 2003.

[71] Umang Nagpal, Marcus Mller, Paul F. Nealey, and Juan J. de Pablo. Free energy of defects in ordered assemblies of block copolymer domains. *Macro Letters*, 1:418–422, 2012.

[72] Yu-Chih Tseng and Seth Darling. Block copolymer nanostructures for technology. *Polymers*, 2, 2010.

[73] François A. Detcheverry, Guoliang Liu, Paul F. Nealey, and Juan J. de Pablo. Interpolation in the directed assembly of block copolymers on nanopatterned substrates: Simulation and experiments. *Macromolecules*, 43:3446–3454, 2010.

[74] C.-C. Liu, A. Ramrez-Hernndez, E. Han, G. S. W. Craig, Y. Tada, H. Yoshida, H. Kang, S. Ji, P. Gopalan, J. J. de Pablo, and P. F. Nealey. Chemical patterns for directed self-assembly of lamellae-forming block copolymers with density multiplication of features. *Macromolecules*, 46:1415–1424, 2013.

[75] J. Y. Cheng, C. A. Ross, V. Z.-H. Chan, E.L. Thomas, R.G.H. Lammertink, and G. J. Vancso. Formation of a cobalt magnetic dot array via block copolymer lithography. *Advanced Materials*, 13:1174–1178, 2001.

[76] Weihua Li, Feng Qiu, Yuliang Yang, and An-Chang Shi. Ordering dynamics of directed self-assembly of block copolymers in periodic two-dimensional fields. *Macromolecules*, 43, 2010.